2007

Study of microburst-induced wind flow and its effects on cube-shaped buildings using numerical and experimental simulations of an impinging jet

Anindya Sengupta
Iowa State University

Study of microburst-induced wind flow and its effects on cube-shaped buildings using numerical and experimental simulations of an impinging jet

by

Anindya Sengupta

A dissertation submitted to the graduate faculty

in partial fulfillment of the requirements for the degree of

DOCTOR OF PHILOSOPHY

Major: Engineering Mechanics

Program of Study Committee:
Partha P. Sarkar, Major Professor
Ganesh R. Rajagopalan, Co-major Professor
William A. Gallus, Jr.
Frederick L. Haan, Jr.
Thomas J. Rudolphi
John Tannehill

Iowa State University

Ames, Iowa

2007

Dedication

This Dissertation is dedicated to people who have influenced my life the most

My

Grandmother .. mother .. friend .. philosopher .. and .. guide

Mrs. Satadal Roy

(July 16th, 1909 – Dec 23rd, 2001)

for her lifelong sacrifices

and

My Wife

Sreemoyee Sengupta (Maitra)

TABLE OF CONTENTS

ACKNOWLEDGEMENTS

I would like to express my sincere gratitude and appreciation for my major advisor, Dr. Partha P. Sarkar, for the encouragement and guidance throughout my study at Iowa State. He has always been there to spend numerous hours explaining to me the finer details of Wind Engineering.

I would also like to thank Dr. Ganesh Rajagopalan, my co-major advisor for his encouragement and constructive criticism in the numerical portion of my dissertation.

My sincere appreciation goes to my committee members, Dr. Fred Haan, Dr. Bill Gallus, Dr. John Tannehill and Dr. Tom Rudolphi for their help at various stages of my research work, either on the experimental, numerical side or meteorological side.

I would also like to thank Dr. Tom Rudolphi (former Head, Department of Aerospace Engineering) and Dr. Tom Shih (Head, Department of Aerospace Engineering) for providing me financial support in the form of a teaching assistantship for a major portion of my stay at the Aerospace Engineering Department, so as to enable me to complete my research work here without any financial worries.

I would like to thank all the staff at the Department of Aerospace Engineering, specially Dee Pfeiffer and Gayle Fay, who went out of their way to help me with all the paperwork and make my stay here a memorable one. Sincere thanks to Bill Rickard and John Stronck for their help in setting up the microburst simulator. I would also like to thank the College of Engineering and the Department of Aerospace Engineering for providing me the computational facilities to complete the long and tedious numerical simulations.

My deepest gratitude and appreciation is reserved for my wife, Sreemoyee, who has always been by my side for the past 7 years, spending sleepless nights along with me, so that I could complete my research work in a timely and effective manner. With her love and caring attitude along with great culinary skills, she has given me stability in my personal life, so that I could be a better person.

ABSTRACT

Microbursts are a major cause of concern for structures both on ground as well as those in air, namely aircrafts. The velocity profile of a microburst is completely different compared to natural boundary-layer wind profiles. The current research is directed to simulation of microburst phenomenon using an impinging jet model. This research reports the first 3D numerical simulation of microbursts and its effects on buildings. Broadly the major accomplishments of the current research can be focused in three major directions.

In the first case, extensive research on velocity profiles of the wall jet that is formed after jet impingement has been conducted experimentally. The main motivation was to develop empirical equations for boundary layer growth based on experimental data, using hot-wire, PIV and pressure rake. Numerical simulations were carried out with different turbulence models so as to find the best turbulence model to simulate this kind of flow.

In the second case, both mean and peak loads on building models under static microburst wind loadings were studied, using both experimental as well as numerical techniques. Parametric study by varying the height of jet impingement, jet exit velocities and size of building models was conducted. It was found that the large eddy simulation (LES) produced results in excellent agreement with the experimental data. The flow field around the building model was obtained using PIV and comparisons were made with the LES results.

Thirdly, and the most important part of this research work was to simulate a translating microburst and study the loads on buildings using a moving impinging jet. Numerical

simulation was validated with the experimental data for one jet translation speed. LES results again matched the experimental data for translating microburst loads on building, with reference to the drag and lift coefficients. The peak loads predicted by LES were within experimental limits. Effects of increased jet translation speeds on the peak loads on building were studied using numerical simulation. It was also found that the drag on building increased monotonically with increase in jet translation speeds, although the lift did not increase significantly. Microburst can produce loads on buildings equivalent to that generated by an F2 tornado.

CHAPTER 1

GENERAL INTRODUCTION

1.1 Wind Effects on Structures

The random nature of wind and its interaction with buildings causing flow separation, vortex formation and wake development makes the study of building aerodynamics very complex and interesting [Cook (1990), Simiu and Scanlan (1996)]. The complexity of wind-structure interaction has precluded theoretical treatment of the problem. Not only is the approach wind field complex, the flow patterns generated around a structure are complicated because of the distortion in the flow field which occurs as a result of flow separation from sharp corners, vortex formation and wake development.

Flow over bluff bodies and building have been the carried out by numerous researchers. Most of the past research work focused on boundary layer type of wind flow in straight-line wind. Three methods are primarily used to study flow over a bluff body, namely, full-scale tests, wind-tunnel tests and numerical simulation using computational fluid dynamics (CFD).

Given a choice, the best option is to conduct a full-scale test on a real structure but it is difficult to do so practically, considering (a) the high cost of these tests, (b) no control on the experimental parameters including the flow conditions upstream of the structure, and (c) relatively large duration of these tests. Researchers at Texas Tech University (TTU) have been able to collect field data for natural boundary layer wind flow over a building with sides

13.7m by 9.1m by 4m [Levitan (1991), Cochran and Cermak (1992), Wu et al (2001)]. Some field data on a 6m cube at Silsoe, UK, were reported by Richards and Hoxey (2001, 2002).

The closest approach to full-scale field tests is to conduct wind tunnel testing using scaled models. A lot of wind-tunnel work to understand building aerodynamics was directed to replicate the TTU field data [Banks and Meroney (2001), Lin et. al (1995), Cheung et. al. (1997), Okada and Ha (1992),Tieleman et. al (2003)]. Other wind-tunnel simulations of flow over building models were reported by Hunt (1982), Sitheeq et al. (1997), Chang and Meroney (2003) and Haan et al. (1998). Experimental work on bluff bodies using cubic models have also been conducted by Martinuzzi and Tropea (1993) and Castro and Robins (1997). The data from these wind-tunnel studies, particularly from the last two references, have been used by numerous researchers to validate their numerical simulations. The limitations of the wind-tunnel tests are scaling issues as well as blockage effects and correct input of inflow conditions. Also, cost of wind tunnel testing might be prohibitive sometimes.

The last approach is numerical simulation using CFD [Patankar (1981), Anderson (1995), Anderson, Tannehill and Pletcher (1997), Versteeg and Malalasekera (1996)] using different turbulence models. Most flows in nature are turbulent and as such turbulence plays an important role in virtually all engineering problems involving fluid flow and environment. There are three basic methods for simulating turbulence in a multidimensional numerical calculation: direct numerical simulation (DNS), large-eddy simulation (LES) and statistical turbulence models for solving the Reynolds-averaged Navier-Stokes equations (RANS). DNS (Moin and Mahesh, 1998) is not suitable for practical flow problems because the number of grid points required for numerically resolving the motion of small-scale dissipative motion increases as $Re^{9/4}$, and usually in practical flow problems the Reynolds

number is fairly high. Hence, such calculations can be carried out only for fairly low Reynolds numbers and even then the computational effort is very large. Until recently, virtually all calculations were carried out by solving the Reynolds-averaged Navier-Stokes equations (RANS) [Mohammadi and Pironneau (1994)] together with a statistical turbulence model. However, progress in the development of large-eddy simulation (LES) [Sagaut, (2002); Piomelli, (1999)] codes for complex geometries, more universal subgrid-scale models and above all the greatly increased computing power have brought the LES method within reach for solving practical flow problems.

Numerical simulation of flow over buildings and bluff bodies have been reported by Paterson and Apelt (1989), Murakami (1987, 1988), Selvam (1997), Lee and Bienkiewicz (1997), He and Song (1997), Kranjovic and Davidson (2003, 2005), Shah and Ferziger(1997), Yahkot et. al (2006), Lakehal and Rodi (1997), Yu and Kareem (1997) and Nowaza and Tamura (2002).

1.2 Motivation and Background for Current Research

1.2.1 Motivation

The existing literature reveals that microburst type flows, especially its effects on buildings have not been extensively studied in the past as was the case for boundary layer type wind flows in straight-line wind over buildings in the 1960s. The literature review points to the following deficiencies:

1. The velocity field in the vicinity of a building due to a microburst has not been studied in details, unlike boundary layer winds.
2. The effects of parameters like height of jet impingement, jet exit velocities and different building sizes have not been studied in details previously.
3. The effect of a microburst in motion has not been studied in detail. Significant work needs to be done in the area of traveling microburst and their effects on buildings.
4. No full three dimensional numerical simulation has been done to date to investigate microburst-like wind flow effects on building models, either for a static microburst or a traveling microburst.
5. An important requirement for employing numerical simulation to gain insight into the flow physics is accurate specification of the appropriate initial, inlet and boundary conditions from physical experiments. In many of the existing studies, complete sets of data for variables of interest to the numerical analysts are lacking.

In view of the needs for research as listed above, the following tasks are proposed here for this research.

1. Conduct an experimental study to look into the wind fields associated with microburst outflow (wall jet) in more details. Also perform numerical simulations with various turbulence models, and see which model produces results in better agreement with the experimental data.
2. Conduct experimental and numerical simulations to investigate the effects of a static microburst on the surface pressure on buildings. Study the changes in velocity and pressure field due to different nozzle exit velocity, the nozzle to ground distance and different sizes of building.
3. Use Particle Image Velocimetry or PIV (Westerweel, 1993) - a non-intrusive and sophisticated velocity measuring technique, which is well known for spatial resolution and resolve directional ambiguity of the velocity field, to get accurate and detailed measurements of the velocity flow field, especially in the vicinity of the building.
4. Study second-order statistics such as peak pressures and root mean square (rms) of velocity and pressure.
5. Conduct experimental and numerical study of translating microbursts and their effects on the building loads. Use numerical simulation to study effects of higher translation speeds of the microburst (which might not be achievable in the laboratory due to experimental limitations) and see the relative influence of the higher translating speeds on the loads on the buildings. The combined wind velocity experienced at a point as microburst passes, is usually assumed to be the vector sum of the radial impinging jet velocity and the translation velocity. It needs to be verified whether this statement is true.
6. Compare the pressure on structures induced by microburst and regular boundary layer winds.

The proposed research work is a combination of both experimental and numerical simulations of microburst such that each method is able to supplement the shortcomings of the other method. The experimental data will also be used to validate the numerical simulation results.

1.2.2 Microburst: Characteristics and Damage

A microburst occurs within a thunderstorm where the weight of the precipitation and the cooling due to microphysical processes acts to accelerate the air downwards. Observations suggest that approximately five percent of all thunderstorms produce a microburst which is characterized by a strong localized down-flow and an outburst of strong winds near the surface. Wind shear is the term for conditions when strong winds change direction very quickly. This occurs in a microburst when the strong downdraft is suddenly redirected in a horizontal direction as it hits the ground. This weather phenomenon and resulting wind shear were first identified because of the major aircraft disasters they caused. Special types of radar were installed at many airports for identifying these dangerous phenomena.

Fujita (1985) termed microburst as a small downdraft having an outburst of damaging winds with the horizontal extent of the damaging winds being less than 4 km. This definition has been modified by radar meteorologists: they require the peak-to-peak differential Doppler Velocity across the divergent center to be greater than 10 m/s and the distance between these peaks to be less than 4 km. A microburst becomes a “macroburst” if the horizontal distance between outflow peaks exceeds 4 km. Also, microburst winds descend and spread outward, unlike tornado winds, which converge and rise. After striking the ground, the powerful outward running gust can wreak havoc along its path. Damage associated with a microburst is often mistaken for the work of a tornado, particularly directly

under the microburst. However, damage patterns away from the impact area are characteristic of straight-line winds rather than the twisted pattern of tornado damage. Thus, the signature of damage on the ground can be distinguished in a “microburst” compared to a “tornado”. An intense microburst can result in damaging winds near 270 km/hr (170 mph) and often last less than five minutes.

The design wind loads for buildings and other structures are currently based upon model tests in low-speed boundary-layer wind tunnels that generate straight-line winds. However, winds resulting from regular storm events such as thunderstorms are far from being regular atmospheric boundary-layer type events. Thunderstorm winds have significant vertical velocity components and mean horizontal velocity distributions that are different from usual boundary-layer winds (as shown in Figure 1, chapter 2). Also the fact that microburst winds produce higher horizontal velocities at lower heights compared to boundary-layer winds makes low-rise buildings more susceptible to microburst type wind loads compared to boundary-layer winds. It is also believed that the gust structure in a downdraft is much better correlated over its width than in more traditional boundary-layer flow, and hence will lead to larger overall loading of long structures such as long-span bridges or power transmission cables. A traveling microburst produces a different pattern of high winds on the ground compared to a stationary or very slowly moving microburst (Fujita, 1985).

Thunderstorms are responsible for about 1/3 of the extreme gust speeds in the United States (Thom, 1969). In recent studies of extreme wind speeds in the United States, Vickery & Twisdale (1992) found that, outside of hurricane regions, up to 75% of the peak gust wind speeds occurred during thunderstorms. The annual insured property loss from thunderstorm winds in the U.S. is $1.4 billion on an average (data from 1950-1997, Extreme Weather

Sourcebook 2001), which is higher than that caused by tornados ($850 million per year). This damage figure does not include damages due to lightning and flooding—almost all of the damages due to thunderstorms can be assumed to be caused by intense downdraft winds, i.e. microbursts.

Not all microbursts are alike: some are accompanied by heavy rain, while others form beneath virga. Virga is rain that evaporates before it reaches the ground and is associated with a *dry microburst*. The weight of large hail can accelerate falling winds to very high velocities from the upper levels of the atmosphere. Both hail and virga also contribute to accelerating the downdraft by evaporating while falling and thus cooling adjacent air and increasing the weight of the falling air-mass. *Dry microbursts*, which occur over the semiarid western Great Plains and the mountain regions of western North America, typically emerge from a swelling cumulus or cumulonimbus cloud with a high base (10,000 ft or more) that has developed in moist air at middle levels. Most of the precipitation from dry microbursts evaporates before reaching the ground, and the evaporative cooling intensifies the downdraft in the dry low-level air. *Wet microbursts* occur in extremely wet environments east of the Rocky Mountains. These wet downdrafts have nearly saturated lower levels, but there is drier air at middle levels outside the storm; the dry air fuels the evaporative cooling that is necessary to accelerate the downdraft. Wet microbursts are often embedded in heavy rain, and they are sometimes associated with tornados and larger-scale squall line gust fronts. Evaporative cooling of precipitation is suspected as being the primary driving mechanism for most dry microbursts; but for wet microbursts the dominant physical mechanism is still less clear. Prior to the NIMROD (Fujita, 1979) and JAWS (Hjelmfelt, 1987) experiments, it was believed that most microbursts occur in heavy rain. Statistics, however, showed evidence that

the rain drops in the microbursts in dry regions often evaporate completely before reaching the ground.

At the dead center of a microburst, the surface pressure is high and the wind is calm. The high total pressure at the microburst center accelerates the air outwards. The atmospheric pressure decreases as the outflow speed increases, reaching a minimum at the location of the maximum wind-speed. If a stationary microburst spreads inside an undisturbed environment, a perfect starburst outflow with an annular ring of high winds will be observed. In reality, however, the traveling motion of a microburst distorts the airflow from circular to elliptical shape. The front-side wind intensifies while the backside wind weakens resulting in a crescent-shaped area of high winds.

1.2.3 Microburst Flow Simulation and Its Loading Effects

Though there have been numerous studies to study the effects of natural boundary layer flow over buildings, the amount of literature in the area of microburst type of wind loads is scarce. Most of the initial literatures on microbursts were meteorological in nature. Notable among them are the work by Mitchelle and Hovermale (1977), Proctor (1989), Hjemfelt (1987, 1988), Droegemeier and Wilhelmson (1987), Wakimoto (1982), Srivastava (1987). and Orf et al. (1996). The amount of field data is scarce, with some data being available for thunderstorm outflow velocities. Some researchers [Lin and Savory (2006), Kim and Hangan (2007)] have studied the outflow velocity characteristics in the laboratory as well as numerically. Although the main aim is to study the effects of these wind fields over buildings, there is currently no field data available for microburst due to its sudden and random occurrence in nature; less than 5% of all thunderstorms produce a microburst. As such the only possible mechanism to study the effects of microburst type of wind loads on

buildings is through laboratory or numerical simulation. Two methods have been used in general to simulate and study microburst outflow characteristics. These are the impinging wall jet model and the “ring vortex” model.

In the impinging wall jet model, there is a steady flow against a flat plate with or without friction and without buoyancy. This impingement gives rise to a wall jet. The schematic of a wall jet is shown in Figure 1 whereas the schematic for JAWS (Hjelmfelt, 1987) is shown in Figure 2. Although there are no hydrostatic pressure changes in this model, there is an impact pressure field that causes the down flow component to decelerate as air approaches the surface and the horizontal component of the wind to accelerate outward from the impact center

The second type of model has arisen because of the manner in which the descending column of air forms a vortex ring prior to touching the ground. This can be achieved in the laboratory by dropping a volume of heavier fluid into a fluid of lesser density. But after touchdown, it is the radial outflow, which dominates the surface structures and as such the first model seems to replicate the effects of microburst better.

Lundgren (1992), Yao and Lundgren (1996) and Alahyari and Longmire (1995) have conducted several experiments using different temperature fluids in a study of downburst for the aircraft industry and they were able to produce a ring vortex which interacted with the ground plane. But the geometric scale of their simulation was approximately 1:25,000, which is not acceptable for wind tunnel testing of civil engineering structures.

Three dimensional models of a downburst have been developed for aeronautical applications by Zhu and Etkin (1985) (based on a circular doublet-sheet), and by Oseguera

and Bowles (1988) (based on empirical solutions of the continuity equations), but neither of them incorporates the effect of translation speeds.

Jet impingement technique has been used extensively by researchers, mainly to study heat transfer characteristics. Experimental work on jet impingement has been carried out by Cooper et al. (1993), Tsuei (1962), Rajarathnam (1976), Looney and Walsh (1984) and others. A significant number of researchers have used different turbulence models to see their effectiveness by validating with the experimental data of Cooper et al. Numerical studies of impinging jets were performed by Behnia et al. (1998), Dianat et. al. (1996), Craft et. al (1993), Chuang(1989), Voke et al. (1995) and Knowles (1996), to name a few.

Selvam and Holmes (1992) were the first to use an impinging jet model to numerically simulate a microburst. They used a 2D axi-symmetric k-ε model, to simulate the thunderstorm downdraft phenomenon, and were able to demonstrate reasonable agreement between numerical model and limited full-scale data. Holmes (1999) and Letchford and Illidge (1999) undertook physical model studies of a jet impinging on a wall to study topography effects on velocity profiles in a microburst. Wood and Kwok (1999) and Wood et al (2001) also studied static impinging jets, both experimental and numerical (k-ε model), to study topographic effects on velocity profiles. Holmes and Oliver (2000) developed an empirical model of the horizontal wind speed and direction generated by a traveling microburst. Oliver et al. (2000) developed a probabilistic model for design of transmission line systems for high intensity downbursts, assuming that the downburst footprint was roughly rectangular in shape and that the transmission line was a line target. Savory et al. (2001) also studied the effects of failure of lattice transmission towers due to tornado and microburst induced wind loading.

Nicholls et al. (1993) used 2D-LES to study the microburst and its effects on a building model. Mudgal and Pani (1998) used a plane jet to look into the drag effects and wake length for a single sill and effects of a second sill on the first. They also studied the drag force on a cube in both normal and 45^0 angle of incidence to flow. They found that the maximum negative pressure on the cube was twice for normal incidence compared to the 45^0 orientation, though the drag at 45^0 incidence is about 12% higher. Sengupta et al. (2001) studied the pressure distribution on a cubic building and also performed 2D numerical simulation. It was seen that 2D simulations failed to capture the 3D flow physics accurately. Chay and Letchford (2002) also studied the effects of stationary jet on cubic building models. They used one jet height and jet velocity. Letchford and Chay (2002) also used a translating jet (which was moved manually) to see the effects to jet translation speeds. They found that the increased speeds resulted in higher drag. But due to the manual movement of the jet, the validity of some of the data is questionable and looks erratic in nature. Mason et al. (2005) used a pulsed jet to see the outflow characteristics of microbursts due to the roll vortices. Sengupta and Sarkar (2006) used RANS models to simulate the static microburst and compared them with their experimental results. Also recently, Sengupta et al. (2006), Sarkar et al., Sengupta and Sarkar (2007) have reported their findings on laboratory and numerical simulation of both static and translating microbursts and compared them to wind loads on cubic as well as tall buildings due to a translating tornado using the Tornado/Microburst Simulator in the WiST laboratory at Iowa State University.

1.3 Thesis Organization

The dissertation is written in the format of "Thesis Containing Journal Papers". The dissertation includes three manuscripts, out of which the first one (chapter 2) has been submitted for review to the Journal of Wind Engineering and Industrial Aerodynamics. and the other two are ready to be submitted to journals. The second paper (chapter 3) will be submitted to the Journal of Fluids and Structures and the third one (chapter 4) will be submitted to the journal of Engineering Structures. In addition, a general introduction chapter appears at the beginning and a conclusion and recommendation's chapter is included at the end of the dissertation. All numerical simulations reported in this dissertation were conducted using commercial CFD software, FLUENT (2005).

The first journal paper deals with the experimental and numerical simulation of a type of thunderstorm, namely microburst, to study the outflow velocity characteristics. The microburst is simulated as a round jet, impinging onto a flat plate. A systematic study of different parameters like the height of impinging jet, jet exit velocity, was conducted experimentally to see their effects on the velocity profiles as well as pressure distribution on the ground. Different experimental techniques like hotwire, pressure rakes and PIV were used to measure the velocity profiles at various locations. The horizontal velocity profiles from experiments agree well with the empirical profiles of other researchers like Rajaratnam (1976) and Wood et al. (2001), and a new set of constants for an old empirical equation is proposed for horizontal velocity distribution. New empirical equations are proposed for predicting the boundary layer growth and the maximum radial velocity as a function of distance from the center of jet. The validity of these equations was checked with the experimental data of other researchers and was found to agree well.

The numerical simulations were initially tested with the k-ε turbulence model to determine the applicability of proper boundary conditions and extent of the numerical domain. Different turbulence models were then used with these boundary conditions and numerical domain to determine their applicability to this type of flow. Comparison of numerical and experimental results was made. There is a good agreement between axial velocity profiles of the jet obtained from experiments (hot wire) with those obtained with various numerical turbulence models. The normalized horizontal velocity profiles computed numerically with various models match closely with the experimental results for different r/D values. All the numerical models capture the trend of the boundary layer growth and decay of maximum radial velocities with increasing radial distance, but the predicted values from LES, realizable k-ε and RSM models match the experimental data better than the other three models.

In terms of pressure distribution, the ground pressure coefficients from experiments and numerical simulation agree very well. Also the pressure distribution on a cube placed at a distance of 1D from the center of the jet, computed numerically agree well compared to experimental data for the front and back sides of the cube. On the roof, LES is able to capture flow separation better, resulting in improved prediction of roof pressures compared to under prediction of pressure on the roof with other turbulence models. The empirical equations derived here from the experimental data have potential application in the design of civil engineering structures for winds generated by a microburst.

The second journal paper deals with the pressure distribution and aerodynamic loading on cubic buildings under static microburst type wind loads. Two different building models were tested experimentally and loads resulting from the static impinging jets at various heights, jet

exit velocities and distances from the building model were studied. It was found that the larger building experiences more loads compared to the smaller one in a region close to the center of the jet. Also for a microburst, the building experiences a downward force when it is directly under the center of the jet, which is not seen for regular atmospheric boundary layer type winds. Varying the jet height did not produce a significant change in the loads on the building, though it was seen that at jet height 2D, the coeffients are somewhat higher in a majority of jet locations from the center of the building models.

The reliability of numerical simulation to simulate microburst type wind loads on cubic building was studied using different RANS and LES turbulence models. The results of numerical simulation were compared to the experimental data. Amongst all the turbulence models tested, LES gave superior results compared to RANS models in most situations. Pressures on the cube computed numerically agree well compared to experimental data for the front and back sides of the cube. Separation occured on the roof at some jet locations, and none of the RANS models were able to capture it. LES was able to capture the separation on the roof with remarkable accuracy, and hence led to better prediction of the roof pressures. The peak loads from the experiments were also compared to the LES results.

The flow field around the building was studied at two building locations, namely $0.0D_J$ and $1.0D_J$ from the center of the jet, where D_J is the diameter of the jet. PIV was used for this purpose. Again it was found that LES simulated the wind field around the buildings better than the RANS models. Favorable agreement between numerical and experimental studies indicates that CFD can be used effectively for this kind of complex flow.

The third journal paper reports the numerical simulation of a moving jet and its effects on a cube shaped bluff body. The simulation replicates a translating microburst that occurs

commonly in nature. Initially the wind loads on the two building models that are mentioned in journal paper 2, resulting from a translating microburst at one speed of jet translation, were studied experimentally (jet translation speed to jet velocity ratio V_{TR} = 0.225). The pressure distribution on the ground was also measured under the translating impinging jet. Velocities were measured at two different heights for the translating jet and compared to LES results.

Large eddy simulation (LES) and RANS were used to numerically simulate four different translating speeds of the microburst, including the one achieved experimentally. Based on the conclusion that LES produced superior results compared to RANS models as seen in the case of a static jet (journal paper 2), LES was used more extensively for the moving jet simulations. Jet motion was simulated numerically using both the sliding mesh and dynamic mesh techniques. LES was able to predict the fluctuating loads which the RANS models failed to capture. The peak force coefficients for the microburst were determined for different translating speeds. Peak drag coefficient was observed to monotonically increase with higher microburst translation speed, whereas the peak lift coefficient remained the same for a range of speeds until a critical speed of S4 was reached when positive (or upward force) peaks resulted along with higher negative peaks of lift force. The ground pressure distribution as well as the transient velocity profiles from LES simulations compared well with that of the experiments. Microburst can produce loads on buildings equivalent to that generated by a F2 tornado.

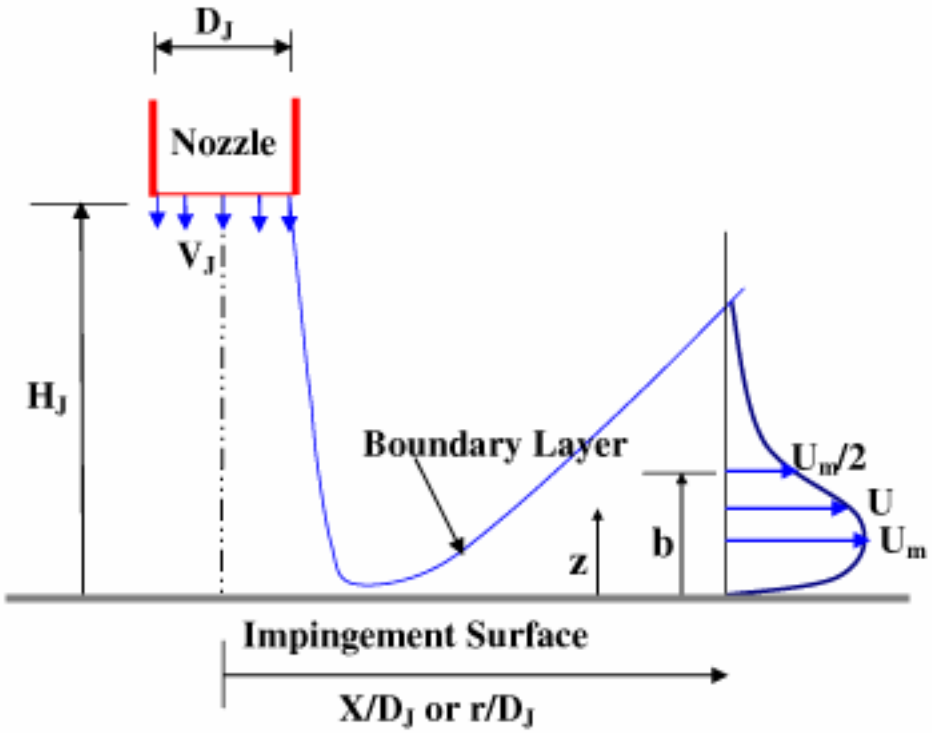

Figure 1: Schematic of impinging jet and subsequent wall jet formation

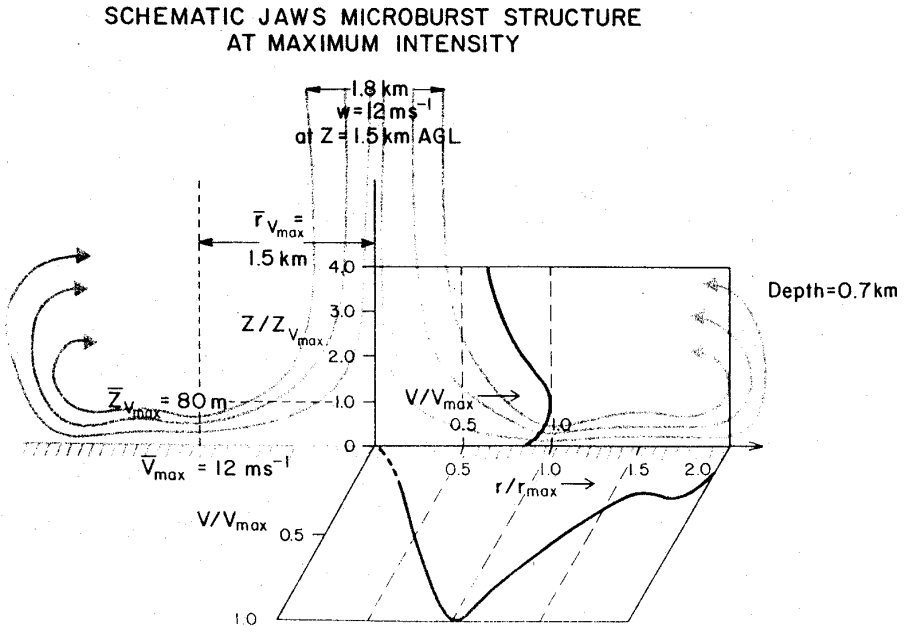

Figure 2: JAWS microburst Schematic (Hjmfeldt,1987)

References

Alahyari, A., and Longmire, E.K., (1995) Dynamics of Experimentally Simulated Microbursts. AIAA Journal. 33(11), 2128- 2136.

Anderson, J. D. (1995) Computational Fluid Dynamics: The Basics with Applications. McGraw-Hill.

Anderson, D.A., Tannehill, J.C. and Pletcher, R.H. (1997) Computational Fluid Mechanics and Heat Transfer. Taylor and Francis. Washington, D.C.

Banks, D. and Meroney, R.N. (2001) The applicability of quasi-steady theory to pressure statistics beneath roof-top vortices. J. Wind Eng. Ind. Aerodyn 89, 569-598.

Cochran, L.S. and Cermak, J.E. (1992) Full and model-scale cladding pressures on the Texas Tech University experimental building. J. Wind Eng. Ind. Aerodyn. 41-44, 1589-1600.

Behnia, M., Parneix, S., and Durbin, P.A. (1998) Prediction of heat transfer in a axisymmetric turbulent jet impinging on a flat plate. Int. J. Heat Mass Transfer 41(12), 1845-1855.

Castro, I.P. and Robbins, A.G. (1977) The flow around a surface-mounted cube in uniform and turbulent streams. J. Fluid Mechanics 79(2), 307-335

Chang, C.H. and Meroney, R.N. (2003) The effect of surroundings with different separation distances on surface pressures on low-rise buildings. J. Wind Eng. Ind. Aerodyn. 91,1039-1050.

Chay M.T. and Letchford C.W. (2002) Pressure distributions on a cube in a simulated thunderstorm downburst. Part A: stationary downburst observations. J. Wind Eng. Ind. Aerodyn. 90, 711-732.

Cheung, J.C.K, Holmes, J.D., Melbourne, W.H., Lakshmanan, N. and Bowditch. P. (1997) Pressures on a 1/10 scale model of the Texas Tech Building. J. Wind Eng. Ind. Aerodyn. 69-71, 529-538.

Chuang, S.H. (1989) Numerical Simulation of an Impinging Jet on a Flat Plate. Int. J. Numer. Meth. Fluids 9, 1413-1426.

Cook, N.J. (1990) The designers guide to wind loading on structures. Butterworth, London.

Cooper, D., Jackson, D.C., Launder, B.E., and Liao, G.X., (1993) Impinging Jet Studies for Turbulence Model Assessment-I: Flow-Field Experiments. Int. J. Heat Mass Transfer 36(10), 2675-2684.

Craft, T.J., Graham, L.J.W., and Launder, B.E. (1993) Impinging Jet Studies for Turbulence Model Assessment-II: An Examination of the Performance of Four Turbulence Models. Int. J. Heat Mass Transfer 36(10), 2685-2697.

Dianat, M., Fairweather, M., and Jones, W.P. (1996) Reynolds Stress Closure Applied to Axisymetric Impinging Turbulent Jets. Theoretical and Computational Fluid Dynamics 8, 435-447.

Dianat, M., Fairweather, M., and Jones, W.P. (1996) Predictions of Axisymmetric two-dimensional Impinging Turbulent Jets. Int. J. Heat Fluid Flow 17, 530-538.

Droegemeier, K.K. and Wilhelmson, R.B (1987) Numerical Simulations of Thunderstorm Outflow Dynamics. Part I: Outflow Sensitivity Experiments and Turbulence Dynamics. J. Atmospheric Sciences 44(8), 1180-1210.

Fluent. (2005) FLUENT *User's Guide:* Release 6.2. Fluent, Inc. Lebanon. New Hampshire.

Fujita, T. T. (1979) Objectives, operations and results of project NIMROD. Preprints, 11th Conf. on Severe Local Storms. Kansas City, Amer. Meteor. Society, 259-266.

Fujita, T. T. (1985) *The Downburst: Microburst and Macroburst.* University of Chicago Press.

Haan, F.L., Kareem, A. and Szewczyk, A.A. (1998) The effects of turbulence on the pressure distribution around a rectangular prism. J. Wind Eng. Ind. Aerodyn 77&78, 381-392.

Haan, F.L., Sarkar, P.P. and Gallus, W.A. (2007) Design, construction and performance of a large tornado simulator for wind engineering applications. Engineering Structures(to appear).

He, J. and Song, C.C.S. (1997) A numerical study of wind flow around the TTU building and the roof corner vortex. J. Wind Eng. Ind. Aerodyn 67 & 68, 547-558.

Hjelmfelt, M.R. (1987) The Microbursts of 22 June 1982 in JAWS. J. Atmospheric Sciences 44(12), 1646-1665.

Hjelmfelt, M.R. (1988) Structure and life cycle of microburst outflows observed in Colorado. J. Applied Meteorology 27, 900-926.

Holmes, J. D (1999) Modeling of Extreme Thunderstorm Winds for Wind Loading of Structures and Risk Assessment. Wind Engineering into the 21st Century, Proc. of the 10th Intl. Conf. on Wind Eng. eds. A. Larsen et al., Denmark, June 1999, 1409–1415.

Holmes, J. D. and Oliver, S.E. (2000) An Empirical Model of a Downburst. Engineering Structures 22, 1167-1172.

Hunt, A. (1982) Wind-tunnel measurements of surface pressures on cubic building models at several scales. J. Wind Eng. Ind. Aerodyn 10, 137-163

Kim J. and Hangan H. (2007) Numerical simulation of impinging jets with application to downbursts. J. Wind Eng. Ind. Aerodyn 95, 279-298.

Knowles, K. (1996) Computational Studies of Impinging Jets using k-e Turbulence Models. Int. J.Numer. Meth. Fluids 22, 799-810.

Kranjovic, S. and L. Davidson, L. (2003) Numerical Study of the flow around the bus-shaped body. ASME: J. Fluids Eng. 125, 500-509.

Kranjovic, S. and L. Davidson, L. (2005) Flow around a simplified car, part I: large eddy simulation. J. Fluids Engng. 127 (5), 907-918.

Lakehal, D. And Rodi, W. (1997) Calculation of the flow past a surface-mounted cube with two-layer turbulence models. J. Wind Eng. Ind. Aerodyn. 67 & 68, 65-78.

Lee, S. and Bienkiewicz, B. (1997) Large-eddy simulation of wind effects on bluff bodies using the finite element method. J. Wind Eng. Ind. Aerodyn. 67 & 68, 601-609.

Letchford, C.W., and Illidge, G., (1999) Turbulence and Topographic effects in Simulated Thunderstorm Downdrafts by Wind Tunnel Jet. Wind Engineering into the 21st Century, Proceedings of the Tenth International Conference on Wind Engineering. eds. A. Larsen G. L. Larose and F. M. Livesey, Denmark, June 1999, 1907-1912.

Levitan, M.L., Holmes, J.D., Mehta, K.C. and Vann, W.P. (1989) Field measurement pressures on the Texas Tech building. J. Wind Eng. Ind. Aerodyn. 38, 227-234.

Letchford C.W. and Chay M.T., (2002) Pressure distributions on a cube in a simulated thunderstorm downburst. Part B: moving downburst observations. J. Wind Eng. Ind. Aerodyn. 90, 733-753.

Lin, J.X., Surry, D. and Tielelam, H.W. (1995) The distribution of pressure near roof corners of flat roof low buildings. J. Wind Eng. Ind. Aerodyn., 56, 235-265.

Lin, W.E. and Savory, E. (2006) Large-scale quasi-steady modeling of a downburst outflow using a slot jet. Wind and Structures. 9, 209-220.

Looney, M.K. and J.J. Walsh, J.J (1984) Mean-flow and Turbulent Characteristics of Free and Impinging Jet Flows. J. Fluid Mech. 147, 397-429.

Lundgren, T. S., Yao, J. and N. N. Mansour, N.N. (1992) Microburst Modeling and Scaling. J. Fluid Mech. 239, 461-488.

Mason, M.S. Letchford, C.W. and James, D.L. (2005) Pulsed wall jet simulation of a stationary thunderstorm downburst, Part A: Physical structure and flow field characterization. J. Wind Eng. Ind. Aerodyn. 93, 557-580.

Martinuzzi, R. and Tropea, C. (1993) The flow around surface-mounted, prismatic obstacles placed in a fully developed channel flow. J. Fluids. Engng. 115, 85-91.

Mitchell, K.E. and Hovermale, J.B. (1977) A Numerical Investigation of the Severe Thunderstorm Gust Front. Monthly Weather Review. 105, 657-677.

Mohammadi, B. and Pironneau, O. (1994) Analysis of the K-Epsilon Turbulence Model. John Wiley & Sons.

Moin, P. and Mahesh, K. (1998) Direct numerical simulation: A tool in turbulence research. Ann. Rev. Fluid Mech. 30, 539-578

Mudgal, B.V. and Pani, B.S. (1998) Flow around obstacles in plane turbulent wall jets. J. Wind Eng. Ind. Aerodyn. 73(3&4), 193-213.

Murakami, S., Mochida, A. (1988) 3D Numerical Prediction of Turbulent Flow around Buildings by k-ε Model. Building and Environment, 24 (1).

Murakami, S., Mochida, A. and Hibi, K. (1987) Three-dimensional Numerical Simulation of Air Flow around a Cubic Model by means of Large Eddy simulation. J. Wind Eng. Ind. Aerodyn. 25, 291-305.

Nicholls, M., Pielke R., and Meroney, R., (1993) Large eddy simulation of microburst winds flowing around a building. J. Wind Eng. Ind. Aerodyn. 46-46, 229-237.

Nozawa, K. and Tamura, T. (2002) Large eddy simulation of the flow around a low-rise building immersed in a rough-wall turbulent boundary layer. J. Wind Eng. Ind. Aerodyn. 90, 1151-1162.

Okada, H. and Ha, Y.C. (1992) Comparison of Wind Tunnel and Full-Scale Pressure Measurement Tests on Texas Tech Building. J. Wind Eng. Ind. Aerodyn. 43,1601-1612.

Oliver, S.E., Moriarty, W.W. and Holmes, J.D. (2000) A Risk Model for Design of Transmission Line Systems against Thunderstorm Downburst Winds. Engineering Structures, 22, 1173-1179.

Orf, L.G., Anderson, J.R. and Straka, J.M. (1996) A Three Dimensional Numerical Analysis of Colliding Microburst Outflow Dynamics. J. Atmospheric Sciences. 53(17), 2490-2511.

Oseguera, R. M. And Bowles, R. L. (1988) A simple, analytic 3-dimensional downburst model based on boundary layer stagnation flow. NAS 1.15100632; NASA-TM-100632

Paterson, D.A. and Apelt, C.J. (1989) Simulation of Wind Flows Around 3-D Buildings. Building and Environment. 24, 39-50.

Patankar, S.V. (1981) Numerical Heat Transfer and Fluid Flow. McGraw-Hill.

Piomelli, U. (1999) Large-eddy simulation: achievements and challenges. Progress in Aerospace Sciences 35, 335-362.

Proctor, F.H. (1989) Case Study of a Low-Reflectivity Pulsating Microburst: Numerical Simulation of the Denver, 8 July 1989, Storm. 17th Conference on Severe Local Storms, St, Louis, Missouri. 677-680.

Rajarathnam, N., (1976) Turbulent Jets. Elsevier Scientific Publishing Company.

Sagaut, P. (2002). Large Eddy Simulation for Incompressible Flows: An Introduction. 2nd Ed. Springer.

Richards, P.J., Hoxey, R.P. and Short, L.J. (2001) Wind Pressures on a 6 m cube. J. Wind Eng. Ind. Aerodyn. 89. 1553-1564.

Richards, P.J. and Hoxey, R.P. (2002) Unsteady flow on the sides of a 6 m cube. J. Wind Eng. Ind. Aerodyn. 90. 1855-1866.

Sarkar, P.P., Haan, F.L., Balaramudu, V. and Sengupta, A., (2006) Laboratory simulation of tornado and microburst to assess wind loads on buildings. Proc. ASCE Structures Congress, St. Louis, USA.

Savory, E., Parke, G.A.R., Zeinoddini, M., Toy, N. and Disney, P. (2001). Modeling of a Tornado and Microburst-induced Wind loading Failure of a Lattice Transmission Tower. Engineering Structures. 23, 365-375.

Selvam, R.P., and Holmes, J.D. (1992) Numerical Simulation of Thunderstorm Downdrafts. J. Wind Eng. Ind. Aerodyn. 41-44. 2817-2825.

Selvam, R. P. (1997) Computation of pressures on Texas Tech University building using large eddy simulation. J. Wind Eng. Ind. Aerodyn. 67 & 68, 647-657.

Sengupta, A. and Sarkar, P.P. and Rajagopalan, G.R. (2001) Numerical and physical simulation of thunderstorm downdraft winds and their effects on buildings. 1st Americas Conference on Wind Engineering, 4-6 June, Clemson, SC.

Sengupta, A. and Sarkar, P.P. (2006) Physical and numerical simulation of microburst-like wind: A study of flow characteristics and surface pressures on a cube. Proc. 3rd Indian National Conf. on Wind Engineering. Kolkata, India.

Sengupta. A., Haan, F.L., Sarkar. P.P. and Balaramudu, V. (2006) Transient loads on buildings in microburst and tornado winds. Proc. 4th Intl. Symp. on Computational Wind Engineering (CWE2006). Japan, July 16–19.

Sengupta. A. and Sarkar. P.P. (2007) Computational and experimental simulation of static and transient loads on buildings in microburst winds. Proc. 12th International Conference on Wind Engineering, Cairns, Australia, July 1-6.

Shah, K.B. and Ferziger, J.H. (1997) A fluid mechanicians view of wind engineering: large eddy simulation of flow past a cubic obstacle. J. Wind Eng. Ind. Aerodyn. 67/68, 211-224.

Simiu, E. and Scanlan, R.H. (1996) Wind Effects on Structures. 3rd Ed. John Wiley & Sons, New York.

Sitheeq, M.M., Iyengar, A.K.S. and Farell, C. (1997) Effect of turbulence and its scales on the pressure field and surface of a three-dimensional square prism. J. Wind Eng. Ind. Aerodyn., 69-71, 461-471.

Srivastava, R.C. (1987) A model of intense downdrafts driven by the melting and evaporation of precipitation. J. Atmos. Sci., 44 (13) 1752-1773.

Thom, H.C.S. (1969) New distributions of extreme wind speeds in the United States. J. Structures Div., ASCE, 94, 1787-1801.

Tieleman, H.W., Ge, Z., Hajj, M.R. and Reinhold, T.A. (2003) Pressures in a surface-mounted rectangular prism under varying incident turbulence. J. Wind Eng. Ind. Aerodyn. 91, 1095-1115.

Tsuei, Y.G., (1962) Axisymmetric Boundary Layer of a Jet Impinging on a Smooth Plate. PhD Dissertation, Colorado State University, Fort Collins, Colorado.

Versteeg, H. K. And Malalasekera (1996) An Introduction to Computational Fluid Dynamics: The Finite Volume Method. Addison Wesley Longman Limited.

Vickery, P. J. and Twisdale, L.A. (1995) Analysis of thunderstorm occurrences and wind speed statistics. J. Wind Eng. Ind. Aerodyn. 55, 813-821.

Voke, P.R. Gao, S. and Leslie, D. (1995) Large-Eddy Simulations of Plane Impinging Jets International Journal For Numerical Methods In Engineering, 38, 489-507.

Wakimoto, R. M. (1982) The life cycle of thunderstorm gust fronts as viewed with Doppler radar and Rawinsonde data. Month. Weather. Rev. 110, 1060-1082

Westerweel, J. (1993) Digital Particle Image Velocimetry: Theory and Application. Delft University Press, Delft.

Wood, G. S and K. C. S. Kwok, (1999) Physical and Numerical Modeling of Thunderstorm Downbursts. Wind Engineering into the 21st Century, Proc. of the 10th Intl. Conf. on Wind Eng., eds. A. Larsen et al., Denmark, June 1999, 1919–1924.

Wood, G.S., Kwok, C.S., Motteram, N.A., and Fletcher, D.F., (2001) Physical and Numerical Modelling of Thunderstorm Downbursts. J. Wind Eng. Ind. Aerodyn. 89, 535-552.

Wu, F., Sarkar, P.P. and Mehta, K.C. (2001) Full-scale study of conical vortices and roof corner pressures. Wind and Structures. 4(2) 131-146

Yao, J. and Lundgren, T.S. (1996) Experimental Investigation of Microbursts. Experiments in Fluids. 21, 17-25.

Yakhot, A., Anor, T., Liu, H. and Nikitin, N. (2006) Direct numerical simulation of turbulent flow around a wall-mounted cube: spatio-temporal evolution of large-scale vortices. J. Fluid Mech. 566, 1-9.

Yu, D. and Kareem, A. (1997) Numerical simulation of flow around a rectangular prism. J. Wind Eng. Ind. Aerodyn. 67/68, 195-208.

Zhu, S. and Etkin, B. (1985) Model of the Wind Field in a Downburst. J. Aircraft. 22. 595-601.

CHAPTER 2

EXPERIMENTAL AND NUMERICAL SIMULATION OF THUNDERSTORM MICROBURST WINDS USING AND IMPINGING JET MODEL

A paper submitted to the Journal of Wind Engineering and Industrial Aerodynamics

Anindya Sengupta[1, 2] and Partha P. Sarkar[1, 3]

Abstract:

Wind profiles and characteristics in a thunderstorm downburst are significantly different than that of regular boundary layer winds. This paper deals with the experimental and numerical simulation of a type of thunderstorm event, namely microburst, to study the outflow velocity characteristics. The microburst is simulated as a round jet, impinging onto a flat plate. A generic empirical equation for radial velocity profile is developed based on the experimental data, using hotwire, pressure rakes and PIV. The experimental results are used to validate CFD simulations and to find the applicability of different turbulence models for this kind of flow. Favorable agreement between numerical and experimental studies indicates that CFD can be used for this kind of complex flow.

Keywords: Microburst simulation; Impinging jet; RANS Turbulence Models; LES; PIV measurements; Velocity profile; Boundary-layer growth; Microburst wind-loads

[1] Graduate Student and Professor respectively, Department of Aerospace Engineering, Iowa State University
[2] Primary researcher and author
[3] Author for correspondence

1. Introduction

The current design wind loads for buildings and other structures are based upon model tests in low-speed boundary-layer wind tunnels that generate straight-line winds. However, winds resulting from regular storm events such as thunderstorms are far from being regular atmospheric boundary-layer type events. Thunderstorm winds have significant vertical velocity components and mean horizontal velocity distributions that are different from usual boundary-layer winds (as shown in Figure 1). It is also believed that the gust structure in a downdraft is much better correlated over its width than in more traditional boundary-layer flow, and hence will lead to larger overall loading of long structures such as long-span bridges or power transmission cables.

Thunderstorms are responsible for about 1/3 of the extreme gust speeds in the United States (Thom, 1969). In recent studies of extreme wind speeds in the United States, Vickery and Twisdale (1995) found that, outside of hurricane regions, up to 75% of the peak gust wind speeds occurred during thunderstorms.

The current research focuses on simulation of a stationary microburst using both experimental and numerical methods. The microburst is modeled as an impinging jet. Jet impingement is a technique for enhancing heat transfer that is used in a variety of cooling applications from electronics to gas turbines. An intensive parametric study was conducted with different jet exit velocities, height of jet above impingement surface and different nozzle diameters.

Experimentally, the microburst is modeled as a jet coming out of a duct and impinging on a wooden platform placed below. This facility consists of a wooden surface on an adjustable base mounted perpendicular to a round jet nozzle as shown in Figure 2a. A small centrifugal

fan serves as the air supply and is mounted on top of the nozzle. The jet to surface height can be varied from 203 mm (8") to 826 mm (32.5"). The jet was operated at 2 different velocities, 10 m/s and 16 m/s, resulting in a Reynolds number of 1.4 x 10^5 and 2.2 x 10^5, respectively, based on the diameter of the jet exit nozzle and jet exit velocity. Hot-wire anemometry, pressure rakes and Particle Image Velocimetry (PIV) techniques were used for measuring the velocity profiles. Digital pressure transducers were used to measure the pressures on the ground plane. The PIV and pressure measurement setups are shown in Figure 2a.

Different turbulence models, such as k-ε and its variants, k-ω, Reynolds Stress Model (RSM) and Large Eddy Simulation (LES) with different boundary conditions and size of computational domain were used to determine the best possible numerical scheme for simulation of the flow-field in a microburst. Commercial CFD software FLUENT (2003) was used for this purpose.

2. Background and Motivation

Microbursts occur in thunderstorms where the weight of the precipitation and the cooling due to microphysical processes act to accelerate the air downwards. Observations suggest that approximately five percent of all thunderstorms produce a microburst which is characterized by a strong localized down-flow and an outburst of strong winds near the surface. Wind shear is the term for conditions when strong winds change direction very quickly. This occurs in a microburst when the strong downdraft is suddenly redirected in a horizontal direction as it hits the ground. This weather phenomenon and resulting wind shear

were first identified by Fujita and his co-workers because of the major aircraft disasters they caused.

Fujita (1985) termed microburst as a small downdraft having an outburst of damaging winds with the horizontal extent of the damaging winds being less than 4 km. This definition has been modified by radar meteorologists: they require the peak-to-peak differential Doppler velocity across the divergent center to be greater than 10 m/s and the distance between these peaks be less than 4 km. A microburst becomes a "macroburst" if the horizontal distance between outflow peaks exceeds 4 km. Also, microburst winds descend and spread outward, unlike tornado winds, which converge and rise. After striking the ground, the powerful outward running gust can wreak further havoc along its path. Damage associated with a microburst is often mistaken for the work of a tornado, particularly if the damage is directly under the microburst. However, damage patterns away from the impact area are characteristic of straight-line winds rather than the twisted pattern of tornado damage. Thus, the signature of damage on the ground can be distinguished in a "microburst" compared to a "tornado". An intense microburst can result in damaging winds with a maximum speed of 270 km/hr (170 mph) that often last for less than five minutes.

Selvam and Holmes (1992) undertook numerical modeling of the thunderstorm downdraft phenomenon and were able to demonstrate reasonable agreement between a numerical model (k-ε) and limited full-scale data. Holmes and Oliver (2000), Letchford and Illidge (1999) and Wood and Kwok (1999) undertook physical model studies of a jet impinging on a wall to study topographic effects on velocity profiles in a microburst. Chay and Letchford (2001) measured velocity profiles on a ground plane in a stationary microburst using an inverted impinging jet. In some of these studies, the comparison of horizontal

velocity profiles with those recorded in full scale has shown that impinging jets do a fairly good job in capturing the mean velocities in a steady-state downdraft. In reality, the microburst is a very short-term phenomenon and usually translates horizontally. A ring vortex has been observed to form in a microburst as the leading edge of the downdraft interacts with the ground and the flow spreads outwards. The horizontally translating ring vortex in a stationary or moving microburst is expected to produce dynamic effects on the velocity profiles. Lundgren et al (1992), Yao and Lundgren (1996) and Alahyari and Longmire (1995) have conducted several laboratory experiments using fluids of different density in a study of downburst for the aircraft industry. They were able to incorporate the effect of buoyancy in their simulation and produce a ring vortex. Other experimental investigations of jet impingement on flat surfaces were performed by Tsuei (1962), Donaldson and Snedeker (1971), Didden and Ho (1985) and Knowles and Myszko (1998).

The impinging jet flow has been a particularly challenging case for numerical turbulence models. The stagnation region flow is dominated by normal straining of the fluid and many of the widely used models, which have been developed primarily for shear flow boundary layers fail to predict the response of the turbulence to normal straining. Craft et al (1993) reported predictions of the flow using four different turbulence models using the experimental results of Cooper et al (1993). They concluded that standard linear eddy-viscosity models significantly over-predict turbulence energy levels (and thus heat-transfer rates) in the stagnation region, as a result of the linear Boussinesq stress-strain relation misrepresenting the normal stresses and leading to excessive turbulence energy generation rates. They also reported predictions employing stress-transport models. They showed that the linear IP model, when used in conjunction with the wall-reflection terms of Gibson and

Launder (1978), gave results that were slightly better than the linear EVM model. This failure was due to the form of the wall-reflection terms, which were developed by considering flow parallel to a wall, and actually have the effect of increasing the stress normal to the wall in impinging flow. When these were replaced with the proposed model of Craft et al (1997), which was designed to predict flows both parallel and normal to a wall, reasonable predictions were obtained. Myszko and Knowles (1995) found out that the standard k-e model failed to accurately predict the thickness of the wall jet. Yamamoto (1997) used a multiple-time-scale Reynolds stress model to show reasonable agreement with experimental data for mean velocity profiles and growth rates. Dianat et al (1996) found out that the inclusion of a wall reflection term in the Reynolds stress closure model resulted in better predictions of the mean velocities. Recently the v2f model (Behnia et al, 1998) has shown a lot of promise in predicting the behavior of turbulent impinging jets.

The existing literature reveals that impinging jets have been extensively (but not exhaustively) studied in the past, especially for the case of jet impingement in a stagnant environment or in a co-flow configuration. However, a systematic parametric study of the impinging jet, such as variation of jet diameter, jet exit velocity and height of jet with respect to ground plane using multiple flow-measurement instruments (hotwire, PIV and pressure rake) has not been undertaken in previous laboratory simulations of microburst. An important requirement for employing numerical simulation to gain insight into the flow physics is accurate specification of the appropriate initial, inlet and boundary conditions from physical experiments. In many of the existing numerical studies of microburst simulation there was only a limited set of laboratory data available to the numerical analyst for comparison. Data sets from a parametric study would be very useful in validating CFD results.

The primary objectives of the present work were: (a) to perform a systematic parametric study of laboratory simulation of stationary and moving microburst using an impinging jet to determine the flow characteristics, (b) application of CFD to simulate the microburst phenomenon with jet impingement using different turbulence models, (c) comparison of CFD results with those of the experiments to determine the most suitable turbulence model, computational domain and boundary conditions, (d) study of pressure distribution on two cube-shaped buildings in a microburst using both numerical and experimental models to determine the effects of size of the building and its location with respect to the center of the microburst and also determine the most suitable turbulence model. This paper presents results from the work related to all the above objectives except objective (d) and a moving microburst that will be presented in a separate paper.

3. Experimental Setup

The experimental setup is shown in Figure 2. A nozzle diameter (D) of 203 mm (8 in.) was used to produce the jet. The distance (H) of the ground plane or impinging platform (L = 2.44 m (96 in.) and B = 1.22 m (48 in.) from the nozzle could be varied from a minimum of 203 mm (8 in.) to a maximum of 826 mm (32.5 in.) using a mechanical jack. A honeycomb and two screens were used to reduce the turbulence of the issuing jet. A 3:1 area contraction was used at the nozzle end to make the velocity of the issuing jet uniform. For the current work, H = 206 mm (8.125 in.), H/D = 1.02; H = 403 mm (15.875 in.), H/D = 1.98; and H = 587 mm (23.25 in.), H/D = 2.91 were used. Henceforth, these three heights are termed as H1, H2 and H3, respectively. The H/D ratio for this study was chosen to be within the range of H/D values of a microburst that varies between 0.75 and 7.5. Two jet velocities were used, V_j

≈ 10 m/s (32.8 ft/s) and V_j ≈ 16 m/s (52.5 ft/s). Henceforth, these two velocities are termed as V1 and V2, respectively. The velocity profiles were measured at different r/D ratios, where r is the radial distance from the centerline of the jet, ranging from 0.5 to 3.0 (Figure 2b).

3.1 Velocity Measurement

A PIV system was used for non-intrusive velocity measurements. To obtain PIV measurements, the flow was homogeneously seeded with tracer particles (olive oil). In PIV, it is assumed that the particles are small enough to move with the local flow velocity. A plane within the flow is illuminated twice within a short interval of time by a laser sheet. A CCD sensor records on separate frames the light from each pulse scattered by the tracer particles. It is possible to identify the path that a particle has traveled by analyzing one image pair. Knowing the time delay between two pulses, one can calculate the velocity. The time interval between the two laser shots was adjusted according to the mean flow velocity and the magnification of the camera lens. The PIV system consists of a laser sheet generated by a 120mJ double pulsed Nd:YAG laser with a maximum repetition rate of 15 Hz per laser head. The CCD camera is a 12 bit camera capable of taking 8 single frames per second, with a minimum inter-framing time of 300 ns.

Two hundred fifty samples were collected for each run to ensure convergence of statistical quantities, like mean and rms (root mean square) velocity of the flow field. Subsequently, 5-10 runs were conducted at each location to ensure that experimental uncertainties are reduced. An initial interrogation window size of 64 x 64 pixels and a final initial interrogation window size of 32 x 32 were used with 50 % overlap, resulting in a grid

spacing of 16 pixels. An adaptive multi-pass filter with decreasingly smaller window sizes (2 passes) was used.

Single-probe hot-wire measurements were also performed to measure the axial velocities under the jet as well as the radial velocity profiles at various distances, r, from the centerline of the jet (Figure 2b). From hot-wire measurements, the turbulence intensity of axial velocities in the jet was found to lie between 1.0 – 2.0 %.

A boundary-layer rake consisting of 16 pitot-static tubes was also used to measure the radial velocities at different r/D ratios. The first tube was placed at a height of 2 mm and the last one was at 140 mm from the ground plane with a uniform spacing of 9.2 mm between the tubes. The pressure rake was connected to a Scanivalve pressure transducer (DSA 3217).

3.2 Pressure Measurement

Pressures on the ground plane, directly beneath the jet, were measured using 25 taps. One tap was placed directly under the center of the jet and 12 taps were placed on either side of it in a straight line at an interval of 25.4 mm (1”). Two Digital Sensor Arrays (DSA 3217, 16 Channel) Scanivalve pressure transducers were used for measuring both the static and fluctuating surface pressures. The DSA 3217 is a stand-alone temperature compensated electronic pressure scanner with a pressure range of ±10 inches of H_2O. Each DSA incorporates sixteen individual, temperature compensated, piezo-resistive pressure sensors with an A/D converter and a microprocessor to create an intelligent gas pressure measurement system. The maximum data acquisition rate for the scanner was 200 samples/channel/sec. A Binary Telnet program, BTEL.EXE, which is a support program for the DSA module along with DSA Link, was used for pressure data acquisition. BTEL can receive and save BINARY formatted data from the DSA to a file. It then converts the binary

data to ASCII, in a format compatible with spreadsheet programs, like Excel. The data acquisition (using BTEL and DSA Link), was facilitated with a PC running the Windows NT operating system.

4. Numerical CFD Modeling

Reynolds Averaged Navier-Stokes (RANS) equations are given by:

$$\frac{\partial \rho}{\partial t} + \frac{\partial}{\partial x_i}(\rho u_i) = 0 \tag{1}$$

and

$$\frac{\partial}{\partial t}(\rho u_i) + \frac{\partial}{\partial x_j}(\rho u_i u_j) = -\frac{\partial p}{\partial x_i} + \frac{\partial}{\partial x_j}\left[\mu\left(\frac{\partial u_i}{\partial x_j} + \frac{\partial u_j}{\partial x_i} - \frac{2}{3}\delta_{ij}\frac{\partial u_l}{\partial x_l}\right)\right] + \frac{\partial}{\partial x_j}\left(-\rho\overline{u_i' u_j'}\right) \tag{2}$$

where, the term $-\rho\overline{u_i' u_j'}$ needs to be numerically modeled to close the equation.

The current study incorporates various turbulence models for studying jet impingement flow characteristics with emphasis on the effects of this kind of flow on nearby structures. All the simulations were carried out under incompressibility assumptions. Below is a brief discussion of some of the models, which were used in this research.

4.1 Standard k–ε Model

This is still the most frequently used model in general-purpose CFD codes. The model proposed by Launder and Spalding (1972) is used here. The standard model uses the following transport equations for turbulent kinetic energy (k) and its rate of dissipation (ε):

$$\frac{\partial}{\partial t}(\rho k) + \frac{\partial}{\partial x_i}(\rho k u_i) = \frac{\partial}{\partial x_j}\left[\left(\mu + \frac{\mu_t}{\sigma_k}\right)\frac{\partial k}{\partial x_j}\right] + G_k + G_b - \rho\varepsilon - Y_M + S_k \tag{3}$$

and

$$\frac{\partial}{\partial t}(\rho\varepsilon)+\frac{\partial}{\partial x_i}(\rho\varepsilon u_i)=\frac{\partial}{\partial x_j}\left[\left(\mu+\frac{\mu_t}{\sigma_\varepsilon}\right)\frac{\partial\varepsilon}{\partial x_j}\right]+C_{1\varepsilon}\frac{\varepsilon}{k}(G_k+C_{3\varepsilon}G_b)-C_{2\varepsilon}\rho\frac{\varepsilon^2}{k}+S_\varepsilon \quad (4)$$

The above equations contain 5 adjustable constants $C_{1\varepsilon}$, $C_{2\varepsilon}$, C_μ, σ_k and σ_ε which have default values:

$C_{1\varepsilon} = 1.44$ and $C_{2\varepsilon} = 1.92$, $C_\mu = 0.09$; $\sigma_k = 1.00$ and $\sigma_\varepsilon = 1.30$.

4.2 RNG k–ε Model

The RNG k-ε model (renormalization group theory) which is an extension of the standard k–ε model, is also used here as one of the turbulence models. The RNG model differs from the standard k–ε model by inclusion of an extra term R in the right hand side of the ε equation. The extra term R depends on the rate of strain, as given by:

$$R=\frac{\rho C_\mu \eta^3\left(1-\eta/\eta_0\right)}{\left(1+\beta\eta^3\right)}\left(\frac{\varepsilon^2}{k}\right) \quad (5)$$

where $\eta = Sk/\varepsilon$. The model constants for RNG k–ε model (FLUENT, 2003) are given by:

$C_{1\varepsilon} = 1.42$, $C_{2\varepsilon} = 1.68$, $C_\mu = 0.0845$, $\sigma_k = 1.0$, $\sigma_\varepsilon = 1.3$, $\eta_0 = 4.38$ and $\beta = 0.012$.

4.3 Realizable k-ε Model

Here the transport equations are given by

$$\frac{\partial}{\partial t}(\rho k)+\frac{\partial}{\partial x_i}(\rho k u_j)=\frac{\partial}{\partial x_i}\left[\left(\mu+\frac{\mu_t}{\sigma_k}\right)\frac{\partial k}{\partial x_j}\right]+G_k+G_b-\rho\varepsilon-Y_M+S_k \quad (6)$$

and

$$\frac{\partial}{\partial t}(\rho\varepsilon)+\frac{\partial}{\partial x_j}(\rho\varepsilon u_j)=\frac{\partial}{\partial x_j}\left[\left(\mu+\frac{\mu_t}{\sigma_\varepsilon}\right)\frac{\partial\varepsilon}{\partial x_j}\right]+\rho C_1 S_\varepsilon-\rho C_2\frac{\varepsilon^2}{k+\sqrt{\nu\varepsilon}}+C_{1\varepsilon}\frac{\varepsilon}{k}C_{3\varepsilon}G_b+S_\varepsilon \quad (7)$$

where $C_1 = \max\left[0.43, \frac{\eta}{\eta+5}\right]$, and $\eta = S\frac{k}{\varepsilon}$

The model constants for the realizable k–ε model are given by:

$C_{1\varepsilon} = 1.44$, $C_2 = 1.68$, $\sigma_k = 1.0$ and $\sigma_\varepsilon = 1.2$. C_μ is no longer a constant in this model. More details about this model can be found in Shih et al (1993).

4.4 Shear-Stress Transport (SST) k-ω Model

This is a variation of the standard k-ω model proposed by Wilcox (1999). In this model, in addition to the standard k equation, another equation for length (ω) is solved. This quantity (ω) is often called specific dissipation and it is defined as $\omega \propto \varepsilon/k$. The modeled k and ω equations are given by (FLUENT, 2003):

$$\frac{\partial}{\partial t}(\rho k) + \frac{\partial}{\partial x_i}(\rho k u_i) = \frac{\partial}{\partial x_j}\left[\Gamma_k \frac{\partial k}{\partial x_j}\right] + G_k - Y_k + S_k \tag{8}$$

and

$$\frac{\partial}{\partial t}(\rho \omega) + \frac{\partial}{\partial x_i}(\rho \omega u_i) = \frac{\partial}{\partial x_j}\left[\Gamma_\omega \frac{\partial \omega}{\partial x_j}\right] + G_\omega - Y_\omega + D_\omega + S_\omega \tag{9}$$

In the SST k-ω model, the definition of turbulent viscosity is modified to account for the transport of the principal turbulent shear stress and this feature enables this model to perform better than the standard k-ε and standard k-ω model. There is also a cross-diffusion term D_ω added to the ω equation.

4.5 Reynolds Stress Model (RSM)

The transport equations for transport of Reynolds stresses, $\rho\overline{u_i' u_j'}$ are written as follows:

$$\frac{\partial}{\partial t}\left(\rho\overline{u_i'u_j'}\right)+\frac{\partial}{\partial x_k}\left(\rho u_k\overline{u_i'u_j'}\right)=-\frac{\partial}{\partial x_k}\left[\rho\overline{u_i'u_j'u_k'}+\overline{\rho\left(\delta_{kj}u_i'+\delta_{ik}u_j'\right)}\right]+\frac{\partial}{\partial x_k}\left[\mu\frac{\partial}{\partial x_k}\left(\overline{u_i'u_j'}\right)\right]$$

$$-\rho\left(\overline{u_i'u_k'}\frac{\partial u_j}{\partial x_k}+\overline{u_j'u_k'}\frac{\partial u_i}{\partial x_k}\right)-\rho\beta\left(g_i\overline{u_j'\theta}+g_j\overline{u_i'\theta}\right)+\overline{p\left(\frac{\partial u_i'}{\partial x_j}+\frac{\partial u_j'}{\partial x_i}\right)}-2\mu\overline{\frac{\partial u_i'}{\partial x_k}\frac{\partial u_j'}{\partial x_k}} \tag{10}$$

$$-2\rho\Omega_k\left(\overline{u_j'u_m'}\varepsilon_{ikm}+\overline{u_i'u_m'}\varepsilon_{jkm}\right)+S_{user}$$

More details about this model and definition of the individual terms can be found in (FLUENT, 2003, Gibson and Launder, 1978 and Launder et al, 1975).

4.6 Large Eddy Simulation (LES)

In LES the governing equation are derived by filtering the time dependent Navier-Stokes equations. The eddies whose scales are smaller than the filter width or grid spacing are filtered out. The subgrid-scale stresses resulting from the previous filtering operation requires modeling. The Boussinesq hypothesis (FLUENT, 2003) is employed and the subgrid-scale turbulent stresses are computed from

$$\tau_{ij}-\frac{1}{3}\tau_{kk}\delta_{ij}=-2\mu_t\overline{S}_{ij} \tag{11}$$

Where μ_t is the subgrid –scale turbulent viscosity, and $\overline{S}_{ij}$ is the rate-of-strain tensor for the resolved scale defined by

$$\overline{S}_{ij}\equiv\frac{1}{2}\left(\frac{\partial\overline{u}_i}{\partial x_j}+\frac{\partial\overline{u}_j}{\partial x_i}\right) \tag{12}$$

For the calculation of μ_t, the dynamic Smagorinsky-Lilly model (FLUENT, 2003) was used. The eddy viscosity μ_t is modeled as

$$\mu_t=\rho L_s^2\left|\overline{S}\right| \tag{13}$$

Where L_s is the mixing length for subgrid scales and

$$\left|\overline{S}\right| \equiv \sqrt{2\overline{S}_{ij}\,\overline{S}_{ij}} \tag{14}$$

L_s is calculated using

$$L_s = \min\left(\kappa d, C_s V^{1/3}\right) \tag{15}$$

where κ is the von Karman constant, d is the distance to the closest wall, C_s is the Smagorinsky constant, and V is the volume of the computational cell. C_s is computed dynamically based on the information provided by the resolved scales of motion and varies in time and space over a wide range.

4.7 Solution Parameters

For all the numerical simulations, the density and viscosity of air were taken as 1.225 kg/m^3 and 1.7894 E-05 Ns/m^2, respectively. The inlet values of turbulence intensities were substituted from the experimental data. For all the simulations using RANS models, the QUICK scheme was used for the convective fluxes as this reduces the numerical diffusion, and a 2nd order scheme was used for k and ε terms. For LES, a central difference scheme was used. The SIMPLE algorithm was used for the pressure correction for steady-state simulations, whereas for LES the PISO algorithm was used.

Initially, the numerical simulation was carried out using various two-dimensional domain dimensions (r, H, H_N), as listed in Table 1, using the k-ε model. Axisymmetric boundary condition (b.c.) was used along the centerline of the jet. It was observed that the difference in the radial velocities did not vary by more than 2.8 % for these cases (C1 to C6). The axial velocity profiles under the jet for all these simulations were also in close agreement with

each other. Ultimately, it was decided to adopt case C2 for our analysis, based on considerations of optimum domain size as well as computation time.

5. Results and Discussion

The ground pressure coefficients are shown in Figure 3, where $C_p = (P-P_s)/0.5\rho V_j^2$. The ground pressures corresponding to the four jet heights (H1, H2, H3 and H4) and two velocities (V1 and V2) match exactly showing that there is no effect of the jet height and jet velocity on ground pressures for the range of parameters chosen. It can be seen that the numerical values of pressure coefficients calculated using the different turbulence models match very well with that obtained from the experiments (Figure 3b). The uncertainty in the experimental pressure values was estimated as less than 10%.

Flow visualization using PIV is shown in Figure 4 where it can be observed that jet axial velocity is uniform across the width of the nozzle near its exit and at mid-height from the ground plane but starts to show the effects of the ground plane as the jet nears the impingement surface. The jet is observed to expand slightly as it descends.

The axial velocity profiles along the centerline of the jet at various heights from the ground plane are shown in Figure 5. The comparison in Figure 5a clearly shows that the jet expands along its edges as it descends and the velocity at the center of the jet decreases by almost 30% as it approaches the ground plane. It also shows the consistency of the profiles between two different velocities V1 and V2 of the jet (Figure 5a). There is a very good agreement between the experimental measurements and numerical (RSM) data as seen in Figure 5b. Axial velocity profiles from other numerical methods also match very well with the experimental ones but are not shown here. The PIV and hot-wire measurements differ

near the edges of the jet. The PIV profiles consistently show a narrower jet at different heights. This could be due to reduced concentration of seeding particles along the jet boundary; a common problem in the use of PIV to visualize jet flows.

A comparison of the normalized axial velocities along the centerline of the jet obtained with PIV and all the numerical models shows (Figure 6) a close agreement between the experimental and all the numerical models. This plot also shows how the jet velocity along the centerline decreases as the jet approaches the ground. The comparison of normalized radial velocity profiles at r/D of 0.5, 1, 2 and 3 that were obtained with k-ε model for different boundary conditions, Cases C1-C6 as described in Table 1, is shown in Figure 7. It shows a good agreement proving that these boundary conditions have little influence on the flow profiles.

The normalized profiles of horizontal velocity (U) at different r/D values are plotted in Figure 8 and compared with the empirical profiles of Rajarathnam (1976) and Wood et al (2001). The general form of the empirical profile is given by

$$\frac{U}{U_m} = C_1\left(\frac{z}{b}\right)^n\left[1 - erf\left(C_2\frac{z}{b}\right)\right] \tag{16}$$

where $C_1 = 1.48$, $C_2 = 0.68$ and $n = 1/7$ (Rajaratnam, 1976); $C_1 = 1.55$, $C_2 = 0.70$ and $n = 1/6$ (Wood et al, 2001); U_m = maximum horizontal velocity at a specific r/D; b = elevation from the ground at which $U = U_m/2$ and erf ( ) is error function.

The current experimental data from PIV and pressure rake at several r/D locations (Figure 2b) were used to generate Eqs. 16-18. The uncertainty in the velocity measurements depends on the flow region but generally it was estimated to be within ±10%.

The best curve-fit of this data (for r/D = 0.75, 1, 1.25, 1.5, 2.0, 2.5 and 3.0) is obtained with $C_1 = 1.52$, $C_2 = 0.68$ and n = 1/6.5 in Eq. 16. This empirical profile is plotted in Figure 8a and was found to agree very well with those of Rajaratnam (1976) and Wood et al (2001). Also plotted in the same figure are the experimental results of Cooper et al (1993). The range of r/D for which the proposed empirical profiles are valid is $0.75 \leq r/D \leq 3.00$. In the figure, the normalized experimental data for r/D = 1, 2 and 3 only are shown for sake of clarity.

The field observation data from Project NIMROD (Fujita, 1981) is also shown in the same plot. The observed values agree closely at higher elevations up to z/b of 1 compared to those at lower ones ($z/b < 0.2$). This could be due to the fact that NIMROD Doppler radar data is prone to errors at lower elevations because of obstructions near ground level. The mismatch between Doppler data and current experimental data at elevations corresponding to $z/b > 1$ could be attributed to higher scatter in the experimental data due to measurement errors of relatively smaller radial velocities ($U/Um < 0.45$) at these elevations as well different topographical conditions too.

The numerical results for normalized radial velocity profiles of the jet are compared with the empirical profile (Eqn. 16) obtained from experimental data and found to agree well, as shown in Figure 8b.

The normalized curve for U_m that fits the experimental data (PIV and rake), as plotted in Figure 9a, is given by

$$\frac{U_m}{V_j} = \exp\left[1.905 - \frac{1.858}{\frac{r}{D}} - 1.949\ln\left(\frac{r}{D}\right)\right] \tag{17}$$

The maximum radial velocity (U_m) is almost equal in magnitude to the jet velocity (V_j) up to r/D of 1 and then decreases to $0.425V_j$ at r/D of 3.

The curve for the prediction of boundary-layer development of the jet that fits the experimental data, as shown in Figure 10a, is given by

$$\frac{b}{D} = -0.0362 + 0.0818\frac{r}{D} + 1.0062\exp\left[-2.472\left(\frac{r}{D}\right)\right] \tag{18}$$

The numerical results for normalized curve for U_m and the boundary layer development of the jet do not match that well with the experimental data as shown in Figs. 9b and 10b. From an assessment of various numerical turbulence models, it is seen that the realizable k-ε model gives results that are closest to the experimental values for the entire range of r/D, whereas RSM model gives acceptable results up to r/D of 2. The standard k-ε, RNG k-ε and SST k-ω models produce results that deviates the most from the experimental values.

For understanding the effect of nozzle diameter on the radial velocities, the experimental data of Cooper et al (1993) and Tsuei (1962) was compared with the empirical profiles for U_m and b obtained for D = 203 mm (8 in.) nozzle (Figure 11). There is generally a very good agreement between the proposed profiles and those of Cooper et al (1993) and Tsuei (1962) data. It is therefore concluded based on this limited comparison that the normalized profiles are not a function of jet diameter. This has a positive implication on the geometric scaling-up of the experimental results to the field.

Table 2 shows the values of U_m/V_j and b/r corresponding to different jet heights, jet exit velocities and location x from the jet centerline. It can be seen that these values correspond fairly well with the values given in Blevins (1984) for impinging radial jet (H/D > 1) with r/D ≥ 1 but not so well for r/D < 1 as originally specified in Blevins (1984).

For understanding the second order statistics, a comparison of the radial turbulence intensity profiles was made. Figure 12 shows the results of the comparison of the data obtained using PIV and LES. It is seen that there is reasonable agreement at most locations except at r/D = 0.75 and 1.0, which is the transition region.

Figure 13 shows the comparison of building pressure coefficients (normalized with V_j), both from experiments and from numerical simulations. All the RANS numerical models tend to predict the pressures on the front and back of the cube well, but fail to do the same on the roof, which is an inherent drawback of most RANS models. But LES gives a much better result compared to other turbulence models, as it can capture the flow separation on the roof.

6. Summary and Conclusions

A laboratory study of a stationary microburst using an impinging jet was conducted to systematically evaluate the effect of different parameters on the velocity profiles and pressure distribution on the ground. Numerical Simulations were carried out with uniform jet profiles and proper boundary conditions and extent of the numerical domain were identified. Different turbulence models were applied to determine their applicability to this type of flow. Comparison of numerical and experimental results was made. The empirical equations derived here from the experimental data have potential application in the design of civil engineering structures for winds generated by a microburst.

The jet expands and the velocity along the centerline of the jet decreases as it gets closer to the ground. There is a good agreement between axial velocity profiles of the jet obtained from experiments (hot wire) with those obtained with various numerical turbulence models. PIV was unable to capture the entire width of the jet because of possible lack of seeding

particles along the jet boundary that can be possibly corrected in the future if the ambient air surrounding the jet is also seeded.

The horizontal velocity profiles from experiments agree well with the empirical profiles of Rajaratnam (1976) and Wood et al (2001), and a new empirical profile equation is proposed. The normalized horizontal velocity profiles computed numerically with various models match closely with the experimental results for different r/D values. New empirical equations are proposed for predicting the boundary layer growth and the maximum radial velocity as a function of distance from the center of the jet. The validity of these equations was checked with the experimental data of other researchers and was found to agree well. All the numerical models capture the trend of the boundary layer growth and decay of maximum radial velocities with increasing radial distance, but the predicted values from LES, realizable k-ε and RSM models match the experimental data better than the other three models. Both ground pressure coefficients and axial velocity profiles under the jet computed numerically with different turbulence models agree very well with experimental results. Pressures on the cube computed numerically agree well compared to experimental data for the front and back sides of the cube. On the roof, LES is able to capture flow separation better, resulting in improved prediction of roof pressures compared to under prediction of pressure on the roof with other turbulence models.

References

Alahyari, A., and Longmire, E.K., (1995) Dynamics of Experimentally Simulated Microbursts. AIAAJ, 33, (11) 2128- 2136.

Behnia, M., Parneix, S., and Durbin, P.A., (1998) Prediction of heat transfer in a axisymmetric turbulent jet impinging on a flat plate. International Journal of Heat Mass Transfer. 41(12), 1845-1855.

Blevins, R.D. (1984) Applied Fluid Dynamics Handbook. Van Nostrand Reinhold Co, New York.

Chay, M.T., and Letchford, C.W. (2001) Pressure Measurements on a Building Model in a Simulated Downburst Flow. Proceedings of 1st Americas Conference on Wind Engineering, 4-6 June, Clemson, SC.

Cooper, D., Jackson, D.C., Launder, B.E., and Liao, G.X. (1993) Impinging Jet Studies for Turbulence Model Assessment-I. Flow-Field Experiments. International Journal of Heat Mass Transfer. 36(10), 2675-2684.

Craft, T. J., Graham, L.J.W., and Launder, B.E. (1993) Impinging Jet Studies for Turbulence Model Assessment-II: An Examination of the Performance of Four Turbulence Models. International Journal of Heat Mass Transfer, 36(10), pp. 2685-2697.

Craft, T.J., Launder, B.E., and Suga, K. (1997) Prediction of Turbulent Transition Phenomenon with a Nonlinear Eddy-Viscosity Model. International Journal of Heat Fluid Flow. 18, 15-28.

Dianat, M., Fairweather, M., and Jones, W.P. (1996) Reynolds Stress Closure Applied to Axisymetric Impinging Turbulent Jets. Theoretical and Computational Fluid Dynamics. 8, 435-447.

Didden, N., and Ho, C.M. (1985) Unsteady separation in a boundary layer produced by an impinging jet. Journal of Fluid Mechanics.`160, 235-256.

Donaldson, C.D., and Snedeker, R.S. (1971) A study of free jet impingement. Part1. Mean properties of free and impinging jets. Journal of Fluid Mechanics. 45(2), 235-256

Fluent (2003) FLUENT User's Guide, Release 6.1, Fluent, Inc., Lebanon, New Hampshire.

Fujita, T.T. (1981) Tornadoes and Downbursts in the Context of Generalized Planetary Scales. Journal of Atmospheric Science, 38, 1511-1534.

Fujita, T.T. (1985) The Downburst: Microburst and Macroburst. University of Chicago Press.

Gibson, M.M., and Launder, B.E. (1978) Ground Effects on Pressure Fluctuations in the Atmospheric Boundary Layer. Journal of Fluid Mechanics, 86, pp. 491-511.

Holmes, J.D. and Oliver, S.E. (2000) An Empirical Model of a Downburst. Engineering Structures. 22, 1167-1172.

Knowles, K., and Myszko, M. (1998) Turbulence measurement in radial wall-jets. Experimental Thermal and Fluid Sciences. 17, 71-78.

Launder, B.E., and Spalding, D.B. (1972) Lectures in Mathematical Models of Turbulence. Academic Press. London, England.

Launder, B. E., Reece, G. J., and Rodi, W. (1975) Progress in the Development of a Reynolds-Stress Turbulence Closure. J. Fluid Mechanics. 68 (3), 537-566.

Letchford, C. W., and Illidge, G. (1999) Turbulence and Topographic effects in Simulated Thunderstorm Downdrafts by Wind Tunnel Jet, in: Wind Engineering into the 21st Century, Proceedings of the Tenth International Conference on Wind Engineering, eds. A. Larsen G. L. Larose and F. M. Livesey, Denmark, June 1999, 1907-1912.

Lundgren, T.S., Yao, J., and Mansour, N.N. (1992)Microburst Modeling and Scaling. Journal of Fluid Mechanics. 239, 461-488.

Myszko, M., and Knowles, K. (1995) Numerical Modeling of a Single Impinging Jet and Experimental Validation, in: PHOENICS Users Conference, Trento, Italy 8th-10th November

Rajarathnam, N. (1976) Turbulent Jets. Elsevier Scientific Publishing Company

Selvam, R.P., and Holmes, J.D. (1992) Numerical Simulation of Thunderstorm Downdrafts. J. Wind Eng. Ind. Aerodyn. 41-44, 2817-2825.

Shih, T.H., Liou, W.W., Shabbir, A., Yang, Z., and Zhu, J. (1995) A New k-ε Eddy-Viscosity Model for High Reynolds Number Turbulent Flows: Model Development and Validation. Computers Fluids. 24(3), 227-238.

Thom, H.C.S. (1969) New distributions of extreme wind speeds in the United States. Journal of Structures Division. ASCE. 94, 1787-1801.

Tsuei, Y.G. (1962) Axisymmetric Boundary Layer of a Jet Impinging on a Smooth Plate. Ph.D Dissertation, Colorado State University, Fort Collins, Colorado.

Vickery, P.J. and Twisdale, L.A. (1995) Analysis of thunderstorm occurrences and wind speed statistics. J. Wind Eng. Ind. Aerodyn. 55, 813-821.

Wilcox, D.C. (1998) Turbulence Modeling for CFD. DCW Industries, Inc, La Canada, California.

Wood, G.S., and Kwok, K.C.S. (1999) Physical and Numerical Modeling of Thunderstorm Downbursts. Wind Engineering into the 21st Century, Proceedings of the Tenth International Conference on Wind Engineering, eds. A. Larsen G. L. Larose and F. M. Livesey, Denmark, June 1999, 1919-1924.

Wood, G.S., Kwok, C.S., Motteram, N.A., and Fletcher, D.F. (2001) Physical and Numerical Modelling of Thunderstorm Downbursts. J. Wind Eng. Ind. Aerodyn. 89, 535-552.

Yao, J. and Lundgren, T.S. (1996) Experimental Investigation of Microbursts. Experiments in Fluids. 21, 17-25.

Yamamoto, M. (1997) Application of multiple-time-scale Reynolds stress models to wall jets. 2nd Int. Sym. on Turbulence, Heat and Mass Transfer, eds. Hanjalic, K., and Peters, T. W. J., Delft University Press

Table 1: Shapes and Sizes of Domains Tested

Case C1	Cases C2 and C3	Case C4 and C5	Cases C6
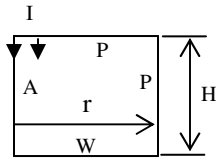	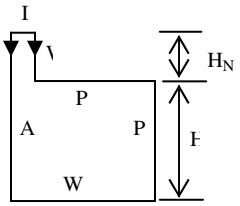	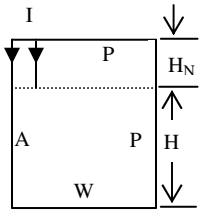	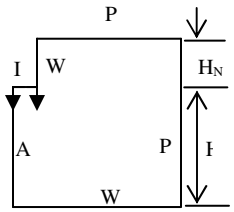
H = 2D	H = 2D	H = 2D, H_N = D	H = 2D, H_N =D
C1 r = 5D	C2 (a) r = 5D (b) H_N =D	C3 (a) r = 5D (b) H_N =D/4	C4 (a) r = 5D C5 (b) r =10D	C6 r =5D

P = pressure b.c., W = wall b.c., A = axisymmetry b.c., I = inlet b.c. (uniform jet), D = jet diameter,
(b) H = jet height, r = radial distance from jet centerline, H_N = height of jet nozzle.

Table 2: Comparison of Current experimental data with Blevins (1984)

H (m) r/H ≥ 0.25	V_j (m/s)	r	U_m/V_j Eq. 17	U_m/V_j Blevins(1984)* r > 0.22D	b/r Eq. 18	b/r Blevins(1984)* r > 0.22D
H1 to H3	V1 and V2	0.75D	0.99	1.40	0.244	0.087
H1 to H3	V1 and V2	1D	1.05	1.05	0.131	0.087
H1 to H3	V1 and V2	2D	0.69	0.53	0.068	0.087
H1 to H3	V1 and V2	3D	0.43	0.35	0.070	0.087

* Uncertainty in these values is 20-30 %

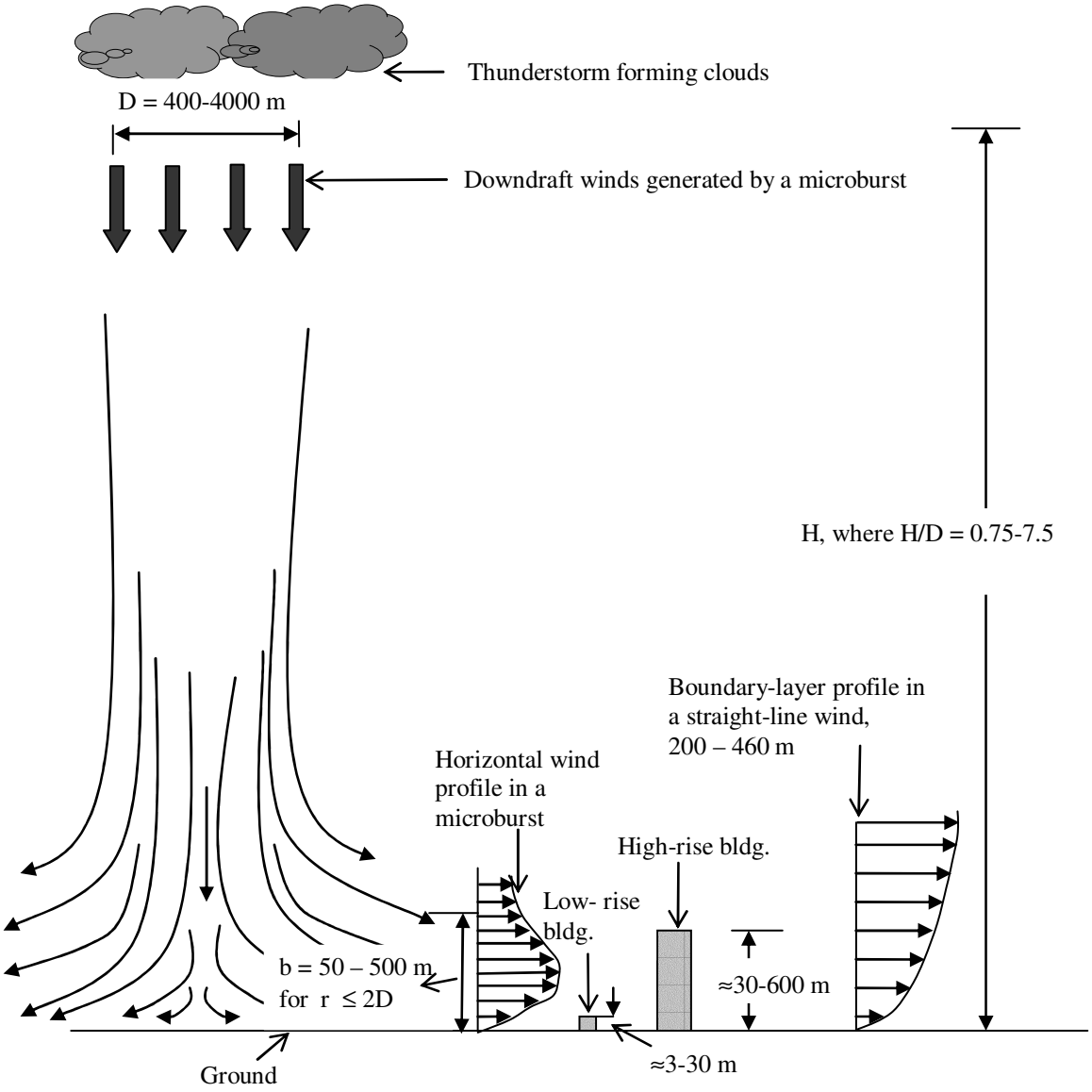

Figure 1: Typical dimensions of horizontal wind profile in a typical microburst in comparison to straight-line wind profile and building heights

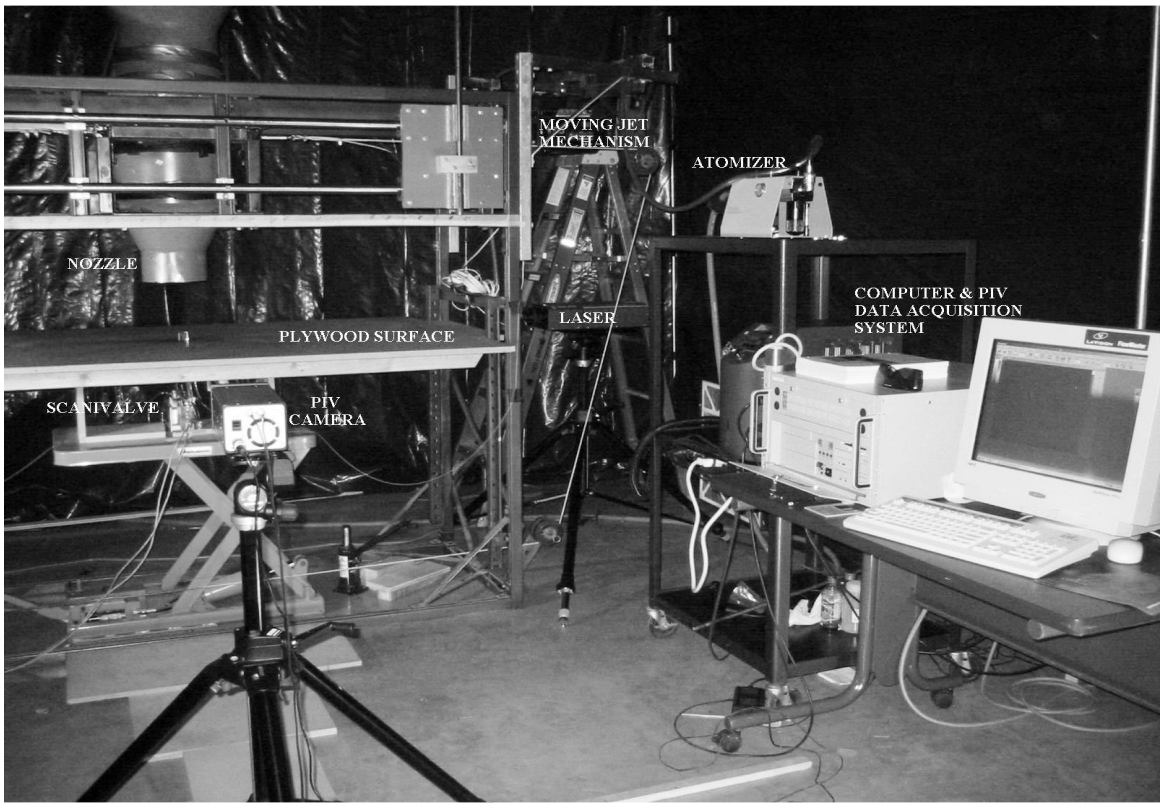

(a)

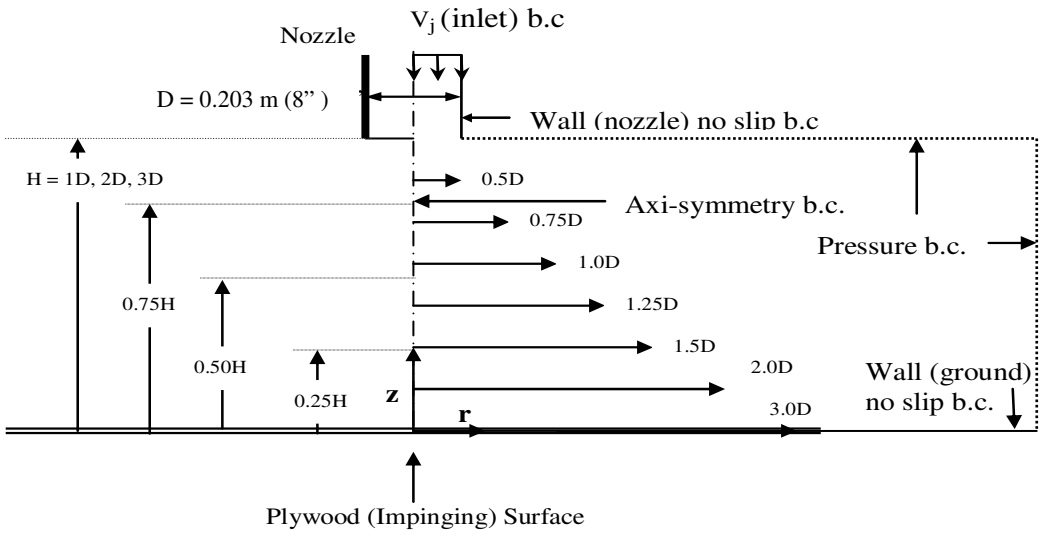

(b)

Figure 2: (a) Experimental setup for PIV and ground pressure measurement.
(b) Schematic of jet impingement setup and velocity measurement locations
(The boundary conditions used for 2-D numerical simulation are shown)

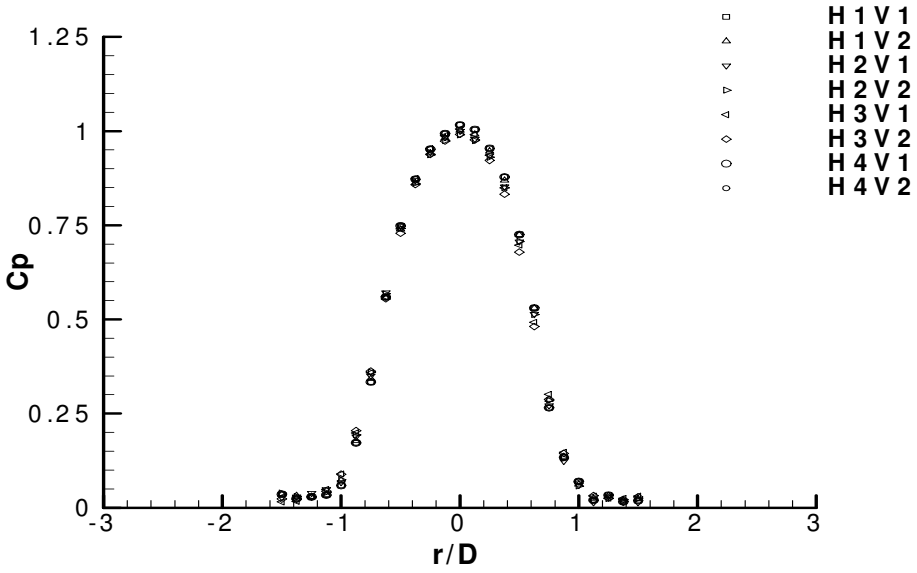

(a)

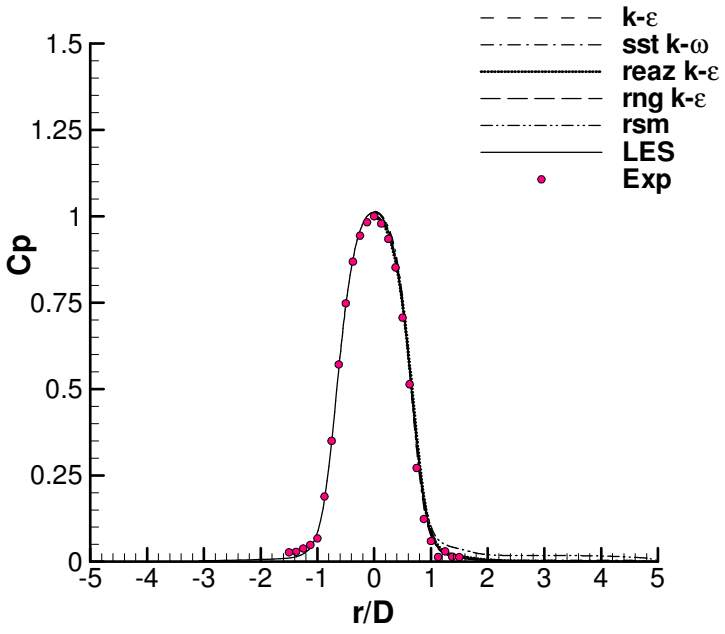

(b)

Figure 3: (a) Plot of pressure coefficient on impingement ground plane (experimental)
(b) Comparison of experimental and numerical simulation of ground Cp for H2V1

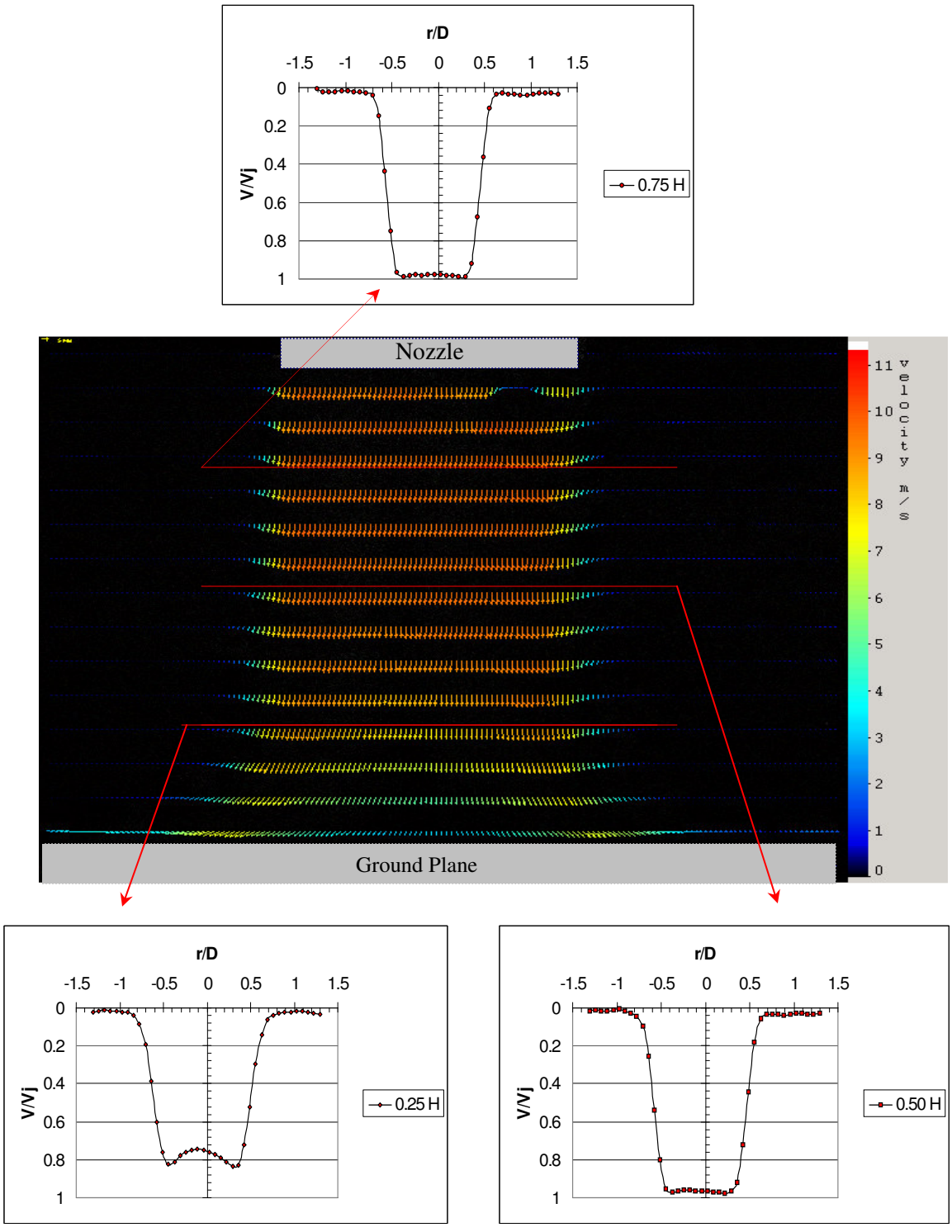

Figure 4: Jet impingement visualization from PIV

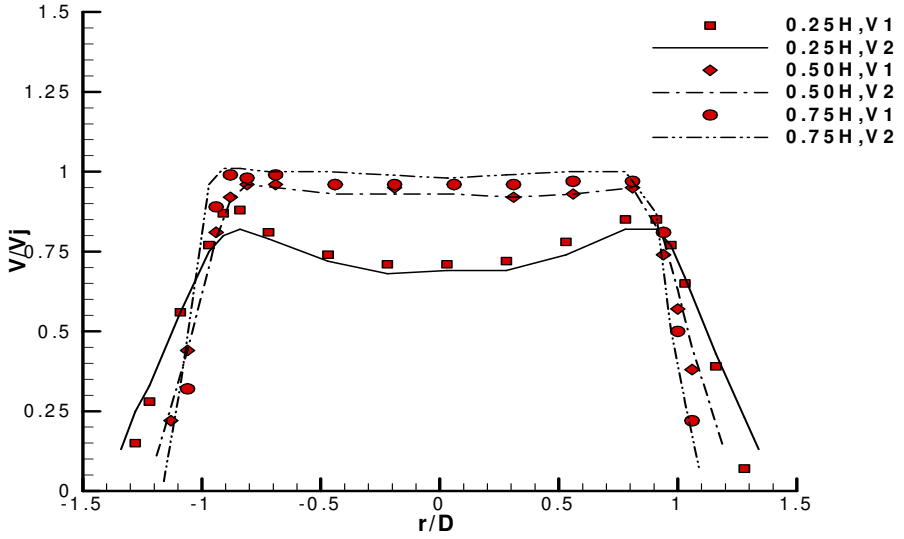

(a)

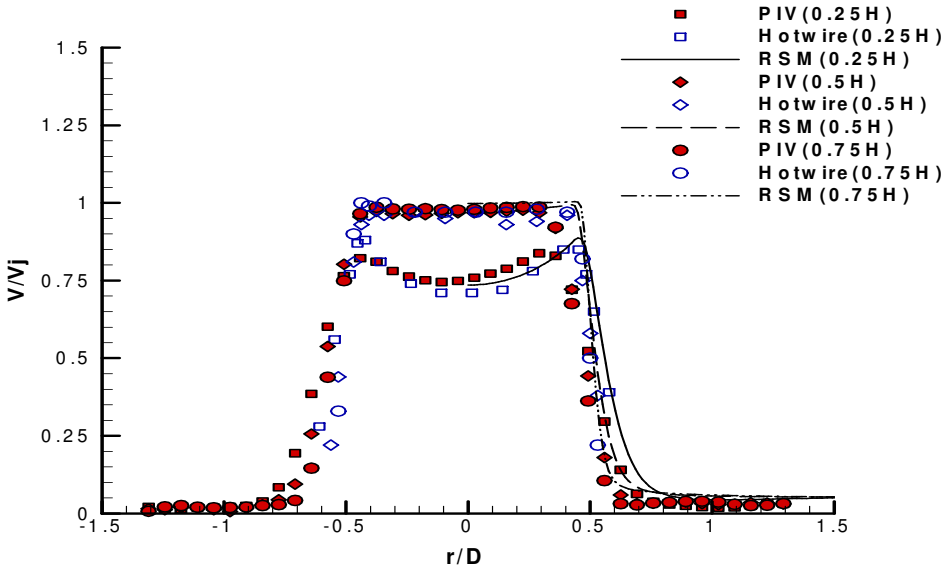

(b)

Figure 5: a) Comparison of normalized jet velocities (hot-wire data) at different normalized heights
b) Comparison of experimental (PIV, hot wire) and numerical (rsm) normalized vertical velocity profiles at H = 2D & V= V1

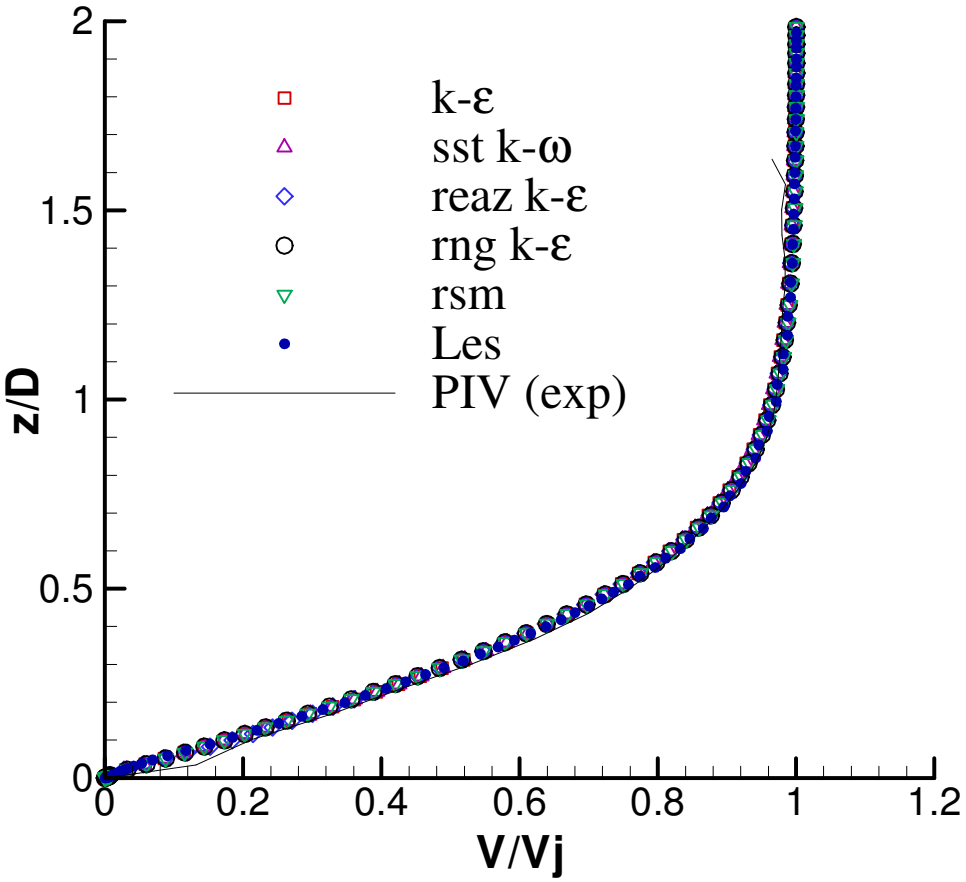

Figure 6: Comparison of normalized vertical velocities along the centerline of the jet (experimental and numerical)

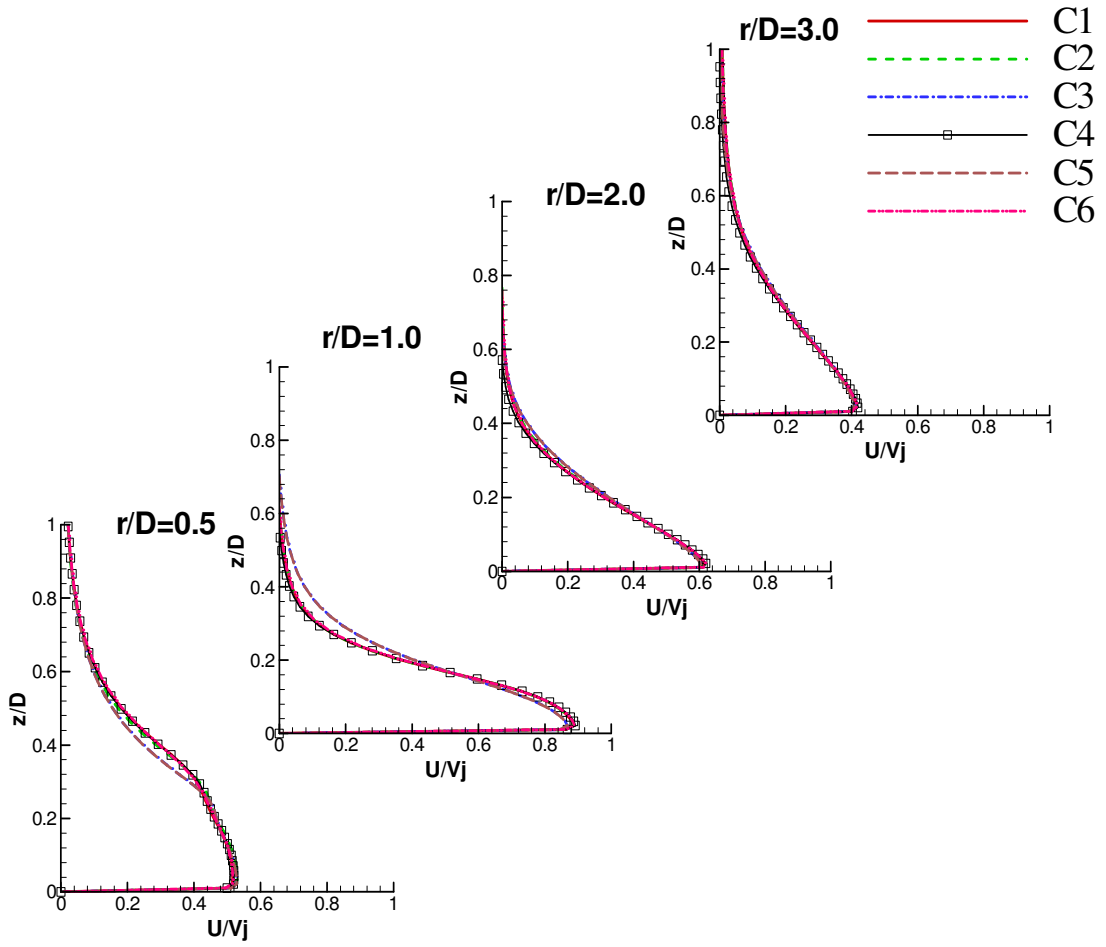

Figure 7: Comparison of radial velocities with different numerical boundary conditions

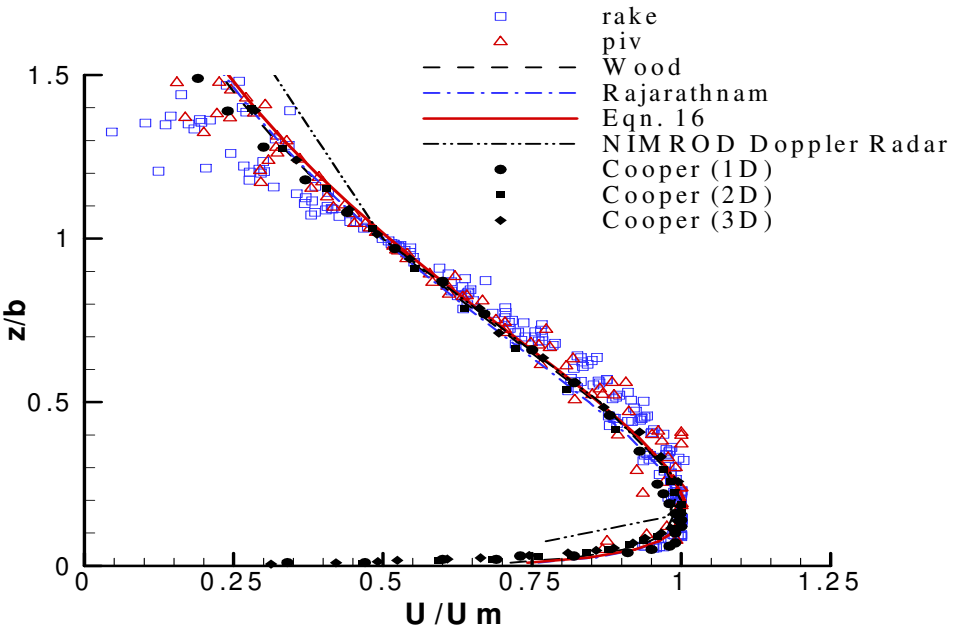

(a)

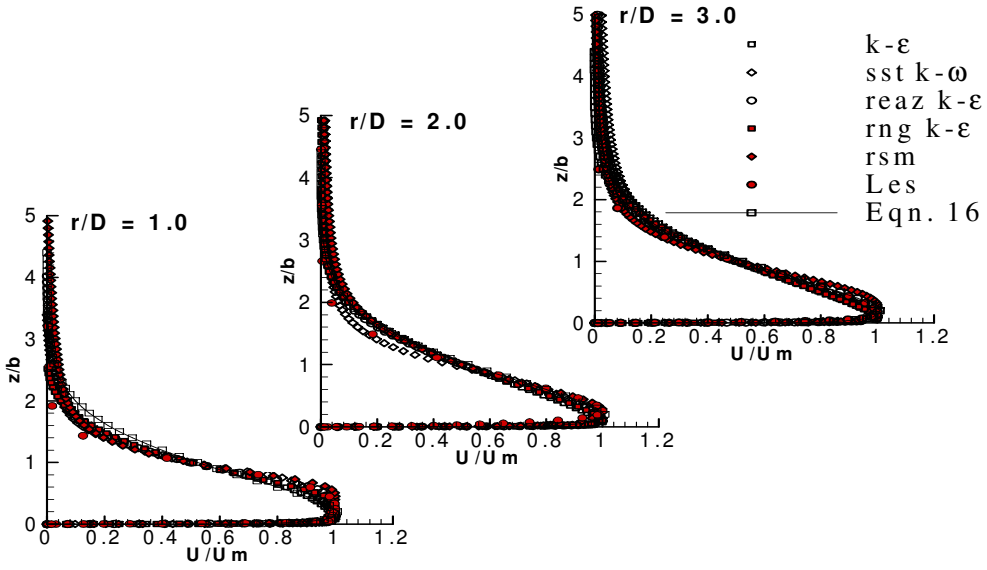

(b)

Figure 8: (a) Comparison of normalized radial velocity profiles (experimental with pressure rake, NIMROD field data and empirical profiles as given by Equation 16
(b) Comparison of numerical simulation data for H2 and V1 with present empirical profile as given by Equation 16

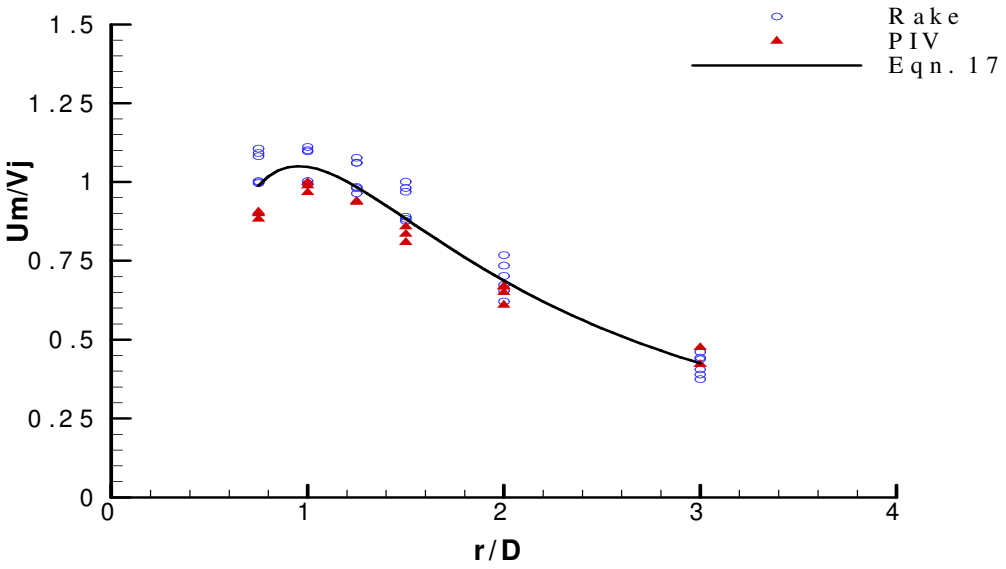

(a)

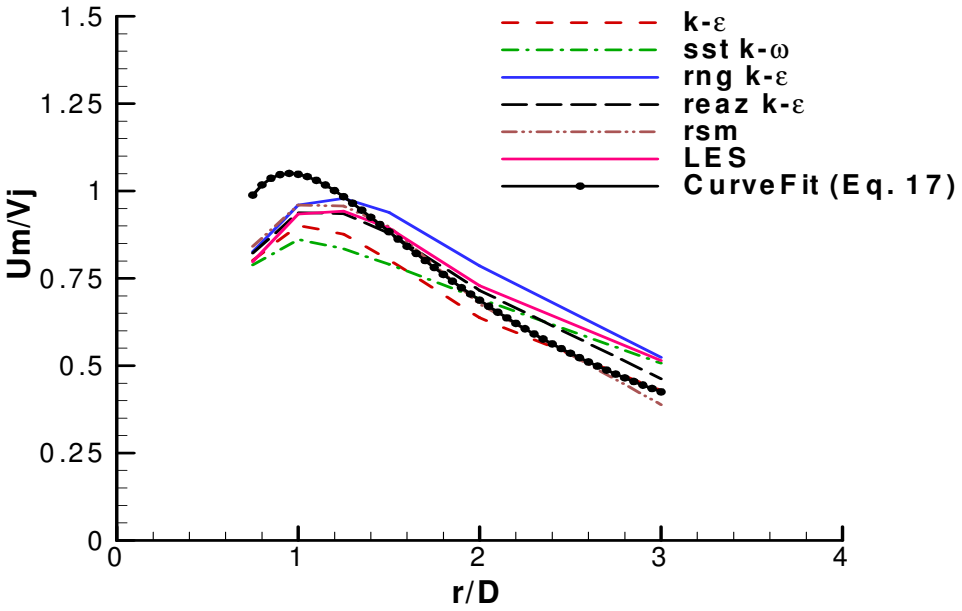

(b)

Figure 9: (a) Plot of Um/Vj as a function of r/D, (b) Comparison of numerical simulation data for H2 and V1 with present empirical profile as given by Equation 17

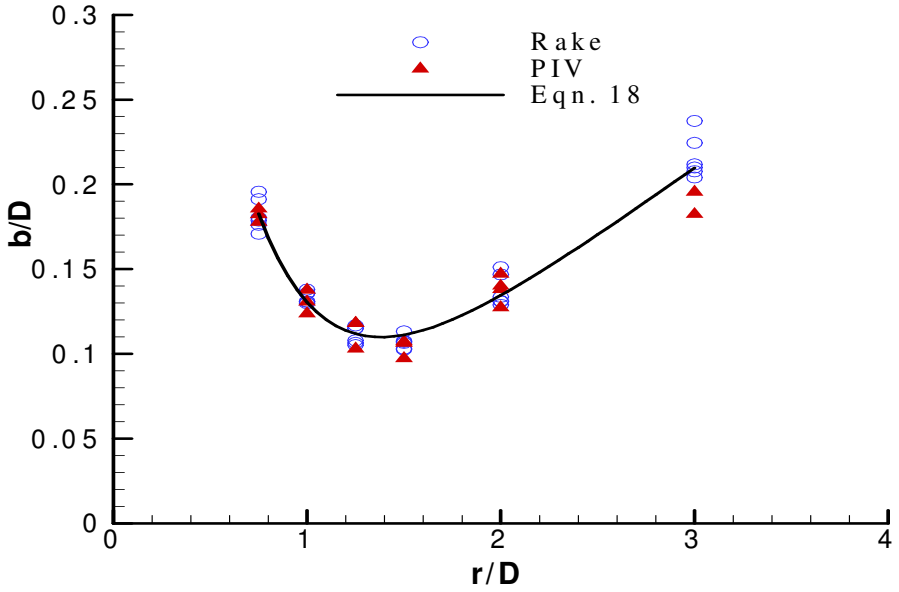

(a)

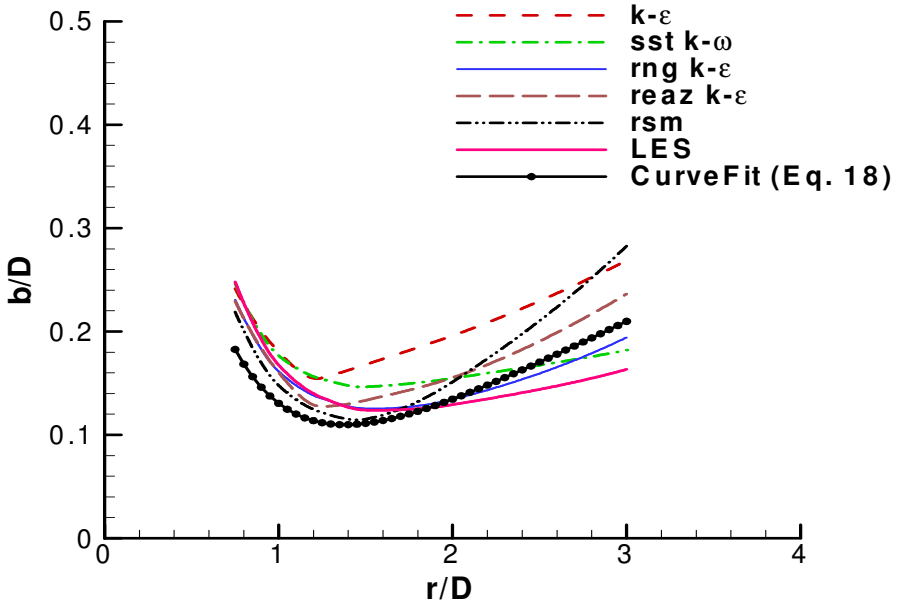

(b)

Figure 10: (a) Plot of boundary-layer growth, (b) Comparison of numerical simulation data for H2 and V1 with present empirical profile as given by Equation 18

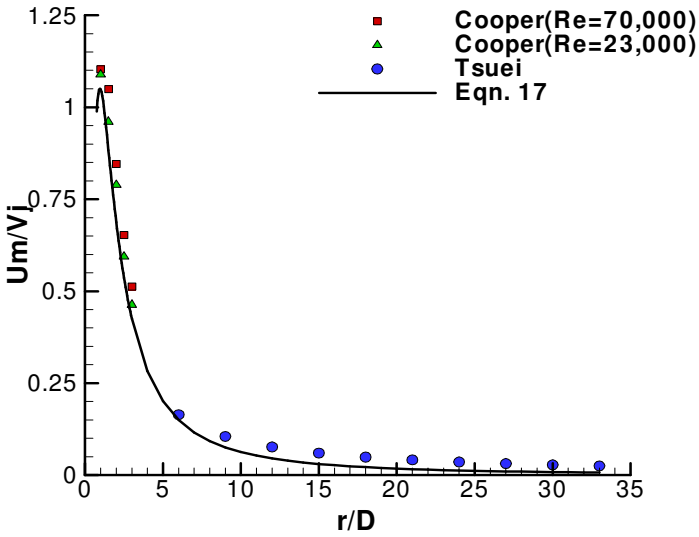

(a)

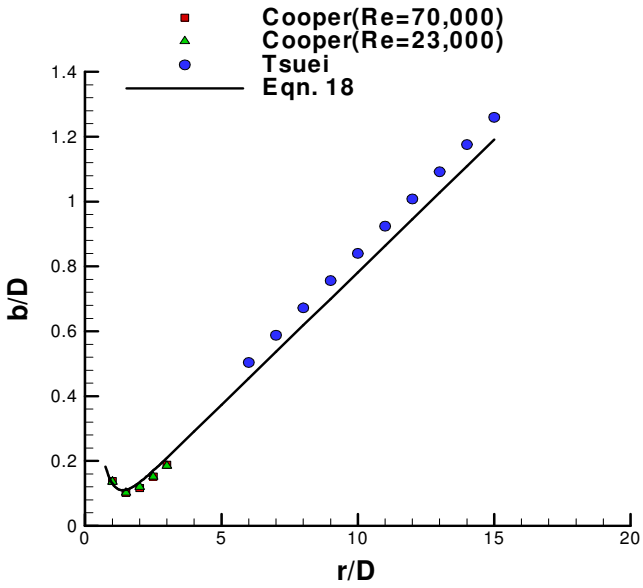

(b)

Figure 11: Comparison of data obtained by Cooper et al (1993) and Tsuei (1962) with empirical profiles for D = 203 mm (8") a) Um/Vj vs r/D and b) b/D vs r/D

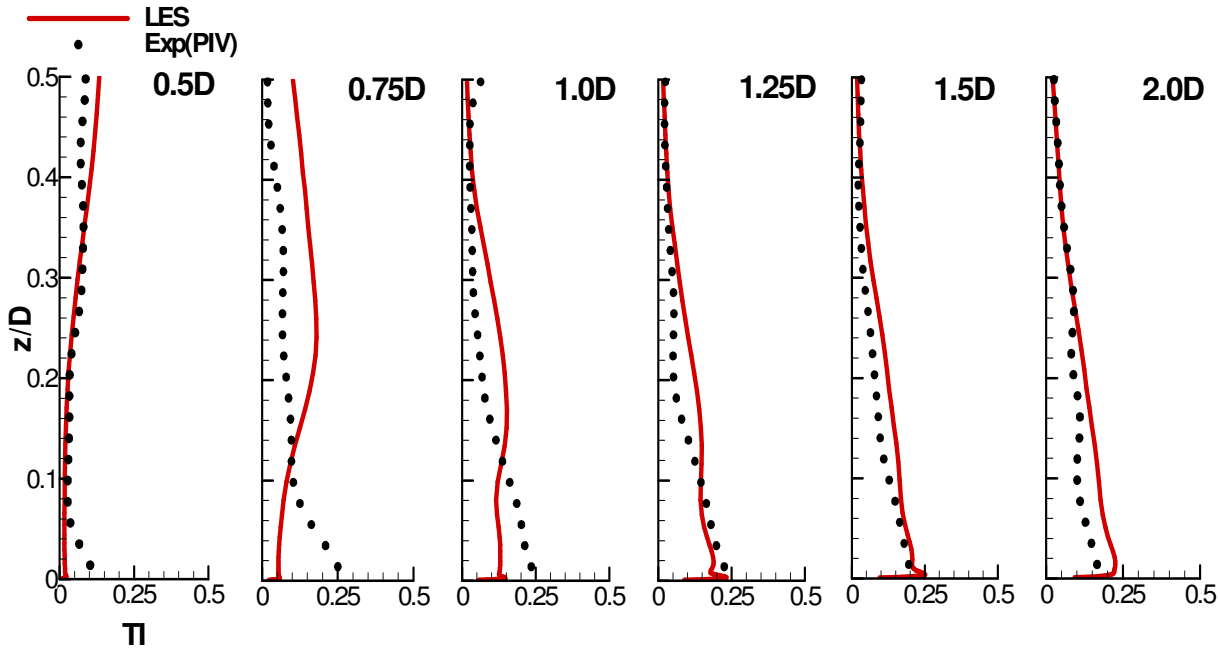

Figure 12: Radial turbulence intensity profiles

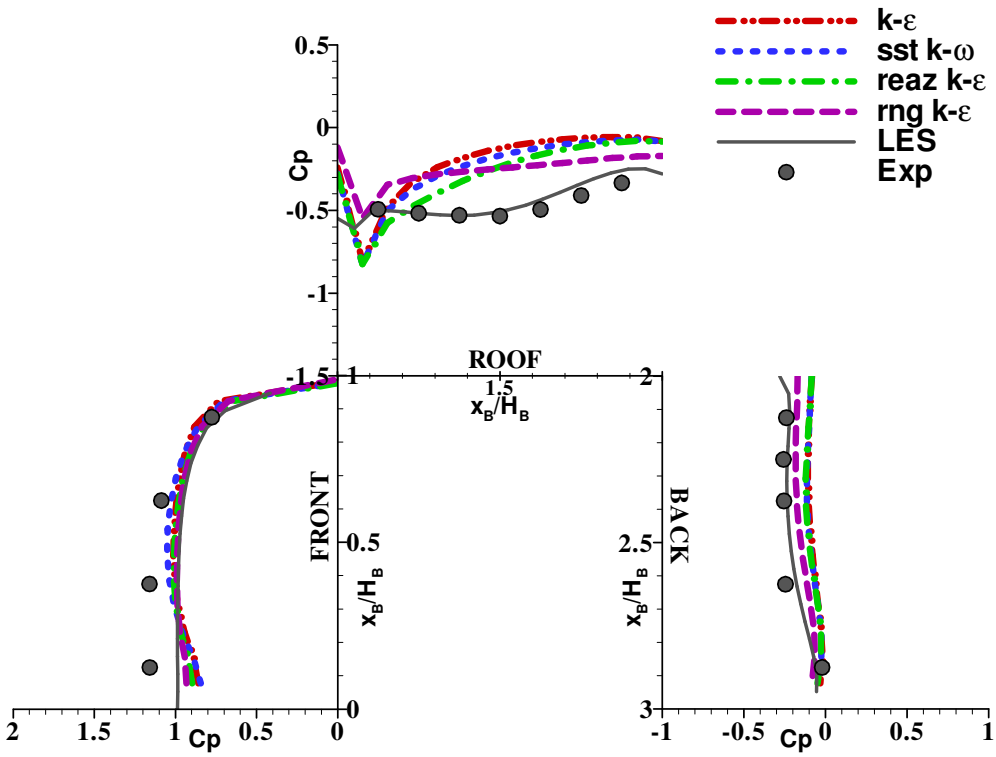

Figure 13: Plot of Pressure Coefficients on Building at 1D

CHAPTER 3

LABORATORY AND NUMERICAL SIMULATIONS TO STUDY THE WIND LOADING EFFECTS OF MICROBURST ON CUBIC BUILDINGS

A paper to be submitted to the Journal of Fluids and Structures

Anindya Sengupta [1, 2] and Partha P. Sarkar[1, 3]

Abstract:

This paper evaluates the reliability of numerical simulation to simulate microburst type wind loads on buildings. The outcome is better understanding of wind loads on buildings produced by microburst-generated outflows. In the laboratory, the natural microburst downdraft phenomenon and spreading out is replicated using a round jet impinging onto a flat plate. An extensive experimental study was conducted using different building models, jet velocities and jet heights. The effects of the static microburst at various distances from the building were studied. In the numerical simulation different RANS and LES models were used to replicate the laboratory setup. The results of numerical simulation were compared to the experimental results. There is good agreement between numerical and experimental simulations indicating that CFD can be used effectively to simulate such a complex flow.

Keywords: Microburst; Impinging jet; RANS; LES; Mean Pressure; Cubic building, PIV

[1] Graduate Student and Professor respectively, Department of Aerospace Engineering, Iowa State University
[2] Primary researcher and author
[3] Author for correspondence

1. Introduction

Microbursts occur in thunderstorms where the weight of the precipitation and the cooling due to microphysical processes act to accelerate the air downwards. Observations suggest that approximately five percent of all thunderstorms produce a microburst which is characterized by a strong localized down-flow and an outburst of strong winds near the surface.

The current research focuses on the simulation of a stationary microburst using both experimental and numerical methods. Here the microburst is modeled as an impinging jet. Jet impingement is a technique for enhancing heat transfer that is used in a variety of cooling applications from electronics to gas turbines. An intensive parametric study was conducted with different jet exit velocities, height of jet above impingement surface and building heights. Two cubic building models (B1: 12.7 mm and B2: 25.4 mm) were used. Digital pressure transducers were used to measure the pressures on the ground plane as well as on the building models. Particle Image Velocimetry (PIV) was used for flow visualization.

Different turbulence models, such as k-ε and its variants (RNG and realizable k-ε), k-ω, and Large Eddy Simulation (LES), were used to find out which numerical scheme produced results that best matched the experimental data for pressure and velocity field characteristics surrounding the buildings under microburst type wind flow.

2. Background and Motivation

Fujita (1985) termed microburst as a small downdraft having an outburst of damaging winds with the horizontal extent of the damaging winds being less than 4 km. This definition has been modified by radar meteorologists: they require the peak-to-peak differential

Doppler Velocity across the divergent center to be greater than 10 m/s and the distance between these peaks be less than 4 km. Unlike tornado winds, which converge and rise, microburst winds descend and spread outward. After striking the ground, the powerful outward running gust can wreak further havoc along its path. Damage associated with a microburst is often mistaken for the work of a tornado, particularly if the damage is directly under the microburst. However, damage patterns away from the impact area are characteristic of straight-line winds rather than the twisted pattern of tornado damage. Thus, the signature of damage on the ground can be distinguished in a "microburst" compared to a "tornado". An intense microburst can result in damaging winds with a maximum speed of 270 km/hr (170 mph) that often last for less than five minutes.

The extent of work done to study the effects of microburst wind on civil engineering structures is limited, compared to that of natural boundary layer type wind flow. The flow characteristics of the microburst have been studied by a few researchers. Selvam and Holmes (1992) undertook numerical modeling of the thunderstorm downdraft phenomenon using a 2D impinging jet model, and were able to demonstrate reasonable agreement between a numerical model (k-ε) and limited full-scale data. Holmes and Oliver (2000), Letchford and Illidge (1999) and Wood et. al. (2001) undertook physical model studies of a jet impinging on a wall to study topographic effects on velocity profiles in a microburst. Oliver et. al (2000) and Savory et. al. (2001) looked at transmission line failures due to microburst. Chay and Letchford (2002) measured velocity profiles on a ground plane in a stationary microburst using an inverted impinging jet. In reality, the microburst is a very short-term phenomenon and usually translates horizontally. A ring vortex has been observed to form in a microburst as the leading edge of the downdraft interacts with the ground and the flow spreads outwards.

The horizontally translating ring vortex in a stationary or moving microburst is expected to produce dynamic effects on the velocity profiles. Yao and Lundgren (1996) and Alahyari and Longmire (1995) have conducted several laboratory experiments using fluids of different density to understand the effects of downburst on aircrafts in flight. They were able to incorporate the effect of buoyancy in their simulation and produce a ring vortex.

In the literature, only a few case studies on microburst type wind effects on building structures have been found that are mentioned as follows. Nicholls et al. (1993) performed a numerical simulation using 2D LES to simulate the microburst type flow on a building. Mudgal and Pani (1999) used a wall jet to study its effects on building models. Sengupta et al. (2001) studied the microburst effect on building models experimentally and compared them to 2D numerical simulations. Chay and Letchford (2002) also studied the effects of microburst on a cubic building model using their inverted impinging jet in the laboratory for a fixed height of the jet. Sengupta and Sarkar (2006) used RANS to study microburst flows.

A survey of existing literature on microburst wind effects on structures reveals that this subject area has not been extensively studied in the past, especially for the case of microburst type wind loads on buildings considering different building sizes, distance of the building from the microburst center or the height of the microburst.

The primary objectives of the present work were: (a) to perform a systematic parametric study of laboratory simulation of stationary microburst using an impinging jet to determine the pressure distribution on cube-shaped buildings. The effects of height of the microburst, size of the building and its location with respect to the center of the microburst were the main focus of the parametric study, (b) application of CFD to simulate the laboratory microburst

phenomenon with jet impingement using different turbulence models, and (c) comparison of CFD results with those of the experiments to determine the most suitable turbulence model.

3. Experimental Setup

The experimental setup is shown in Figure 1. The microburst is modeled as a jet coming out of a duct and impinging on a wooden platform placed below. A nozzle diameter (D) of 203 mm (8 in.) was used to produce the jet. Air at atmospheric pressure and temperature is sucked in through the inlet of a small centrifugal fan mounted on top of the nozzle. The distance (H) of the ground plane or impinging platform (L = 2.44 m (96 in.) and B = 1.22 m (48 in.) from the nozzle could be varied from a minimum of 203 mm (8 in.) to a maximum of 826 mm (32.5 in.) using a mechanical jack. A honeycomb and two screens were used to reduce the turbulence of the issuing jet. A 3:1 area contraction was used at the nozzle end to make the velocity of the issuing jet uniform. For the current work, H = 206 mm (8.125 in.), H/D = 1.02; H = 403 mm (15.875 in.), H/D = 1.98; and H = 587 mm (23.25 in.), H/D = 2.91 were used. Henceforth, these three heights are termed as H1, H2 and H3, respectively. The H/D ratio for this study was chosen to be within the range of H/D values of a microburst that varies between 0.75 and 7.5. Two jet velocities were used, $V_j \approx 10$ m/s (32.8 ft/s) and $V_j \approx 16$ m/s (52.5 ft/s). Henceforth, these two velocities are termed as V1 and V2, respectively. This resulted in a Reynolds number of 1.4×10^5 and 2.2×10^5, respectively, based on the diameter of the jet exit nozzle (D).

3.1 Pressure Measurement

Pressure taps were located along the mid-plane of both the building models that were tested on the front, back and top surfaces. For the first cubic building model B1 (12.7 mm or

0.5 in), a total of 9 pressure taps were used with 3 pressure taps on each of the three faces of the model on the front side, roof and the back side. In the case of the second cubic building model B2 (25.4 mm or 1.0 in), a total of 16 pressure taps were used with 4 taps on the front side, 7 on the roof and 5 on the back side. The arrangement of pressure taps for both the building models are shown in Figure 1b. A 16-channel Scanivalve pressure transducer (Digital Sensor Array or DSA 3217) was used for measuring both the static and fluctuating pressures on the building models. The data was acquired at a sampling rate of 200 Hz, which was the upper limit for the transducer.

3.2 Velocity Measurement

A PIV System (Raffel et.al, 1998, Westerweel, 1993) was used for velocity measurements. Data acquisition was done using DaVis Software package (version 6.2, 2003) which is a 32 bit image-acquisition and processing software. A dual processor Pentium computer running Windows 2000 was used for this purpose. Olive oil was used as seeding that was injected into the flow using an atomizer (ATM210) and flexible tubing. A New Wave Research Gemini double pulsed PIV Nd:YAG 120 mJ laser was used with a 15 Hz repetition rate. The camera used was a FlowMaster 3S CCD camera, SONY ICX 085. The CCD resolution was 1280 x 1024 pixels, resulting in a pixel size of 6.7 µm x 6.7 µm. It is a 12-bit camera capable of taking 8 single frames per second, with a minimum inter-framing time of 300 ns. The camera was mounted on a tripod whose height could be adjusted.

Double frame/Double exposure (cross-correlation) mode was used for acquiring the images. Depending on the velocity of the jet, the time interval δt was found to lie between 50-100 mµs for the current set of experiments. Here $\min(0,4) \leq \delta t \leq \min(L,C)$, where L = 1/(laser repetition rate) and C = 1/(camera repetition rate). To ensure proper optical access,

the building models were made of plexi-glas. This ensured that the laser light sheet could pass through the middle plane of the building model, so that the vector field around the building could be processed. On an average, about two hundred to two hundred and fifty (200-250) samples were collected to ensure convergence of statistical quantities, like mean and rms velocity of the flowfield. An initial interrogation window size of 64 x 64 pixels and a final initial interrogation window size of 32 x 32 were used with a 50 % overlap, resulting in a grid spacing of 16 pixels. An adaptive multi-pass filter with decreasingly smaller window sizes (2 passes) was used. The setup is shown in Figure 1a and the pressure tap arrangement is shown in Figure 1b.

4. Numerical Simulation

The Reynolds Averaged Navier-Stokes (RANS) equations contains the term $-\rho\overline{u_i'u_j'}$ which is defined as the Reynolds stress tensor and needs to be numerically modeled to close the equation. The Reynolds stress tensor is obtained by the averaging process. In RANS the Reynolds stress is computed using an eddy viscosity μ_t. For Standard, RNG and Realizable k–ε models, μ_t is a function of both k (turbulent kinetic energy) and ε (turbulence dissipation rate) whereas in the case of k–ω models it is a function of k and ω (specific dissipation rate). A brief discussion of the RNG k–ε and SST k–ω model is given below. More details about these two models as well as the standard k–ε and realizable k–ε model used can be found in Fluent (2005).

4.2 *RNG k–ε Model*

The RNG k-ε model (renormalization group theory) is an extension of the standard k–ε model. The RNG model differs from the standard k–ε model by the inclusion of an extra

term R in the right hand side of the ε equation. In the RNG model, the following transport equations for turbulent kinetic energy (k) and its rate of dissipation (ε) are used:

$$\frac{\partial}{\partial t}(\rho k)+\frac{\partial}{\partial x_i}(\rho k u_i)=\frac{\partial}{\partial x_j}\left[\left(\mu+\frac{\mu_t}{\sigma_k}\right)\frac{\partial k}{\partial x_j}\right]+G_k+G_b-\rho\varepsilon+S_k \tag{1}$$

$$\frac{\partial}{\partial t}(\rho \varepsilon)+\frac{\partial}{\partial x_i}(\rho \varepsilon u_i)=\frac{\partial}{\partial x_j}\left[\left(\mu+\frac{\mu_t}{\sigma_\varepsilon}\right)\frac{\partial \varepsilon}{\partial x_j}\right]+C_{1\varepsilon}\frac{\varepsilon}{k}(G_k+C_{3\varepsilon}G_b)-C_{2\varepsilon}\rho\frac{\varepsilon^2}{k}+-R+S_\varepsilon \tag{2}$$

The extra term R depends on the rate of strain, as given by:

$$R=\frac{\rho C_\mu \eta^3\left(1-\eta/\eta_0\right)}{\left(1+\beta\eta^3\right)}\left(\frac{\varepsilon^2}{k}\right) \tag{3}$$

where $\eta = Sk/\varepsilon$. The model constants for RNG k–ε model (FLUENT, 2005) are given by:

$C_{1\varepsilon} = 1.42$, $C_{2\varepsilon} = 1.68$, $C_\mu = 0.0845$, $\sigma_k = 1.0$, $\sigma_\varepsilon = 1.3$, $\eta_0 = 4.38$ and $\beta = 0.012$.

4.4 Shear-Stress Transport (SST) k-ω Model

This is a variation of the standard k-ω model proposed by Wilcox (1999). In this model, in addition to the standard k equation, another equation for length (ω) is solved. This quantity (ω) is often called specific dissipation and it is defined as $\omega \propto \varepsilon/k$. The modeled k and ω equations are given by (FLUENT, 2005):

$$\frac{\partial}{\partial t}(\rho k)+\frac{\partial}{\partial x_i}(\rho k u_i)=\frac{\partial}{\partial x_j}\left[\Gamma_k\frac{\partial k}{\partial x_j}\right]+G_k-Y_k+S_k \tag{4}$$

$$\frac{\partial}{\partial t}(\rho \omega)+\frac{\partial}{\partial x_i}(\rho \omega u_i)=\frac{\partial}{\partial x_j}\left[\Gamma_\omega\frac{\partial \omega}{\partial x_j}\right]+G_\omega-Y_\omega+D_\omega+S_\omega \tag{5}$$

In the SST k-ω model, the definition of turbulent viscosity is modified to account for the transport of the principal turbulent shear stress and this feature enables this model to perform

better than the standard k-ε and standard k-ω model. There is also a cross-diffusion term D_ω added to the ω equation.

4.5 Large Eddy Simulation (LES)

In LES the velocity field is separated into two distinct parts, namely the resolved part ($\overline{u}_i$) which represents the larger scales or eddies and the subgrid (or modeled) part (u_i') which represents the smaller scales. We need to include the effect of these small scales on the resolved field through the use of a subgrid-scale model. To separate the large scales from the small scales, a filtering operation is performed. A filtered variable is defined as

$$\overline{f}(x) = \int_D f(x')G(x-x')dx' \tag{6}$$

where D is the entire flow domain and G is the filter function which determines the size and structure of the small scales which requires modeling. For a top hat filter in real space,

$$G(x-x') = \begin{cases} 1/\Delta, & |x-x'| \le \Delta/2 \\ 0, & otherwise \end{cases} \tag{7}$$

where $\Delta = (\Delta_1\Delta_2\Delta_3)^{1/3}$. Applying the filtering operation, we get the following equations for continuity and momentum for an incompressible flow;

$$\frac{\partial \overline{u}_i}{\partial x_i} = 0 \tag{8}$$

$$\frac{\partial \overline{u}_i}{\partial t} + \frac{\partial \overline{u}_i \overline{u}_j}{\partial x_j} = -\frac{1}{\rho}\frac{\partial \overline{p}}{\partial x_i} - \frac{\partial \tau_{ij}}{\partial x_j} + \nu \frac{\partial^2 \overline{u}_i}{\partial x_j \partial x_j} \tag{9}$$

The term τ_{ij} called the subgrid-scale (SGS) stress is given by

$$\tau_{ij} = \overline{u_i u_j} - \overline{u}_i \overline{u}_j \tag{10}$$

The role of the SGS stress is to remove energy from the large or resolved scales. The subgrid-scale stresses resulting from the filtering operation requires modeling. The subgrid-scale turbulent stresses are computed using the eddy-viscosity model:

$$\tau_{ij} - \frac{1}{3}\tau_{kk}\delta_{ij} = -2C\Delta^2 \left|\overline{S}\right| \overline{S}_{ij} \tag{11}$$

Here $C = C_S^2$, $\left|\overline{S}\right| = \sqrt{2\overline{S}_{ij}\overline{S}_{ij}}$ and $\overline{S}_{ij}$ is the rate-of-strain tensor for the resolved scale defined by

$$\overline{S}_{ij} \equiv \frac{1}{2}\left(\frac{\partial \overline{u}_i}{\partial x_j} + \frac{\partial \overline{u}_j}{\partial x_i}\right) \tag{12}$$

In the dynamic SGS model (Germano et al. (1991), two different filters are applied. In addition to the grid filter G (Δ), a test filter $\hat{G}$ ($\hat{\Delta}$) is also applied. In general the test filter is larger than the grid filter and usually $\hat{\Delta}$ = 2Δ. Applying both the filters to the Navier-Stokes equation results in;

$$\frac{\partial \hat{\overline{u}}_i}{\partial t} + \frac{\partial \hat{\overline{u}}_i \hat{\overline{u}}_j}{\partial x_j} = -\frac{1}{\rho}\frac{\partial \hat{\overline{p}}}{\partial x_i} - \frac{\partial T_{ij}}{\partial x_j} + \nu \frac{\partial^2 \hat{\overline{u}}_i}{\partial x_j \partial x_j} \tag{13}$$

The above filtering result in subtest-scale stresses (as in equation 10)

$$T_{ij} = \widehat{\overline{u_i u_j}} - \hat{\overline{u}}_i \hat{\overline{u}}_j \tag{14}$$

Applying the test filter to the grid filtered equation (Eq. 9) results in

$$\frac{\partial \hat{\overline{u}}_i}{\partial t} + \frac{\partial \hat{\overline{u}}_i \hat{\overline{u}}_j}{\partial x_j} = -\frac{1}{\rho}\frac{\partial \hat{\overline{p}}}{\partial x_i} - \frac{\partial \hat{\tau}_{ij}}{\partial x_j} + \nu \frac{\partial^2 \hat{\overline{u}}_i}{\partial x_j \partial x_j} - \frac{\partial L_{ij}}{\partial x_j} \tag{15}$$

Here the dynamic Leonard stresses L_{ij} is defined as

$$L_{ij} = \widehat{\overline{u}_i \overline{u}_j} - \hat{\overline{u}}_i \hat{\overline{u}}_j = T_{ij} - \hat{\tau}_{ij} \tag{16}$$

Assuming the same functional form for T_{ij} as in equation 11, we get

$$T_{ij} - \frac{1}{3} T_{kk} \delta_{ij} = -2C\hat{\Delta}^2 \left|\hat{\bar{S}}\right| \hat{\bar{S}}_{ij} \tag{17}$$

Substituting equation 11 and 17 into the expression for L_{ij} in equation 16, we get

$$L_{ij} - \frac{1}{3} \delta_{ij} L_{kk} = -2C(\hat{\Delta}^2 \left|\hat{\bar{S}}\right| \hat{\bar{S}}_{ij} - \Delta^2 \widehat{\left|\bar{S}\right| \bar{S}_{ij}}) \tag{18}$$

Using $M_{ij} = (\hat{\Delta}^2 \left|\hat{\bar{S}}\right| \hat{\bar{S}}_{ij} - \Delta^2 \widehat{\left|\bar{S}\right| \bar{S}_{ij}})$, the error $Q = (L_{ij} - \frac{1}{3} \delta_{ij} L_{kk} - 2CM_{ij})^2$ is minimized using a least squares minimization suggested by Lilly (1992) using the relationship $\frac{\partial Q}{\partial C} = 0$ giving

$$C = -\frac{1}{2} \frac{L_{ij} M_{ij}}{M_{ij} M_{ij}} \tag{19}$$

Here $C = C(x_i, t)$ i.e. a function of both space and time. To avoid numerical instability, the value of C is clipped at zero.

4.6. Numerical Simulation Parameters

For all the RANS models, the QUICK scheme was used for the convective fluxes as this reduces the numerical diffusion, and 2nd Order schemes for k, ε and ω terms were chosen. The SIMPLE algorithm was used for pressure correction. The RANS models were run both with the non-equilibrium wall functions as well as enhanced wall treatment. The second option resulted in slightly improved result, and is as such presented in this paper. The enhanced wall treatment adopted required more computational cells and a fine mesh with $y^+ < 1$ was ensured for all regions, especially the ground and the building faces.

For LES, the Fractional Step method (FSM) was used for pressure-velocity coupling in case of static jet simulation. This non-iterative (NITA) scheme uses much less computation time compared to the iterative (ITA) schemes with PISO, although the results were almost

the same using either of the above mentioned scheme. Initially LES simulations for the static jet case were performed using the both the constant Smagorinsky [Fluent 2005] and dynamic Smagorinsky-Lily [Fluent 2005] model. It was seen that the results of the dynamic model matched the experimental data better and henceforth all the simulations were conducted using the dynamic smagorinsky model only. A bounded central difference scheme was used for the convective terms and an implicit scheme was chosen for temporal discretization.

In the numerical simulations, the air density was taken as 1.225 kg/m^3 and the air viscosity as 1.7894E-05 Ns/m^2. The inlet values of turbulence intensities were substituted from the experimental data. Also fully converged solutions were obtained after setting the residual errors for all variables to be less than $1x10^{-6}$, except for continuity for which it was less than $1x10^{-8}$. The validity of the numerical simulation was checked using different domain and grid sizes as well as time steps (LES only). For the simulation results presented here, the RANS model for the static jet case consists of approximately 0.7 to 1.9 million cells (half model). The results presented here are with 1.1 million cells. For the static jet LES simulations, 1.4 to 2.0 million cells were used depending on the location of the jet. Grid stretching and clustering near the walls enabled us to achieve a mean y+ value of 1 for the ground plane wall and the building walls for both RANS and LES simulations.

The simulations were carried out using Fluent [8] in our computational laboratory consisting of PC's with 2GB of RAM and using dual CPU Intel Xeon processors running Red Hat Linux OS. An AMD dual CPU Opteron 64 bit machine was used later to validate our LES simulations with about 2.75 million cells. Figure 2a shows a typical mesh used for the LES simulation when the building is directly under the jet for a jet height of 1D, whereas Figure 2b shows the mesh for the case when the building is at 1D from the center of the jet.

5. Results and Discussion

Each laboratory case of pressure measurement corresponds to an average of five identical runs. The pressure coefficient C_p was normalized with the jet exit velocity V_J, where C_p is defined as:

$$Cp = \frac{(P - P_S)}{0.5\rho V_j^2} \tag{20}$$

The experimental results are presented first, followed by those from the numerical simulation and their comparison with the experiments.

5.1 Experimental Results

The effect of the building model size is presented first. Figure 3 shows the comparison of the centerline Cp plots for buildings B1 and B2 for jet height H2. Initially, the effects of the static jet on these two building models at various distances from the jet centerline were studied. In Figure 3a, when the buildings are placed directly under the jet, they are subjected to a significant amount of negative lift (downward force). The jet downdraft reaches the building before impinging on the ground. When the buildings are at a distance of 0.5D from the center of the jet, they are still partly under the direct impact of the jet downdraft and as such the pressure distribution on the roof is still positive and there is no flow separation on the roof of the building similar to building location 0D. A slight dip in the positive pressures near the front edge of the roof for building B1 is observed, contrary to that observed for B2 where there is an increase. Also at location 0.5D, it can be seen that the smaller building B1 is subjected to higher positive pressures on the backside of the building. In both the cases, as mentioned above, the buildings are subjected to a downward force on the roof and a positive

force on the back side. This loading is different from those produced in a regular straight-line type flow, and is not considered in the current design practice.

In a previous study of the wall jet formed due to the impinging jet (Sengupta and Sarkar, 2006), it was found that the maximum velocity occurs in the region $0.75 \leq x/D \leq 1.25$. In Figures 3c-3e, the results of the experimental data for the case when the building is in this critical zone are presented. The flow structure is now completely different than the previous two jet locations. A wall jet is now formed due to the flow impinging on the ground plane.

When the buildings are placed at 0.75D, the pressure distributions are observed to change on the roof of the building. It is seen that suction or negative pressure is produced in the front section of the roof. This is observed for both the building models. Though the pressure distributions on the front and back of the building models are identical, there is some difference in the distribution on the roof. The smaller building seems to be undergoing much larger suction pressure than the bigger one. At locations between 1.0D to 2.0D, the pressure distribution is again very much the same for both building models, except that the roof undergoes slightly more suction for model B1 compared to B2. At building location 3D, we see that there is absolutely no difference in the pressure distribution on the buildings for both models. Therefore, it can be concluded that the pressure distribution is not dependent on the height of the building model at or after a distance of 3D from the center of the jet.

The effects of the jet height are presented next. Figure 4 shows the results for building model B2, at various locations from the center of the jet. Each plot shows the pressure distribution for three different jet heights, namely H1, H2 and H3. At 0D, the pressure distribution profiles are found to be similar showing some effects due to the variation of jet height. The highest pressures occur when the jet is at height H3 and lowest occur at height

H1. Between the three heights, the difference is less than 10%. When the building is at 0.5D, jet height H2 results in the maximum pressure coefficient on all sides of the cube. A similar result is also seen at building location 0.75D. At 1.0D, the profiles on the roof are similar for all three heights except the rear of the roof, where jet height H3, produces a slightly lower value of uplift. At this location also, it is seen that the jet height H2 produces maximum pressures on the frontal face of the building compared to the other two heights. At locations 1.25D and 1.5D, the maximum roof pressures are again due to jet heights H2 as well as H3. But in this case also the maximum pressures in the front of the building occur due to jet height H2. At 2.0D and 3.0D the pressure distributions for all three heights are pretty much similar. This means that when the buildings are placed at a distance 2.0D and beyond, the height of the jet does not affect the pressure distribution on the cubes.

Three conclusions can be made regarding the wind loads on the roof of a cubic building based on the experimental results. The first is that the building undergoes maximum downward pressure when it is directly under the jet (0D). Secondly, building location 1D from the center of the static jet produced the maximum lift on the building. Thirdly, flow separation takes place on the roof as evidenced by the pressure distribution on the roof for building positions 0.75 D and beyond from the center of the jet. This is similar to what buildings experience in the natural boundary layer wind except that the 0.75D location is the transition region where the flow separates and strongly reattaches on the roof as opposed to separation without or with a weak reattachment.

5.2 Numerical Results

As stated previously, the location of the building directly under the jet is an interesting position to study for microburst type flows. Here the building experiences a downward force,

not seen in natural boundary layer type wind. In Figure 5, the numerical (LES) results of the pressure distribution on the building model B2 for velocity V1 for all the three jet heights are presented. It is seen that LES is able to predict the distribution of pressure with remarkable accuracy for jet height H1. For jet heights H2 and H3, the numerical results under-predict the experimental values. Though the LES values are within the range of experimental uncertainty, it is believed that the difference in the results could be due to the mesh size. The mesh size of 1.4 million was adequate for smaller jet height H1, but the mesh size of 1.65 and 1.9 million for jet heights H2 and H3, respectively, were probably not enough for good accuracy. Increase in mesh size could not be accomplished in the same ratio as the increase in jet impingement height because of the limited computer resources.

The validity of our LES simulations for building location at 1D was checked. The results of the mesh size distribution as well as time step variation are shown in Figure 6. In Figure 6a, the mesh size M1 corresponds to about 1.35 million (M) cells, M2 corresponds to 1.9 M cells and M3 consists of about 2.75 M cells. It is seen that the results are in good agreement for all the three mesh sizes. From now on we will discuss the results with mesh size M2 only unless stated otherwise. The effect of time step variation is shown in Figure 6b. T3 was chosen as the time step for all subsequent LES computations keeping in mind both the accuracy of the results as well as computation time. Here the non-dimensional time steps used are T1 = 0.01, T2 = 0.005, T3 = 0.0025 and T4 = 0.0005. The time steps were non-dimensionalized using the relationship $T = \frac{\Delta t * V_J}{D_J}$, where Δt is the actual physical time step used in the simulation. Note that X_B is distance along the centerline of the cubic building of side H_B starting from the bottom of the frontal face.

Next the data from the numerical simulations, using different turbulence models for building B2 at jet height H2 and jet velocity V1, are presented and compared with our experimental data. All the turbulence models discussed previously were tested for each location of the building model between 0D and 3D from the center of the jet. The results are presented in Figure 7. When the building is directly under the jet, all the models give more or less the same results and these compare well with the experimental data, with k-ε producing slightly better results, compared to other turbulence models including LES. Similarly at 0.5D all the turbulence models produce results which are close to that from the experiments. Here also k-ε and k-ω models produced results which are slightly better compared to others. Now consider the zone where the jet is no longer impinging on the building models directly but only hitting as a wall jet. At 0.75D and beyond, the building is under the influence of the wall jet. There is separation of flow on the roof as depicted by the negative pressures near the front edge of the roof. It is seen that LES does the best job of capturing the effects of the separation amongst all the numerical models, though not fully accurate. All other RANS models fail to capture the effects of the separation. The only high point about the RANS models is that k-e model does a good job of capturing the stagnation pressure on the front wall compared to others. While considering location 1D, it is recalled that this was the location of the static jet that produced the maximum lift on the building as observed experimentally. A comparison of numerical and experimental data for this location shows again that LES is the only turbulence model that is capable of predicting the overall roof pressure coefficients accurately. None of the RANS models were able to capture the pressure distribution near the leading edge of the roof accurately. The prediction of pressure coefficients with LES at 1.25D is again remarkably accurate, particularly within the

separated region of the roof. At building locations 2D and 3D, LES predictions of the centerline pressure distribution matches the experimental results perfectly. The RANS models over predicts the values on the front of the building at both of these locations.

The force coefficient values for the building model B2 at different jet locations and jet height H2 are listed in Table 1. The experimental values were determined by multiplying the centerline pressure distribution with the corresponding tributary area since only pressures along the centerline were measured. The results of the numerical simulation (both RANS and LES) are also shown. It can be seen that the drag coefficients are lower in the region $0.5 \leq x/D \leq 1.25$ for the numerical simulations compared to the experimental ones. This can be explained with Figure 8 that shows the frontal pressure distribution at 1D, as computed by LES. It is not uniform but higher at the center and lower towards the edges. The drag coefficient calculated numerically considers this fact. But the experimental drag value is calculated using the centerline pressure data only that are higher than those near the edges. The lift values for experiments are not affected using only the centerline values as it is seen from the LES calculations that the pressure distribution on the roof is banded in a favorable way.

A quick glance at Table 1 summarizes the following observations. The building experiences maximum downward force at 0D and no drag at all at this location. The drag coefficient C_D was observed to significantly increase as the building moved from 0D location to 1D location from the center of the jet. The maximum drag occurred within the zone $0.75 \leq x/D \leq 1.0$ D. At the same time, the lift coefficient changed sign from negative (or downward) to positive (or upward) and achieved a maximum positive value at 1D and then gradually reduced with increasing distance of the building from the center of the jet.

Figure 9 plots the fluctuating drag and lift coefficients as computed using LES. Figure 9a shows the drag and lift coefficients for the building at 0D whereas Figure 9b shows the corresponding values at building location 1D. It can be seen that the fluctuations in the coefficient values are more at 1D compared to 0D due to increase in turbulence intensity. The power spectral density functions of velocity and pressure fluctuations are plotted in Figure 10 for two points on the surface of the building that is located at 1D. The first point is located at tap 9 on the roof. The second point is at the back of the building in the recirculation zone, midway between taps 6 and 7. The velocities were recorded at points which were located at a normal distance of $0.25H_B$ away from these above mentioned points. The plot shows a slope of -5/3 over a decade representing the inertial sub-range. These plots show much lower frequency content of the pressures compared to what is observed in regular straight-line wind in a rough terrain. This is possibly because the upstream terrain is smooth and the upstream flow is very smooth as observed in the *rms* plots of velocity as presented later in this paper.

Observing the velocity vector plots for building B2 under the jet (location 0D, jet height H1), it is seen that there are two distinct and symmetric recirculation zones created on either side of the building as shown in Figure 11. All the turbulence models are able to capture this remarkably well, though the size of the recirculation bubble varies between the models. The velocity vector plots of both the RANS and LES models are also compared with those from experimental PIV data at location 1D as shown in Figure 12. It is observed that the RANS models fail to capture the flow features as accurately as the LES model. For example, the RANS models do not show the circulation region in front of the building and produces a longer reattachment length in the wake. The velocity vectors from LES are found to better replicate those of the PIV. It should be noted here that PIV does not capture the recirculation

in front of the base of the building. This might be due to the fact that region was not illuminated properly by the laser as it had to pass through the thick plexi-glas cube.

Figures 13 and 14 show the experimental (PIV) and numerical (LES) velocity profile comparisons. In Figure 13a, the profile locations are shown as a function of X_{BF}/H_B. The origin of X_{BF} is located at the frontal face of the building. The mean U velocity profiles from the LES simulations are in good agreement with the PIV data as shown in Figure 13b. The mean V velocity profiles are shown on Figure 14a. There is good agreement in general at all the locations except at location 4. There is some deviation at location 4, which is the location at the intersection of the frontal face and the roof of the building. The sharp rise in the V velocity due to separation as depicted numerically is missing in the PIV data. It might be due to either inadequate lighting near the wall at that location or due to low seed count. The rms of U velocity is also shown in Figure 14b and again the agreement between numerical and experimental results is very good.

6. Summary and Conclusions

The goal of the work presented here was to subject a cubic building model to simulated microburst winds to study the resulting aerodynamic loads on the building. Loads resulting from the static impinging jets at various heights and distances from the building model were studied. It was found that the larger building experiences more loads compared to the smaller one disproportionate to their sizes. Also for a microburst, the building experiences a downward force when it is directly under the center of the jet. Varying the jet height did not produce a significant change in the loads on the building, though it was seen that at jet height 2D, the load coeffients are somewhat higher in a majority of the jet locations from the center

of the building models. Amongst all the turbulence models tested, LES gives superior results compared to RANS models in most situations. Pressures on the cube computed numerically agree well compared to experimental data for the front and back sides of the cube. Separation occurs on the roof at some jet locations, and none of the RANS models are able to capture it. LES is able to capture the separation on the roof with remarkable accuracy and hence leads to better prediction of the roof pressures. There is good aggrement between LES and PIV velocity data.

References

Alahyari, A., and Longmire, E. K., (1995) Dynamics of Experimentally Simulated Microbursts. AIAAJ. 33(11)2128- 2136.

Chay M.T. and Letchford C.W. (2002) Pressure distributions on a cube in a simulated thunderstorm downburst. Part A: stationary downburst observations. J. Wind Eng. Ind. Aerodyn. 90, 711-732.

Fluent. (2005) FLUENT *User's Guide.* Release 6.2, Fluent, Inc., Lebanon, New Hampshire.

Fujita, T.T.(1985) *The Downburst: Microburst and Macroburst.* University of Chicago Press.

Germano, M., Piomelli, U. Moin, P. and Cabot, W.H. (1991) A Dynamic Subgrid-Scale Eddy Viscosity Model. Physics of Fluids, 3, 1760-1765.

Holmes, J.D. and Oliver, S.E. (2000) An Empirical Model of a Downburst. Engineering Structures. 22, 1167-1172.

Lavision (2003) Software Manual for Davis 6.2. Lavision GmbH, Gottingen, Germany.

Letchford, C.W., and Illidge, G. (1999) Turbulence and Topographic effects in Simulated Thunderstorm Downdrafts by Wind Tunnel Jet. Wind Engineering into the 21st Century, Proceedings of the Tenth International Conference on Wind Engineering, eds. A. Larsen G. L. Larose and F. M. Livesey, Denmark, June 1999, pp. 1907-1912.

Lilly, D.K. (1992) A Proposed Modification of the Germano Subgrid-Scale Closure Method. Physics of Fluids, 4, 633-635.

Mudgal, B.V. and Pani, B.S. (1998) Flow around obstacles in plane turbulent wall jets. J. Wind Eng. Ind. Aerodyn. 73 (3&4), 193-213.

Nicholls, M., Pielke R., and Meroney, R. (1993) Large eddy simulation of microburst winds flowing around a building. J. Wind Eng. Ind. Aerodyn. 46-46, 229-237.

Oliver, S.E., Moriarty, W.W. and Holmes, J.D. (2000) A Risk Model for Design of Transmission Line Systems against Thunderstorm Downburst Winds. Engineering Structures. 22, 1173-1179.

Raffel, M., Willert, C. and Kompenhans, J. (1998) Particle Image Velocimetry: A Practical Guide. Springer, Berlin.

Savory, E., Parke, G.A.R., Zeinoddini, M., Toy, N. and Disney, P. (2001) Modeling of a Tornado and Microburst-induced Wind loading Failure of a Lattice Transmission Tower. Engineering Structures. Vol. 23, 365-375.

Selvam, R. P., and Holmes, J.D. (1992) Numerical Simulation of Thunderstorm Downdrafts. J. Wind Eng. Ind. Aerodyn. 41-44, 2817-2825.

Sengupta, A. and Sarkar, P.P. and Rajagopalan, G.R.,(2001) Numerical and physical simulation of thunderstorm downdraft winds and their effects on buildings. 1st Americas Conference on Wind Engineering, 4-6 June, Clemson, SC.

Sengupta, A. and Sarkar, P.P. (2006) Physical and numerical simulation of microburst-like wind: A study of flow characteristics and surface pressures on a cube. Proc. 3rd Indian National Conf. on Wind Engineering, Kolkata, India.

Wood, G.S., Kwok, C.S., Motteram, N.A., and Fletcher, D.F., (2001) Physical and Numerical Modelling of Thunderstorm Downbursts. J. Wind Eng. Ind. Aerodyn. 89, 535-552.

Westerweel, J. (1993) Digital Particle Image Velocimetry: Theory and Application. Delft University Press, Delft.

Yao, J. and Lundgren, T.S. (1996) Experimental Investigation of Microbursts. Experiments in Fluids. 21, 17-25.

Table 1: Drag and Lift coefficients for Experimental and Numerical Simulation

Location of building from the center of the Jet	Exp*		LES		RANS Models							
					Standard k-ε		RNG k-ε		Reaz k-ε		SST k-ω	
x/D	C_D	C_L	C_D	C_L	C_D	C_L	C_D	C_L	C_D	C_L	C_D	C_L
0.00	0.01	-1.07	0.00	-0.97	0.00	-1.01	0.00	-0.97	0.00	-0.98	0.00	-1.01
0.50	0.86	-0.73	0.66	-0.66	0.76	-0.76	0.66	-0.66	0.66	-0.67	0.74	-0.75
0.75	1.21	0.05	0.96	0.05	1.03	0.12	0.93	0.07	0.94	0.09	1.00	-0.11
1.00	1.20	0.47	1.01	0.44	0.95	0.23	0.95	0.29	0.91	0.32	0.96	0.26
1.25	1.01	0.36	0.88	0.40	0.87	0.29	0.94	0.27	0.88	0.34	0.90	0.32
1.50	0.81	0.22	-	-	0.74	0.24	0.83	0.24	0.78	0.29	0.79	0.27
1.75	0.67	0.19	-	-	-	-	-	-	-	-	-	-
2.00	0.51	0.17	0.53	0.25	0.49	0.16	0.59	0.22	0.54	0.18	0.60	0.20
2.50	0.34	0.14	-	-	-	-	-	-	-	-	-	-
3.00	0.20	0.10	0.19	0.11	0.24	0.08	0.30	0.13	0.27	0.10	0.37	0.13

* Experimental values are based on mean centerline pressure distribution only.

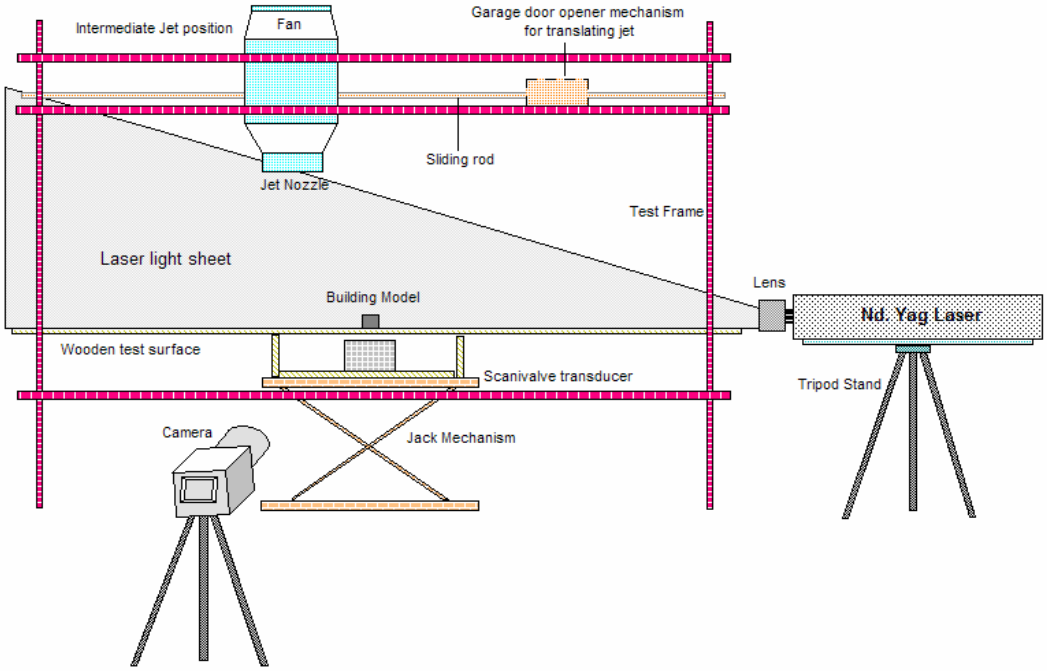

(a)

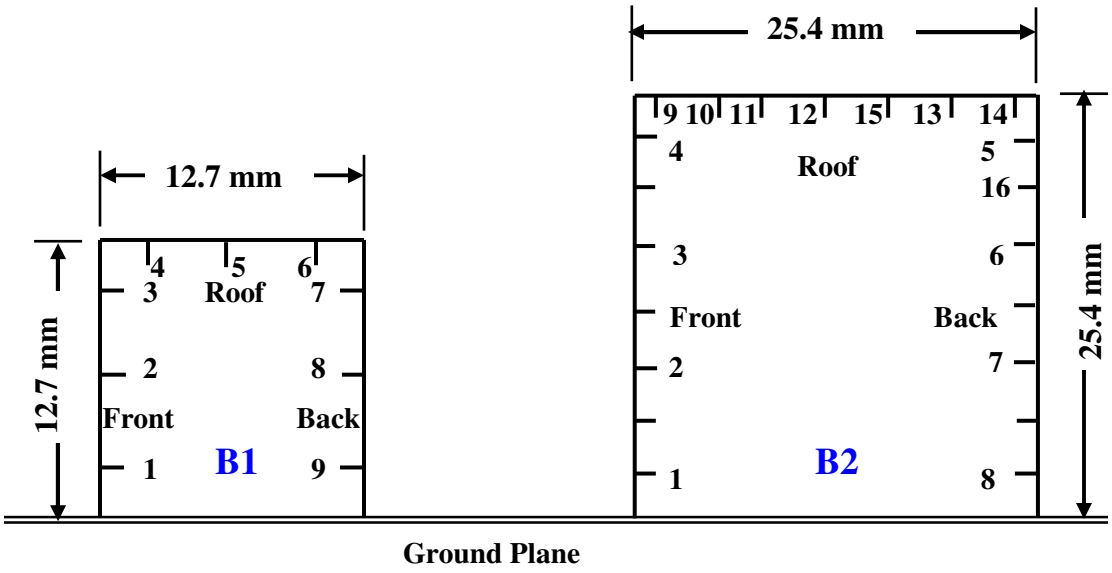

(b)

Figure 1: (a) Schematic of Impinging Jet experimental Setup with Building model
(b) Model building dimensions and pressure tap locations

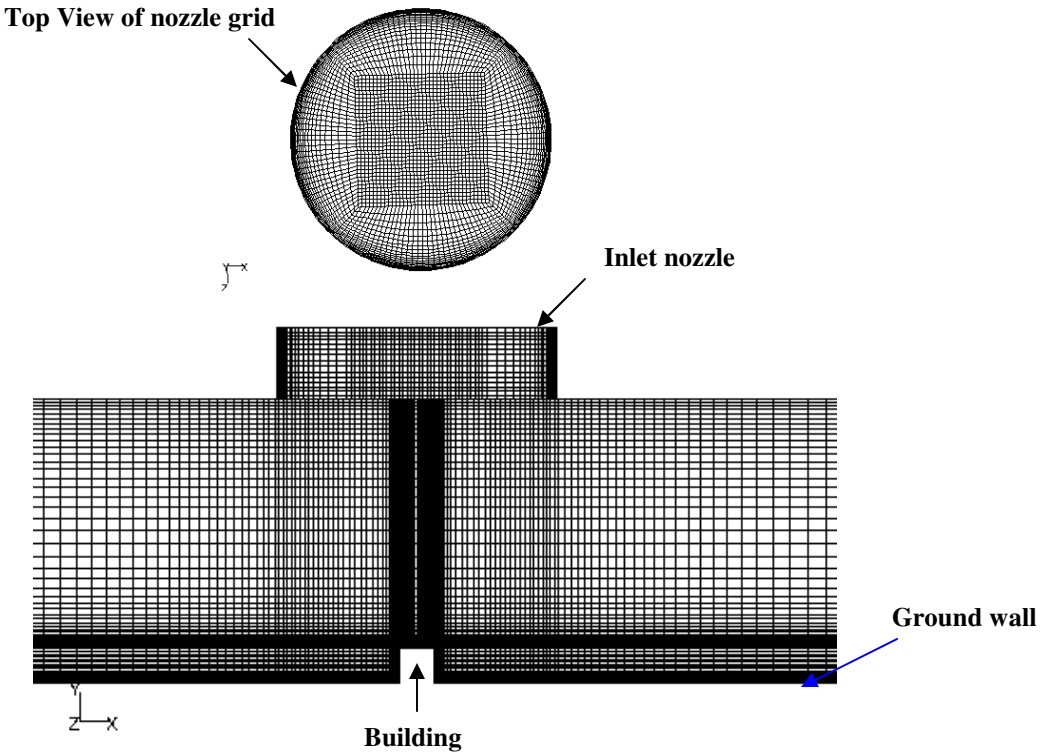

(a)

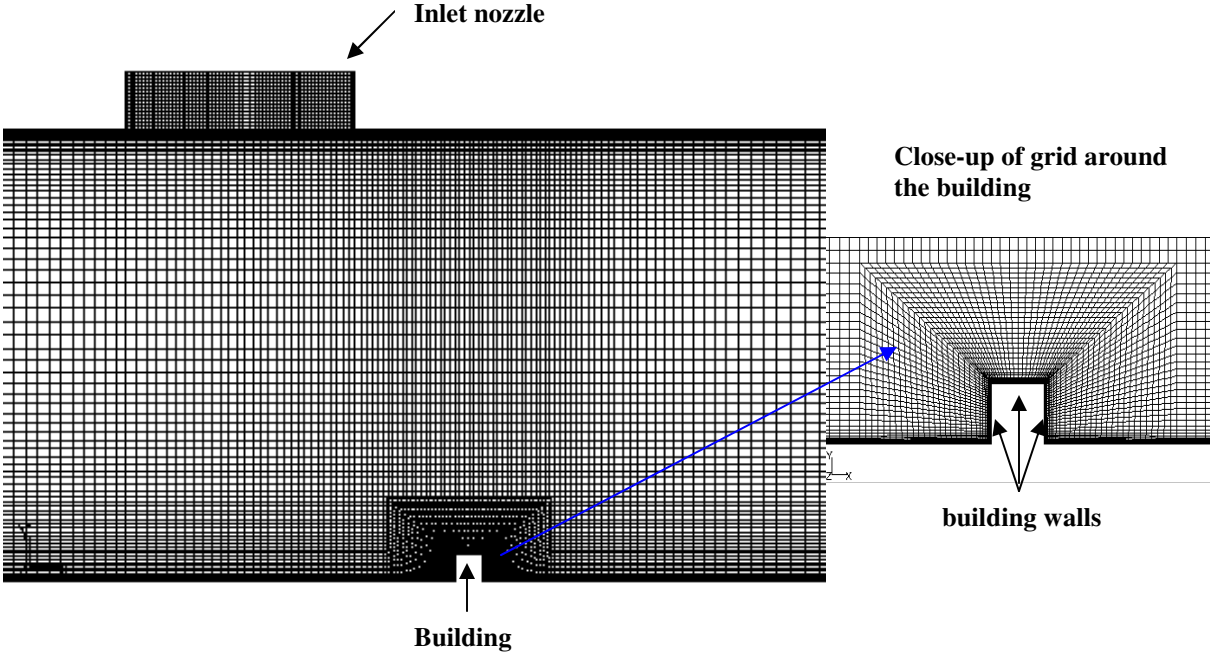

(b)

Figure 2: Grid for 3D numerical simulation (LES) along symmetry plane
(a) Building at 0D and jet height H1 (b) Building at 1D and jet height H2

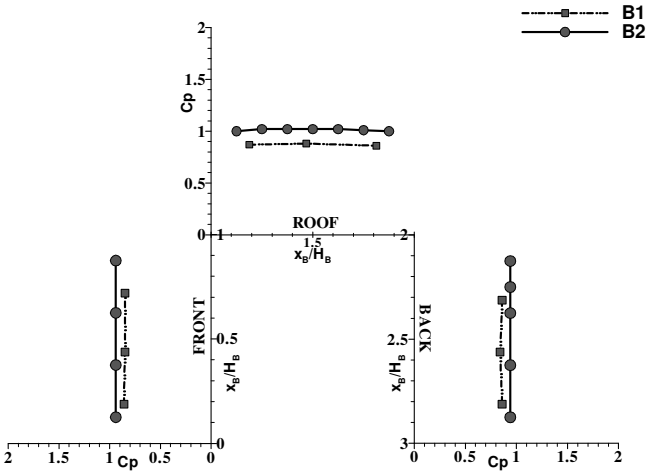

(a)

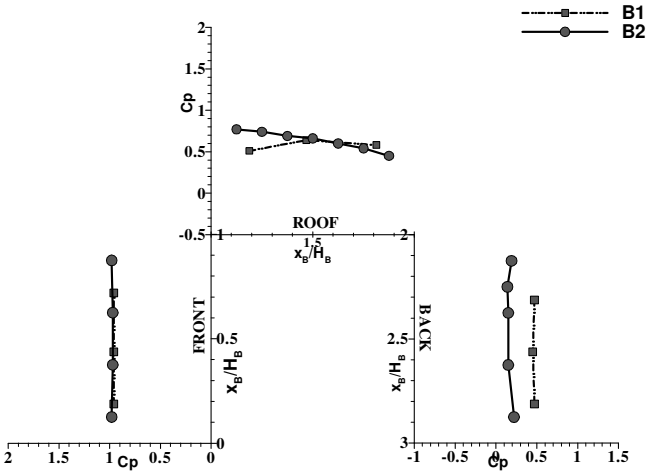

(b)

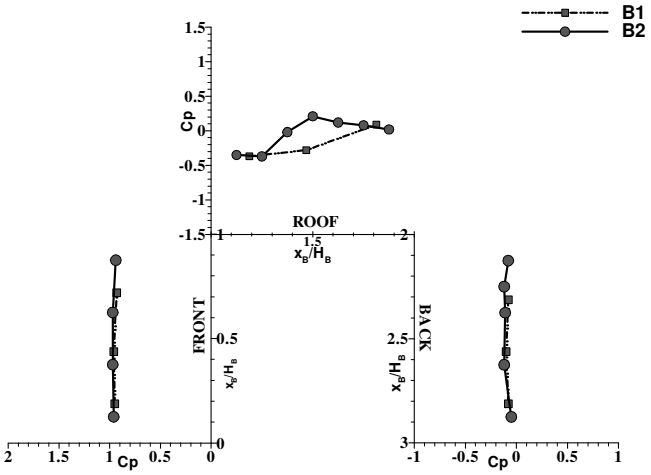

(c)

Figure 3: Comparison of Pressure Coefficients for Building B1 and B2.

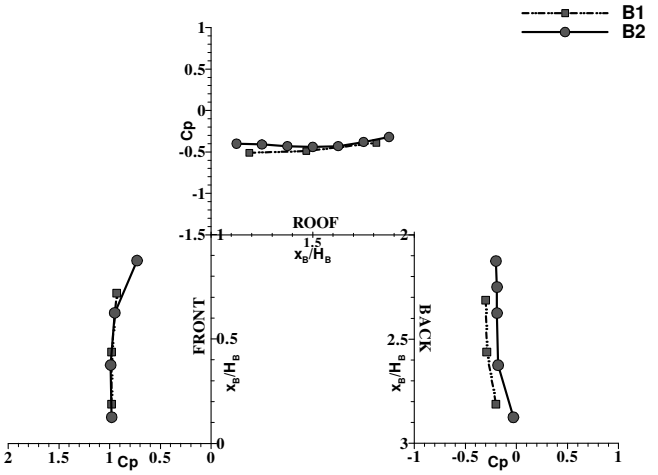

(d)

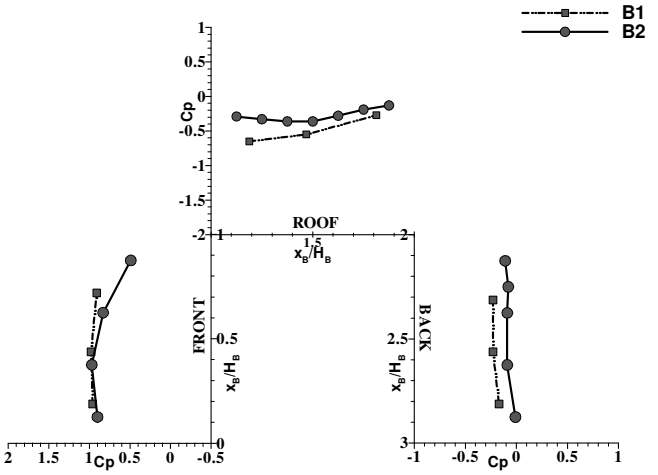

(e)

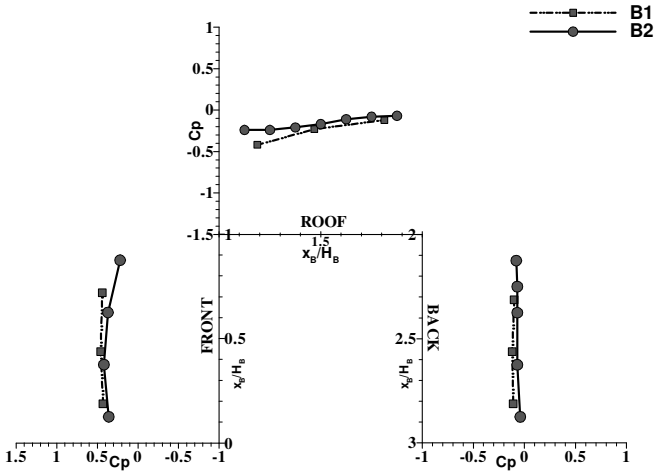

(f)

Figure 3: Comparison of Pressure Coefficients for Building B1 and B2.

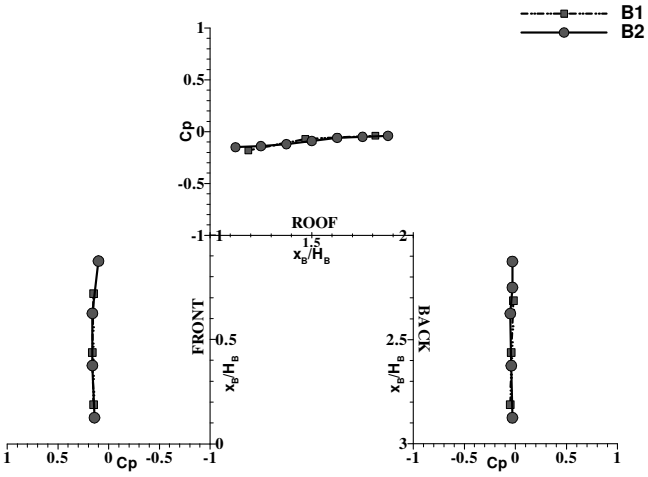

(g)

Figure 3: Comparison of Pressure Coefficients for Building B1 and B2. Buildings are placed at (a) 0d (b) 0.5D (c) 0.75D (d) 1.0D (e) 1.25D (f) 2.0D (g) 3.0D

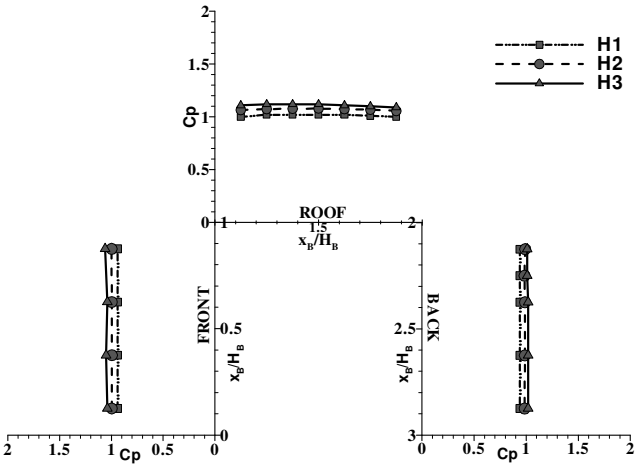

(a)

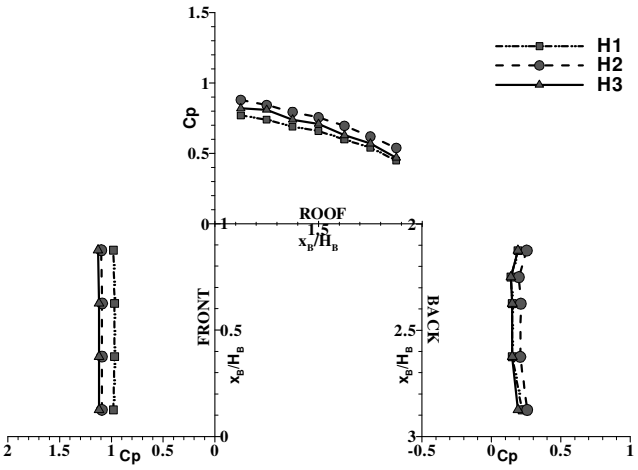

(b)

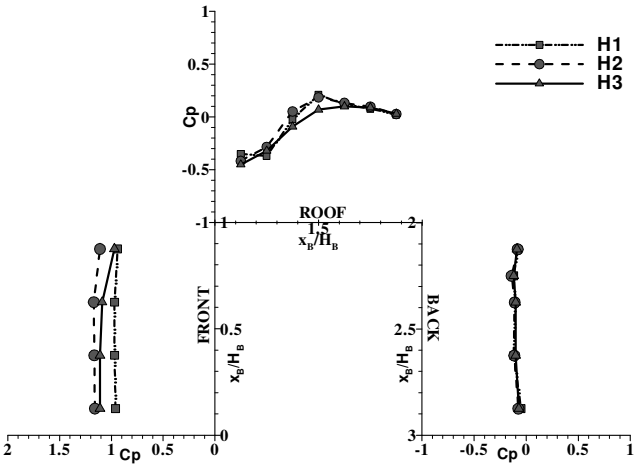

(c)

Figure 4: Comparison of Pressure Coefficients for Building B2 at heights H1, H2 and H3

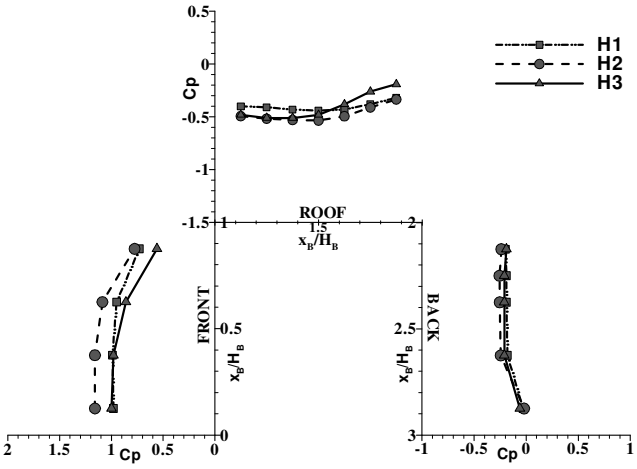

(d)

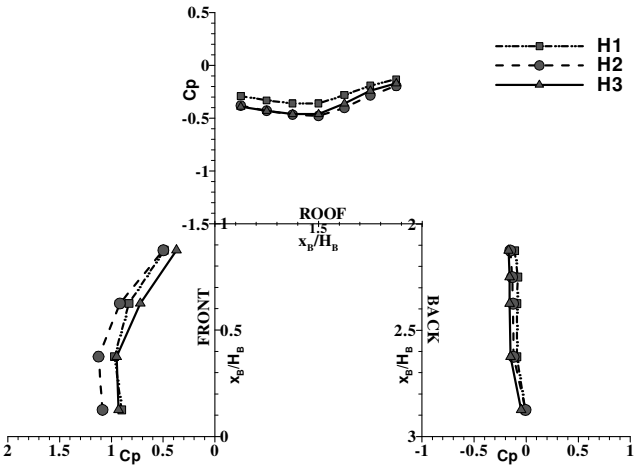

(e)

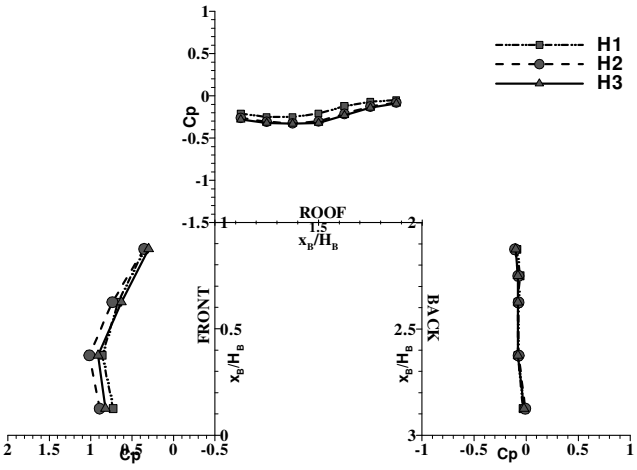

(f)

Figure 4: Comparison of Pressure Coefficients for Building B2 at heights H1, H2 and H3

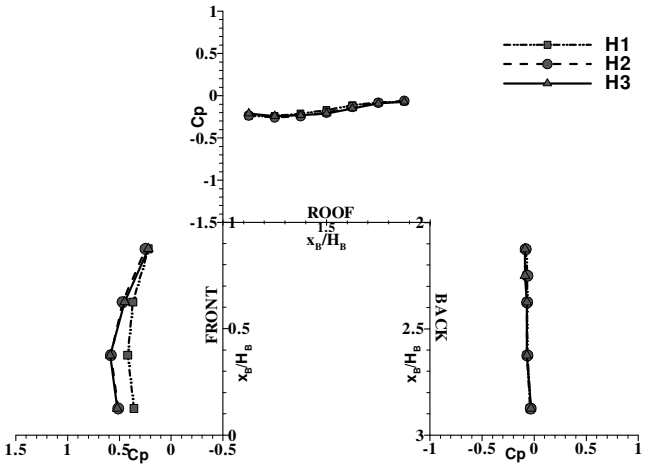

(g)

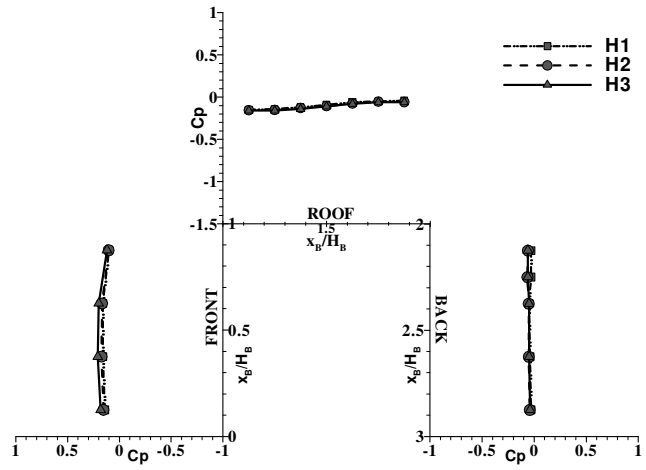

(h)

Figure 4: Comparison of Pressure Coefficients for Building B2 at heights H1, H2 and H3
Building locations are: (a) 0d (b) 0.5D (c) 0.75D (d) 1.0D (e) 1.25D (f) 1.5D
(g) 2.0D (h) 3.0D

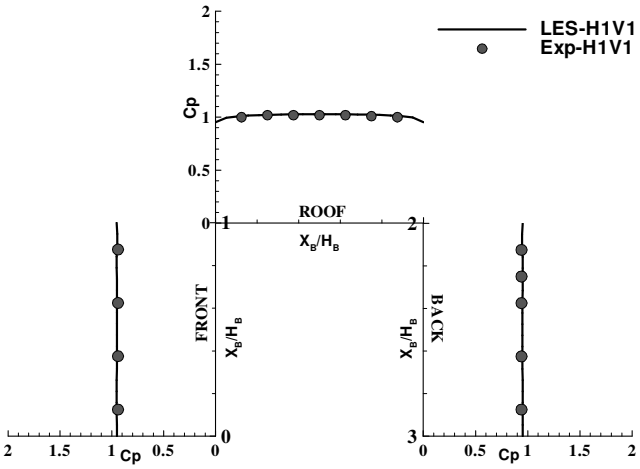

(a)

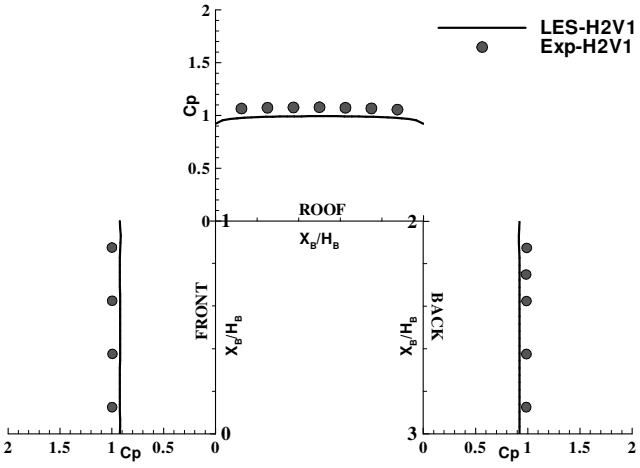

(b)

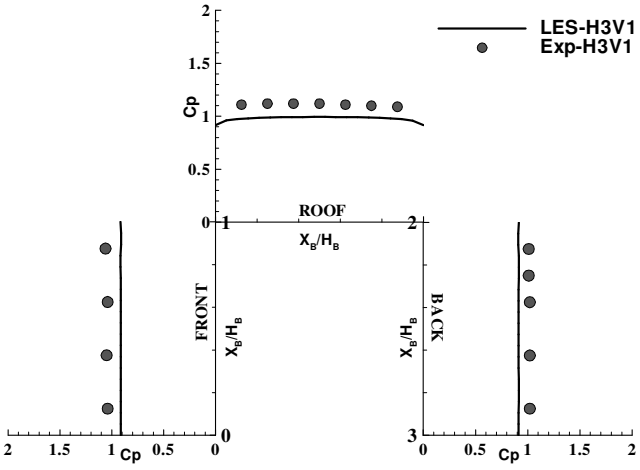

(c)

Figure 5: Comparison of Numerical and Experimental Pressure Coefficients for B2 at 0D (a) Jet at height H1, (b) Jet at height H2 and (c) Jet at height H3

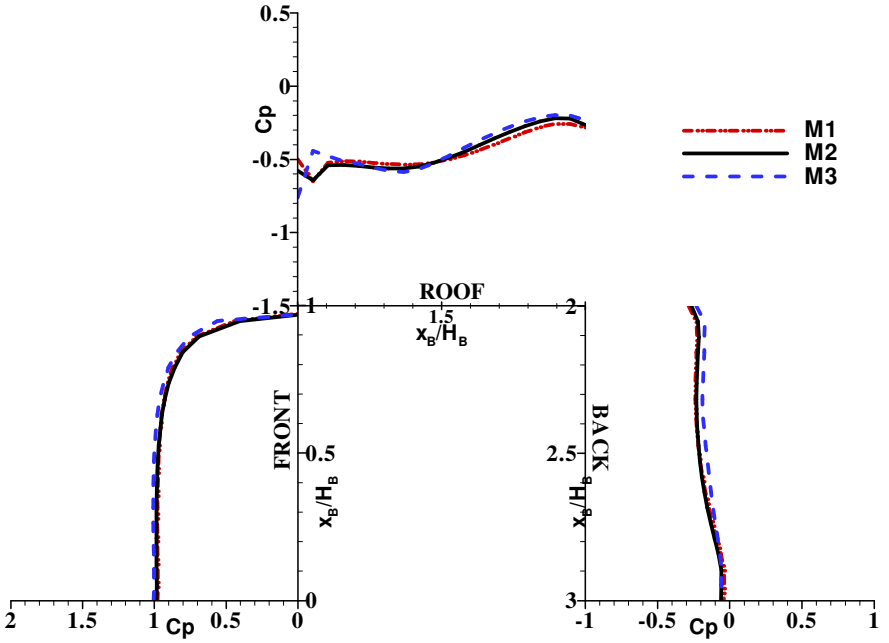

(a)

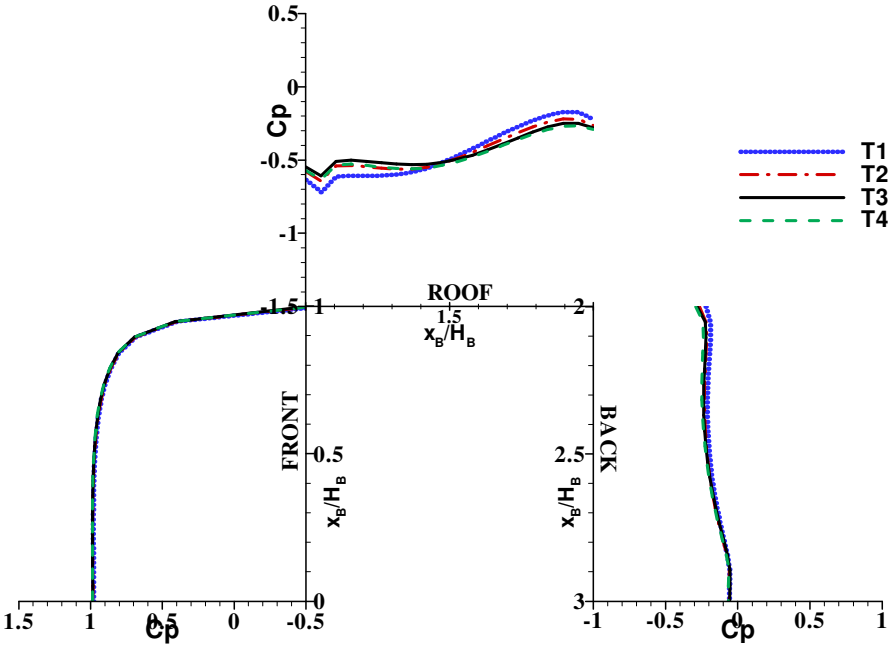

(b)

Figure 6: Validation of Numerical (LES) Simulation for B2 at 0D
(a) Mesh Size (b) Time-Step

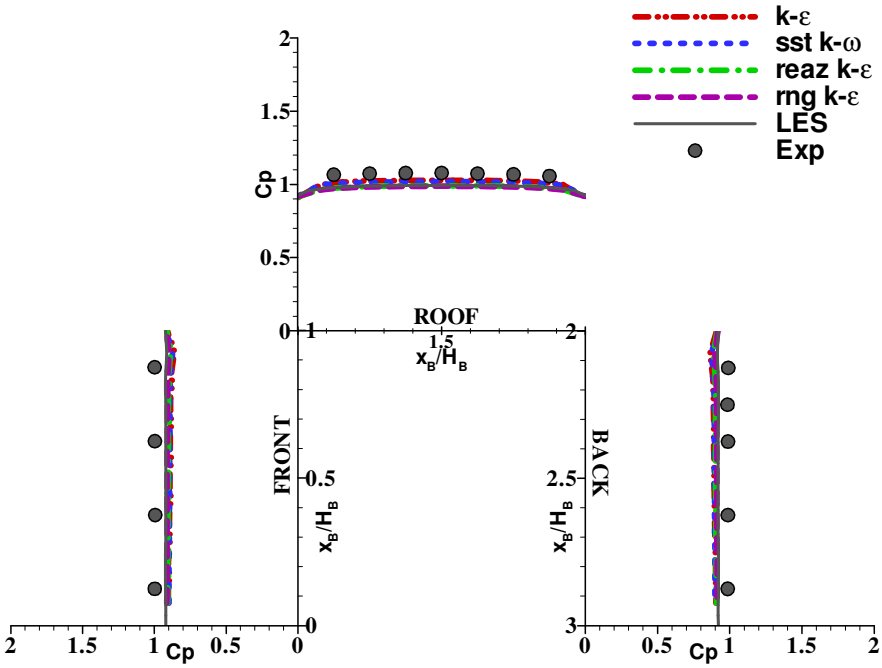

(a)

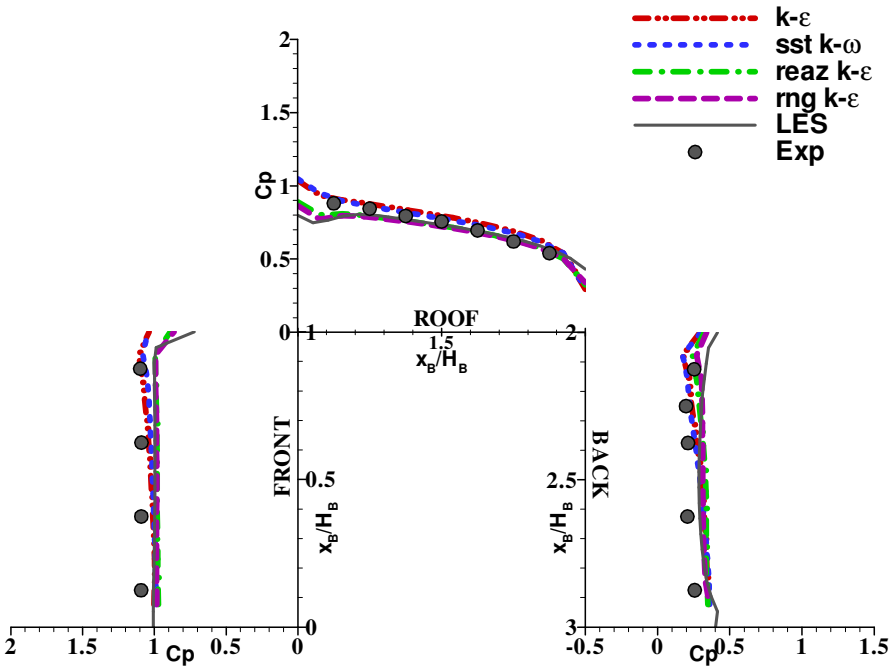

(b)

Figure 7: Comparison of Numerical and Experimental Pressure Coefficients for B2 at different locations from the center of the jet

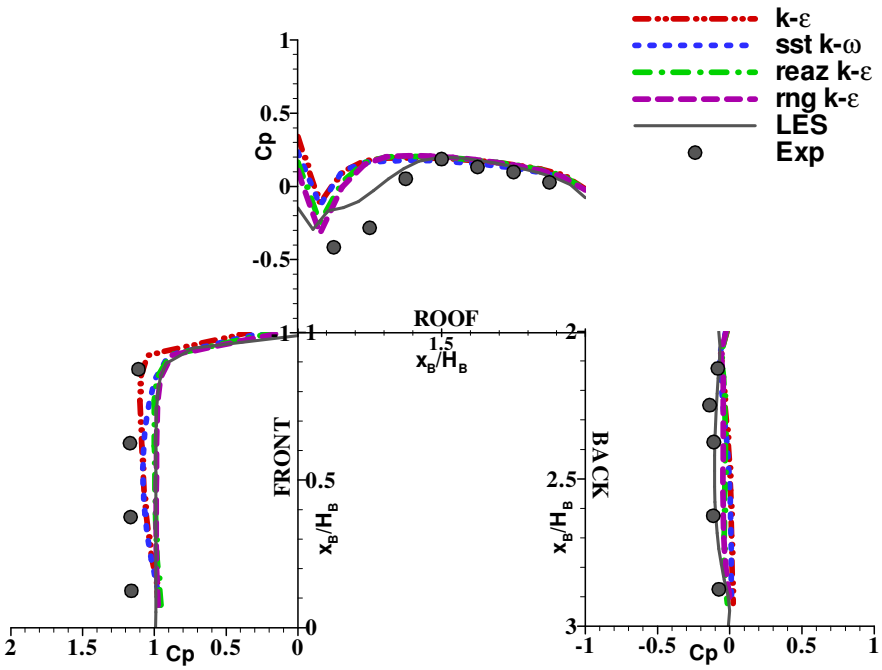

(c)

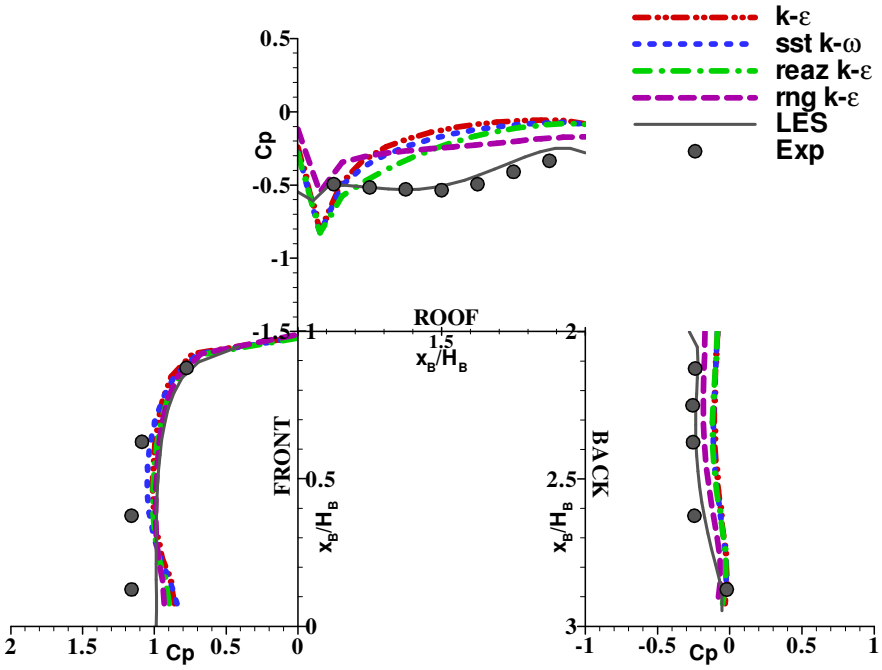

(d)

Figure 7: Comparison of Numerical and Experimental Pressure Coefficients for B2 at different locations from the center of the jet

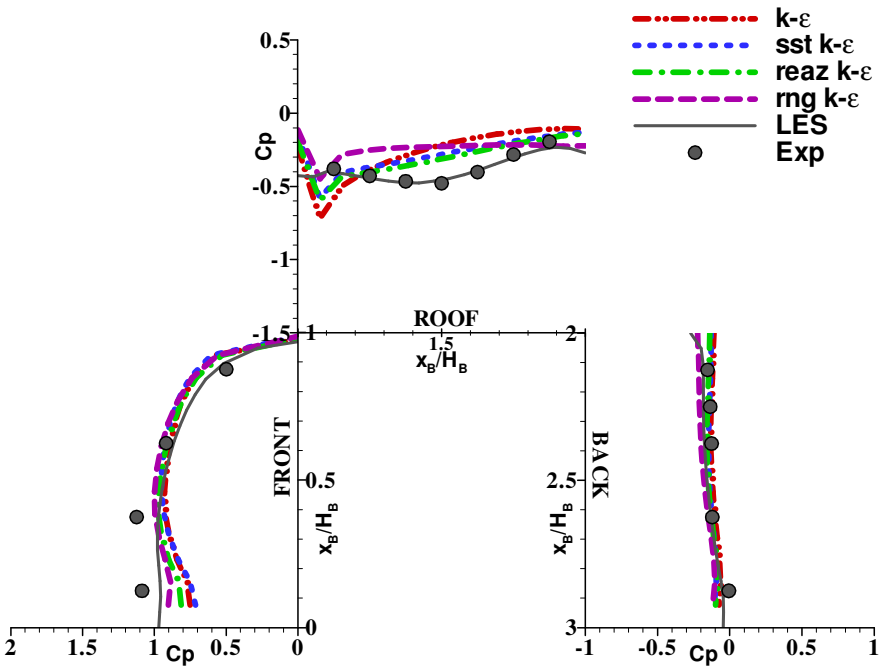

(e)

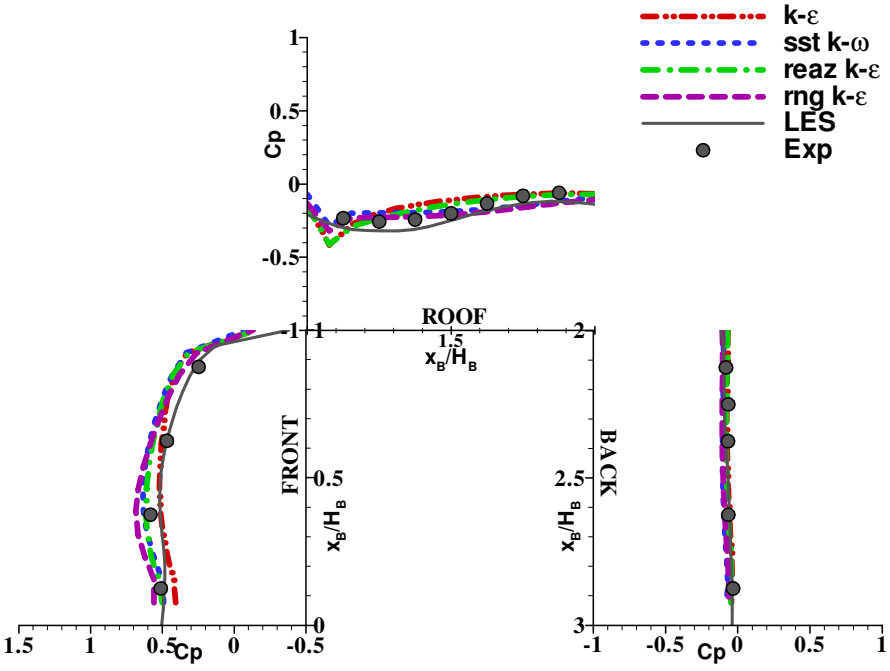

(f)

Figure 7: Comparison of Numerical and Experimental Pressure Coefficients for B2 at different locations from the center of the jet

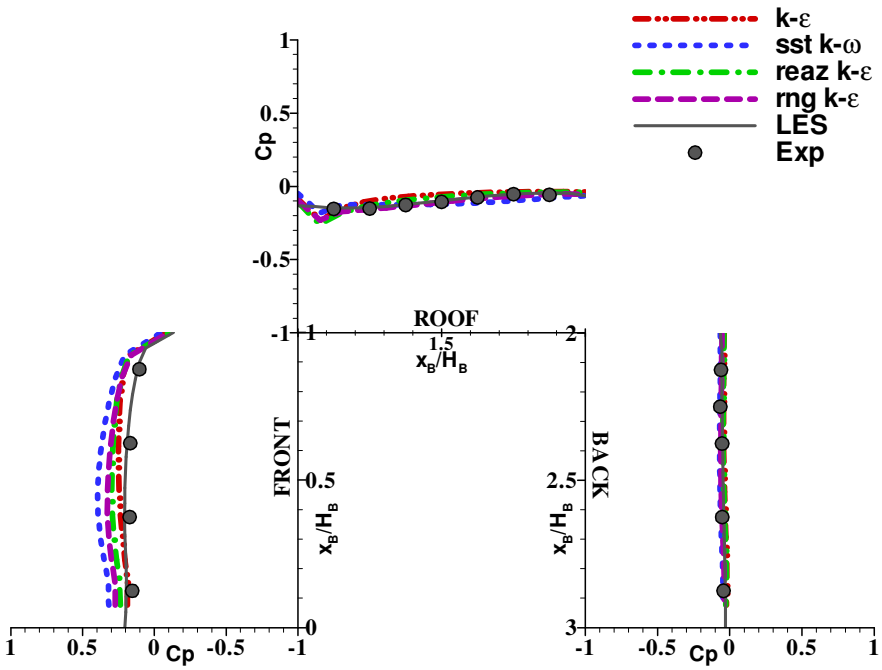

(g)

Figure 7: Comparison of Numerical and Experimental Pressure Coefficients for B2 at different locations from the center of the jet
(a) 0D (b) 0.5D (c) 0.75D (d) 1.0D (e) 1.25D (f) 2.0D (g) 3.0D

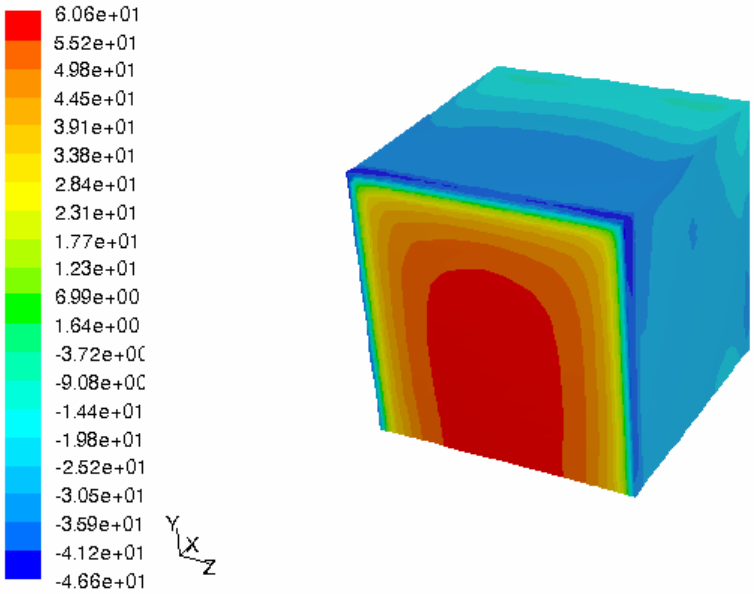

(a)

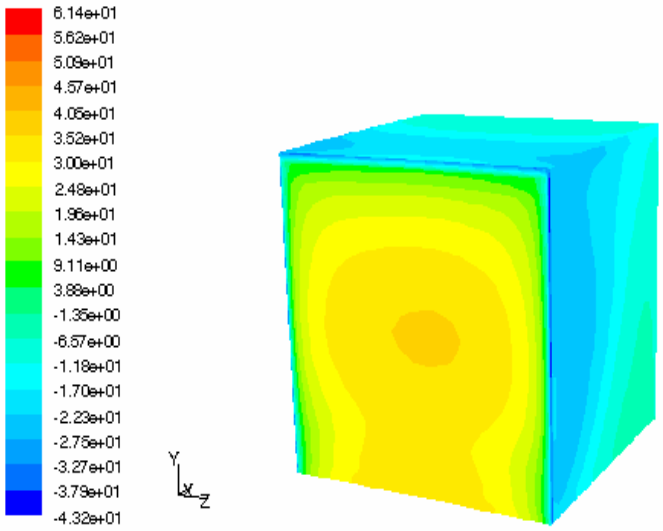

(b)

Figure 8: Frontal face pressure distribution for B2 at locations
(a) 1.0D (b) 2.0D

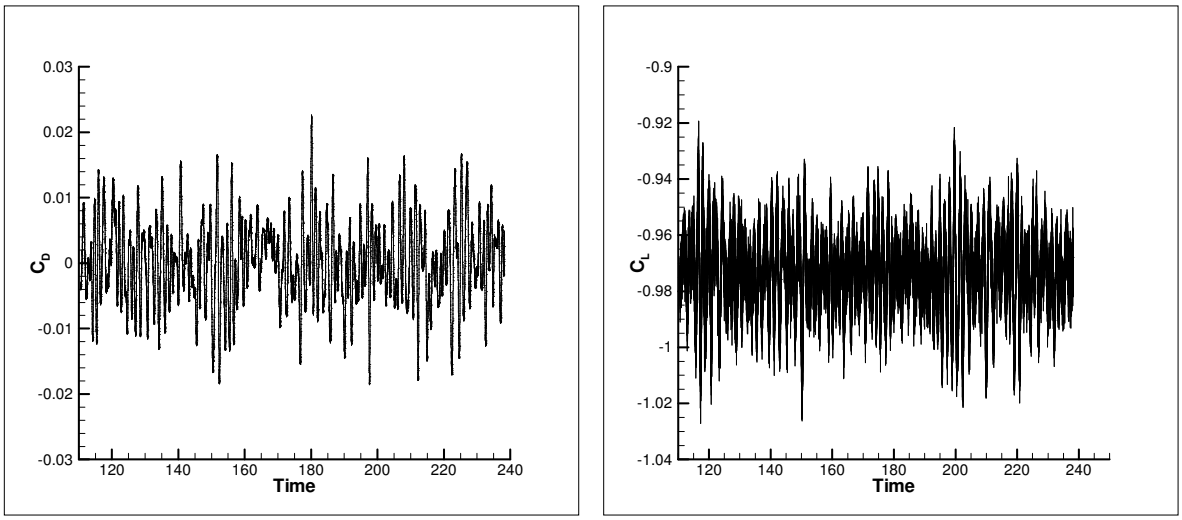

(a)

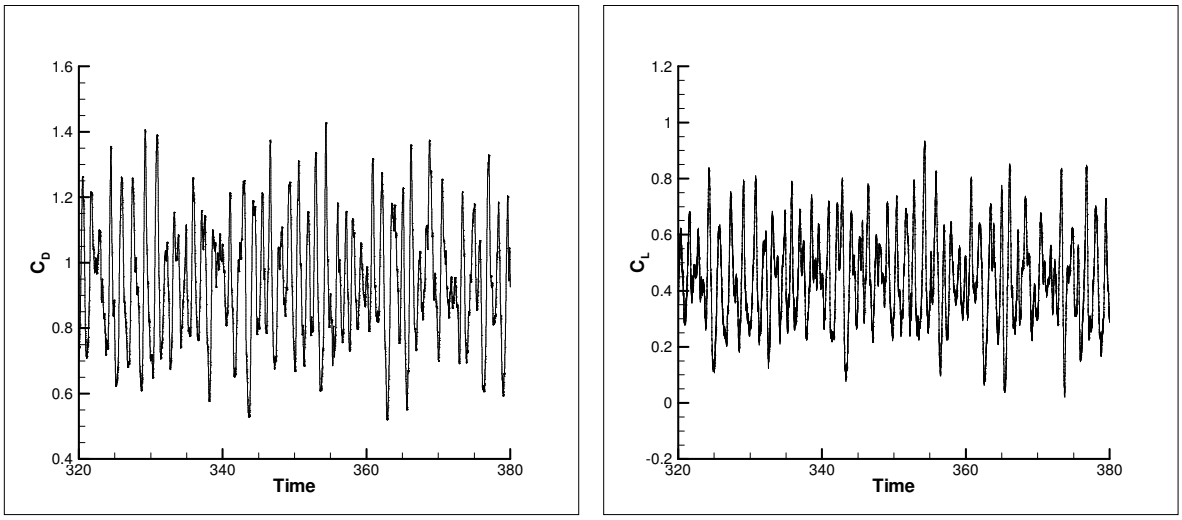

(b)

Figure 9: Numerical Drag/Lift versus time curve
(a) building at 0D (b) building at 1.0D

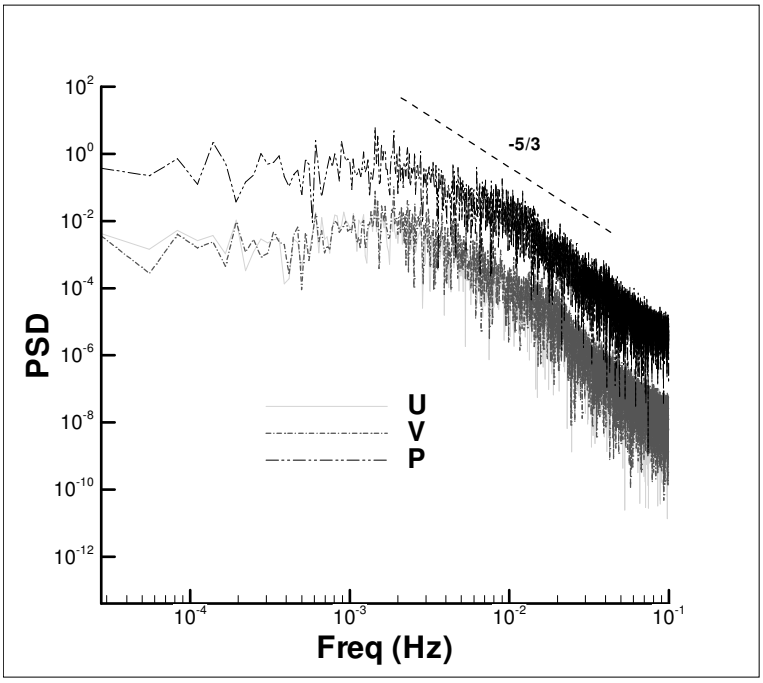

(a)

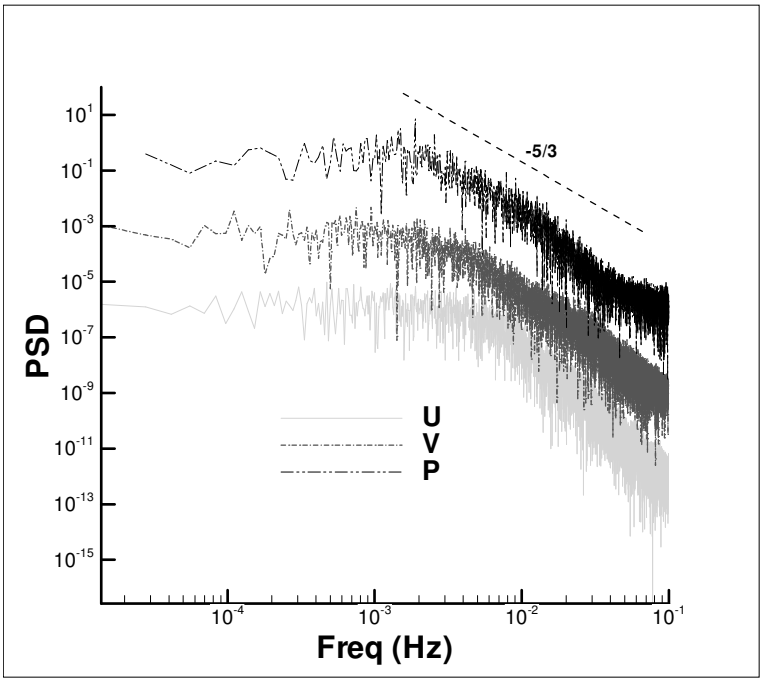

(b)

Figure 10: Spectra plots of U and V Velocity and Pressure for building at 1D
(a) Roof of the building (b) Back of Building

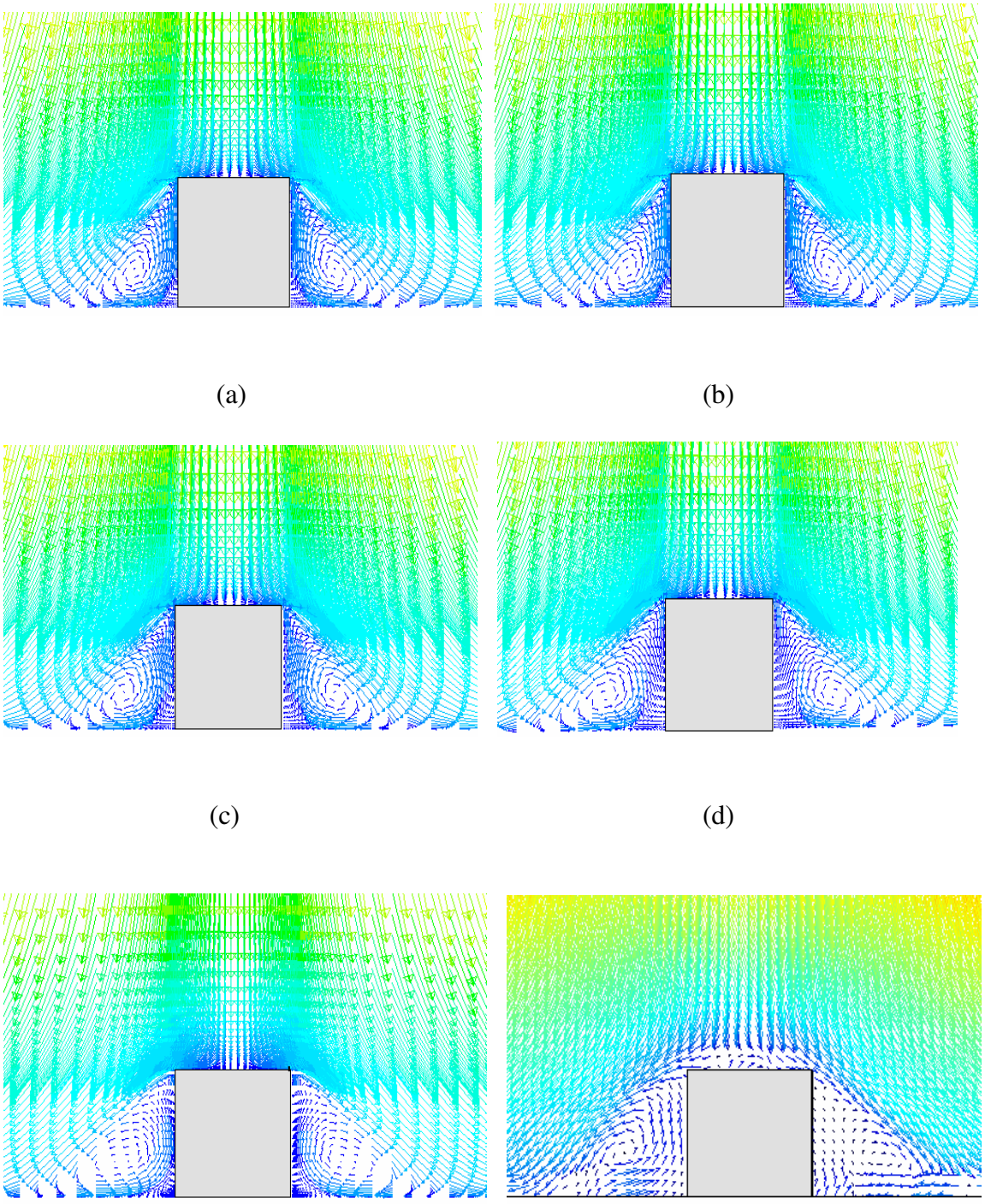

(a) (b)

(c) (d)

(e) (f)

Figure 11: Comparison of mean velocity vectors for building B2 at 0 D
(a) standard k-ε (b) SST k-ω (c) Reaz k-ε (d) RNG k-ε (e) LES (f) Exp (PIV)

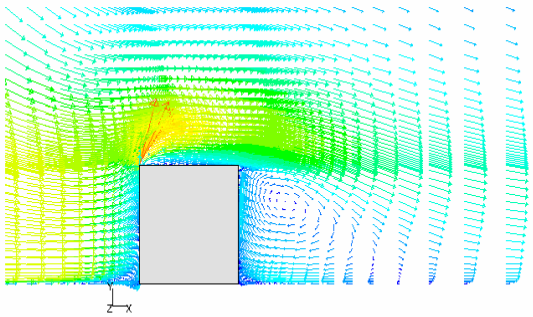

(a)

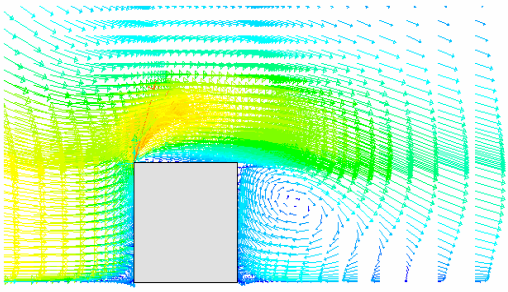

(b)

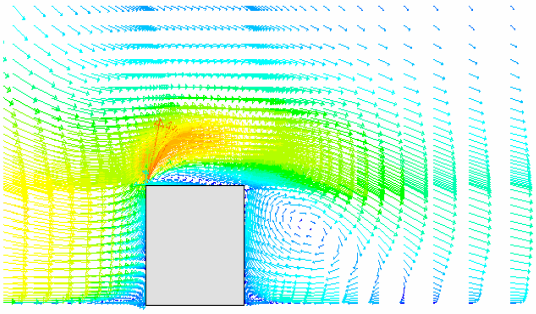

(c)

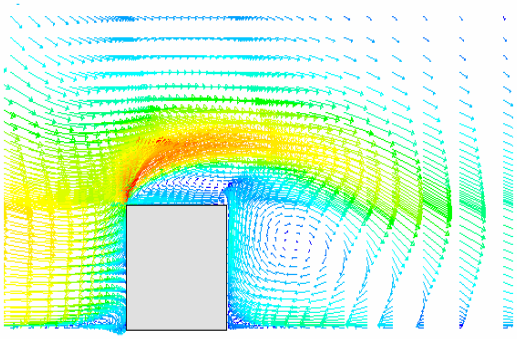

(d)

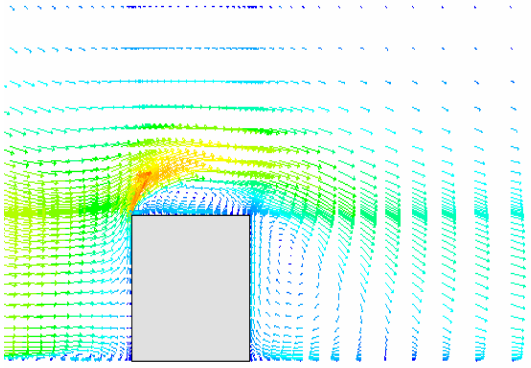

(e)

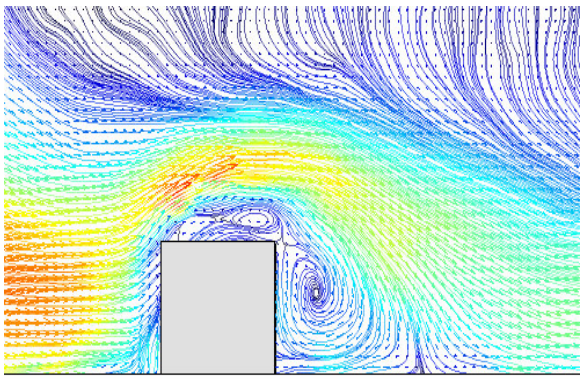

(f)

Figure 12: Comparison of mean velocity vectors for building B2 at 1.0 D
(a) standard k-ε (b) SST k-ω (c) Reaz k-ε (d) RNG k-ε (e) LES (f) Exp (PIV)

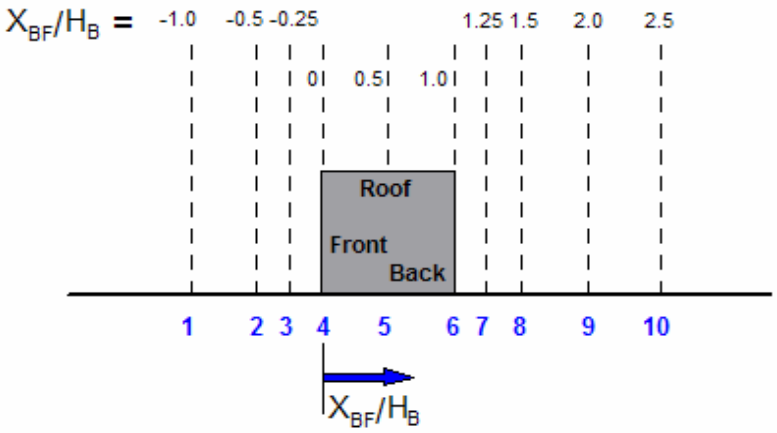

(a)

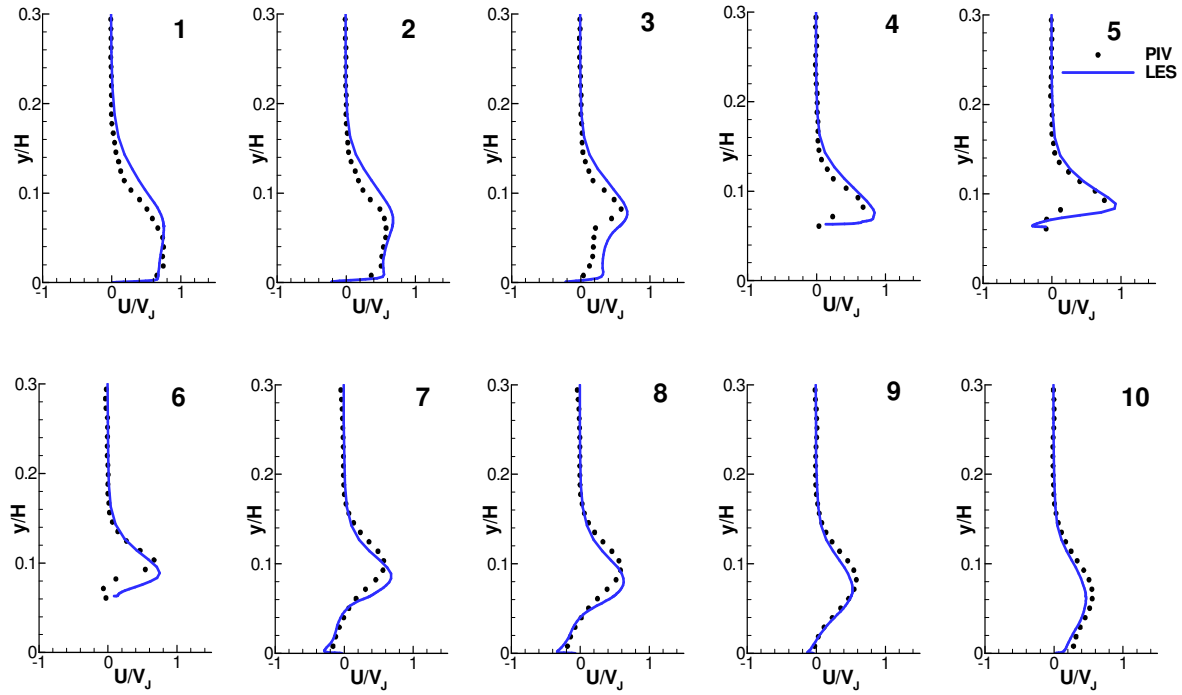

(b)

Figure 13: Comparison of Mean velocity profiles, LES and PIV
(a) Profile locations (b) Normalized Mean U velocity at 1.0D

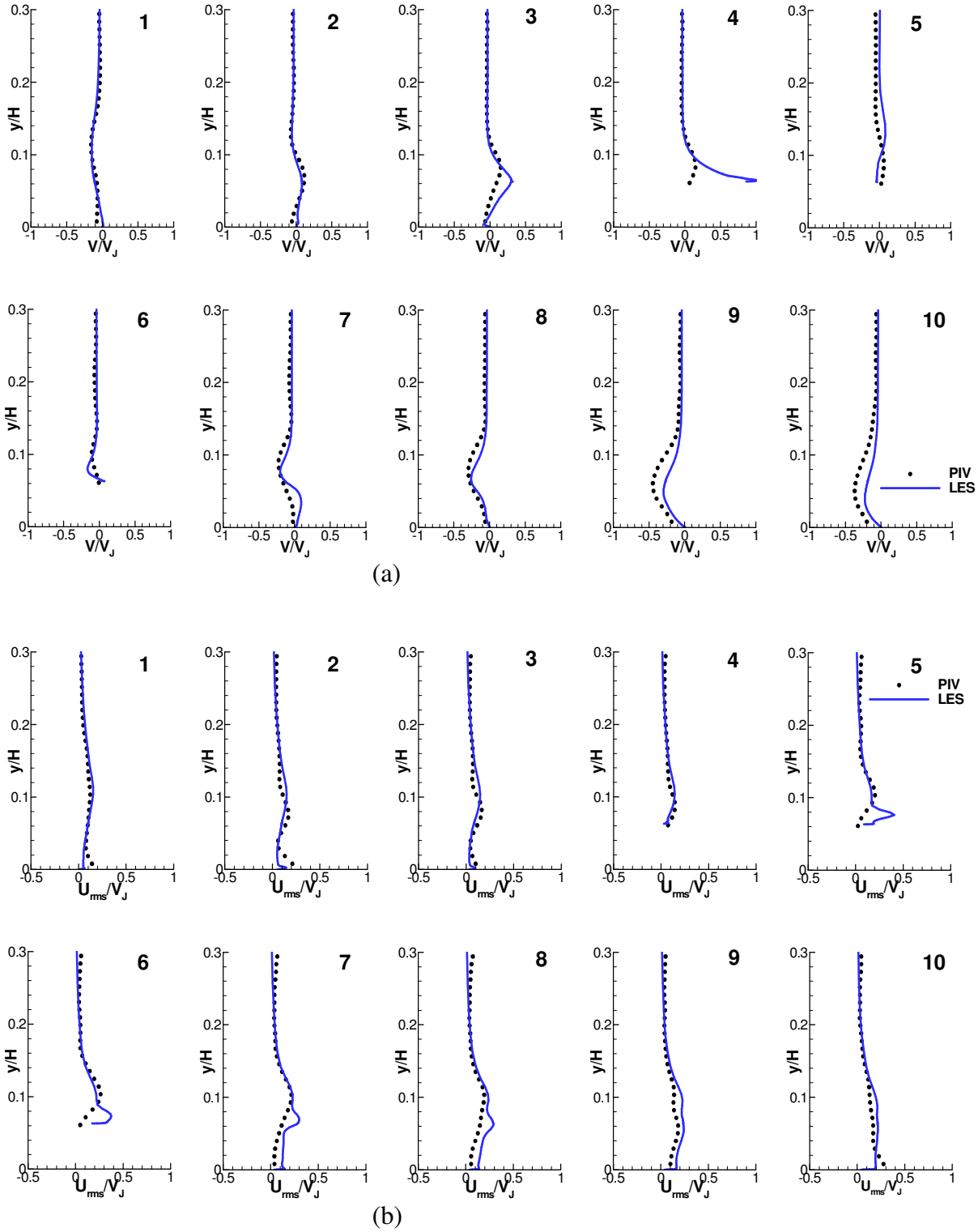

Figure 14: Comparison of Mean velocity profiles, LES and PIV at 1D
(a) Normalized Mean V velocity (b) Normalized U_{rms} velocity profiles

CHAPTER 4

LARGE EDDY SIMULATION OF MOVING IMPINGING JETS OVER A CUBE: APPLICATION TO MODELING A TRANSLATING MICROBURST AND ITS AERODYNAMIC LOADING EFFECTS ON BUILDINGS

A paper to be submitted to the Journal of Engineering Structures

Anindya Sengupta [1, 2] and Partha P. Sarkar[1, 3]

Abstract:

This paper reports the numerical simulation of a moving jet and its effects on a cube shaped building. The simulation replicates a translating microburst that occurs in nature. The effects of wind loads resulting from a translating microburst on a building model were studied. Large eddy and RANS simulations were conducted for four different translating speeds of the microburst. The results of the simulation for the lowest speed setting are compared with those obtained in the laboratory. The microburst is modeled as a round jet, impinging onto a flat plate. The resulting loads on the building models for static and moving impinging jets are compared, with emphasis on peak loads experienced by the building.

Keywords: Translating microburst; Moving impinging jet; LES; Peak wind loads; Fluid-structure interaction

[1] Graduate Student and Professor respectively, Department of Aerospace Engineering, Iowa State University
[2] Primary Researcher and author
[3] Author for correspondence

1. Introduction

The current research focuses on the simulation of a traveling microburst (Fujita, 1985) using both experimental and numerical methods. In the laboratory, the microburst is modeled as a jet coming out of a circular duct and impinging on a wooden platform placed below. This facility consists of a wooden surface on an adjustable base mounted perpendicular to a round jet nozzle with a 3:1 area contraction ratio. A small centrifugal fan that supplies the air flow is mounted on top of the nozzle. The nozzle could be translated at a constant speed using a garage door opener. The jet to surface height can be varied from 203 mm (8") to 826 mm (32.5"). The jet was operated at two different velocities, 10 m/s and 16 m/s, resulting in a Reynolds number of 1.4×10^5 and 2.2×10^5, respectively, based on the diameter of the jet exit nozzle (203 mm or 8 in.). Two cubic building models (B1: 12.7 mm and B2: 25.4 mm) were tested. The current paper focuses on the 25.4 mm cubic building or B2 only. Digital pressure transducers were used to measure the pressures on the ground plane as well as on the building models.

Large Eddy Simulation (LES) was used to simulate the translating microburst phenomenon and study the pressure field characteristics on buildings. The RANS turbulence model, realizable k-ε model was also tested to see how well it compared to both the experimental as well as LES data.

In reality, the microburst is a very short-term phenomenon and usually translates horizontally due to the motion of the parent cloud. A ring vortex has been observed to form in a microburst as the leading edge of the downdraft interacts with the ground and the flow spreads outwards. The horizontally translating ring vortex in a stationary or moving microburst is expected to produce dynamic effects on the velocity profiles. Lundgren et al.

(1992), Yao and Lundgren (1996) and Alahyari and Longmire (1995) have conducted several laboratory experiments using fluids of different density to study the effects of downburst on aircrafts in flight for the aircraft industry and were able to incorporate the effect of buoyancy in their simulation and produce a ring vortex. Orf and Anderson (1998) studied the effects of traveling and colliding microbursts, through numerical study from a meteorological view. The only work that relates to effects of a moving microburst on a building was reported by Letchford and Chay (2002). They manually moved an inverted impinging jet at various speeds to study the drag and lift forces on a cube. The main motivation of the current paper is to simulate translating microbursts using numerical simulation. As it might not be physically possible to produce translation speeds higher than a certain limit due to lack of experimental infrastructure and cost limitations, it is now possible to do so using numerical simulation with the quantum increase in the power of desktop computing. Recently research work in this area was reported by Sengupta et. al (2006) and Sengupta and Sarkar (2007).

Jet impingement is a technique for enhancing heat transfer that is used in a variety of applications ranging from electronic cooling to flow through gas turbines. Jet impingement on moving surfaces has been simulated, both experimentally and numerically, by a few researchers. Chattopadhyay and Saha (2003) used LES to study the flow and heat transfer due to a slot jet impinging on a moving plate. Recently, Senter and Collic (2007) studied the flow field due to a turbulent slot jet impinging on a moving surface using PIV. In all the research work mentioned above, the impinging jet was kept fixed and the impingement surface was moved at specific speeds. Moving impinging jet has been used to simulate spray painting for automotive purposes by Ye (2005).

The primary objectives of the present work were: (a) to perform laboratory simulation of a moving microburst using an impinging jet to study the transient pressure characteristics its distribution on a cube-shaped building, (b) to apply CFD to simulate the moving microburst phenomenon with jet impingement using different turbulence models, (c) to compare and validate the CFD results with those of the experiments, and (d) to apply CFD to numerically predict the effects of different translating speeds of a microburst on wind loads on a cubic building. The effects of the magnitude of the jet velocity ratio V_{TR}, defined as the ratio of the jet translating speed (V_T) to jet exit speed (V_J), on the wind loads on the cubic building is studied.

2. Experimental Setup

The experimental setup is shown in Figure 1. A nozzle diameter (D) of 203 mm (8 in.) was used to produce the jet. The nozzle could be translated using a garage door opener, which allowed the jet to move at a maximum speed of 0.225 m/s. The distance (H) of the ground plane or impinging platform (L = 2.44 m (96 in.) and B = 1.22 m (48 in.) from the nozzle could be varied from a minimum of 203 mm (8 in.) to a maximum of 826 mm (32.5 in.) using a mechanical jack. A honeycomb and two screens were used to reduce the turbulence of the issuing jet. A 3:1 area contraction was used at the nozzle end to make the velocity of the issuing jet uniform. For the current work, H = 206 mm (8.125 in.), H/D = 1.02; H = 403 mm (15.875 in.), H/D = 1.98; and H = 587 mm (23.25 in.), H/D = 2.91 were used. Henceforth, these three heights are termed as H1, H2 and H3, respectively. The H/D ratio for this study was chosen to be within the range of H/D values of a microburst that varies between 0.75 and 7.5. Two jet velocities were used, $V_j \approx 10$ m/s (32.8 ft/s) and $V_j \approx$

16 m/s (52.5 ft/s). Henceforth, these two velocities are termed as V1 and V2, respectively. This resulted in a Reynolds number of 1.4 x 10^5 and 2.2 x 10^5, respectively, based on the diameter of the jet exit nozzle (D). The current paper discusses the results for H2 and V1 only.

2.1 Static and Fluctuating Pressure Measurement

The ground plane was made of plywood with numerous pressure ports drilled onto it for measuring the pressures on the ground due to both static and moving microburst. A schematic arrangement of ground pressure taps is shown in Figure 2a. For the building model, a wooden cube was used with sides 25.4 mm (1.0 in). 7 pressure taps were drilled on each side of the cube along its centerline. Building model showing pressure tap locations is shown in Figure 2b, with the numbers indicating the taps that were actually used to collect data. A total of 16 pressure taps were used for the *static jet* case, 4 on the front side, 7 on the roof and 5 on the back side. For the case of the translating jet, 14 pressure taps were used. Tap numbers 15 and 16 were not used to measure the roof and backside pressures for the *translating jet* case.

In the absence of a triggering mechanism, a simple but innovative solution was developed to stamp the starting and stopping times of the pressure records for the translating jet case. One pressure tap each was placed directly under the exit nozzle both at the starting (tap 17 and stopping (tap 18) locations of the nozzle (Figure 1). They were placed in such a way that the first one will stop recording any dynamic pressure as soon as the jet starts translating. The second one was located in such a way such that it will start recording the dynamic pressure when the jet just stops translating after covering the required distance. This arrangement helped in determining exactly the starting and stopping time for the translating jet. The jet

translated with a constant velocity and the error in the translating speed was found be less than 1%. A schematic diagram for this arrangement is shown in Figure 1. Figure 3 plots the raw pressure tap data readings showing the effectiveness of this setup to accurately measure the starting and stopping time of the jet. A 16-channel Scanivalve pressure transducer (Digital Sensor Array or DSA 3217) was used for measuring both the static and fluctuating pressures on the ground surface as well as those on the building models.

3. Numerical Simulation

As found from the previous studies, Realizable k-ε model performed best in terms of results as well as computational speed; we have used this RANS model for translating jet simulation. The RNG k-ε model was also used, and as it gave results very similar to the Realizable k-ε model, those results are not presented in this paper.

3.1 Realizable k-ε Model

In this model the transport equations are given as follows:

$$\frac{\partial}{\partial t}(\rho k)+\frac{\partial}{\partial x_i}(\rho k u_j)=\frac{\partial}{\partial x_i}\left[\left(\mu+\frac{\mu_t}{\sigma_k}\right)\frac{\partial k}{\partial x_j}\right]+G_k+G_b-\rho\varepsilon-Y_M+S_k \quad (1)$$

$$\frac{\partial}{\partial t}(\rho \varepsilon)+\frac{\partial}{\partial x_j}(\rho \varepsilon u_j)=\frac{\partial}{\partial x_j}\left[\left(\mu+\frac{\mu_t}{\sigma_\varepsilon}\right)\frac{\partial \varepsilon}{\partial x_j}\right]+\rho C_1 S_\varepsilon-\rho C_2\frac{\varepsilon^2}{k+\sqrt{\nu\varepsilon}}+C_{1\varepsilon}\frac{\varepsilon}{k}C_{3\varepsilon}G_b+S_\varepsilon \quad (2)$$

$$\text{Here } C_1=\max\left[0.43,\frac{\eta}{\eta+5}\right] \text{ and } \quad \eta=S\frac{k}{\varepsilon}$$

The model constants for the realizable k–ε model are given by: $C_{1\varepsilon}$ = 1.44, C_2 = 1.68, σ_k = 1.0 and σ_ε = 1.2. C_μ is no longer a constant in this model. More details about this model can be found in Fluent (2005).

3.2 Large Eddy Simulation (LES)

In LES the velocity field is separated into two distinct parts, namely the resolved part ($\bar{u}_i$) which represents the larger scales or eddies and the subgrid (or modeled) part (u_i') which represents the smaller scales. We need to include the effect of these small scales on the resolved field through the use of a subgrid-scale model. To separate the large scales from the small scales, a filtering operation is performed. A filtered variable is defined as

$$\bar{f}(x) = \int_D f(x')G(x-x')dx' \tag{3}$$

where D is the entire flow domain and G is the filter function which determines the size and structure of the small scales which requires modeling. For a top hat filter in real space,

$$G(x-x') = \begin{cases} 1/\Delta, & |x-x'| \le \Delta/2 \\ 0, & otherwise \end{cases} \tag{4}$$

where $\Delta = (\Delta_1\Delta_2\Delta_3)^{1/3}$. Applying the filtering operation, we get the following equations for continuity and momentum for an incompressible flow;

$$\frac{\partial \bar{u}_i}{\partial x_i} = 0 \tag{5}$$

$$\frac{\partial \bar{u}_i}{\partial t} + \frac{\partial \bar{u}_i \bar{u}_j}{\partial x_j} = -\frac{1}{\rho}\frac{\partial \bar{p}}{\partial x_i} - \frac{\partial \tau_{ij}}{\partial x_j} + \nu \frac{\partial^2 \bar{u}_i}{\partial x_j \partial x_j} \tag{6}$$

The term τ_{ij} called the subgrid scale (SGS) stress is given by

$$\tau_{ij} = \overline{u_i u_j} - \bar{u}_i \bar{u}_j \tag{7}$$

The role of the SGS stress is to remove energy from the large or resolved scales. The subgrid-scale stresses resulting from the filtering operation requires modeling. The subgrid-scale turbulent stresses are computed using the eddy-viscosity model:

$$\tau_{ij} - \frac{1}{3}\tau_{kk}\delta_{ij} = -2C\Delta^2 \left|\overline{S}\right| \overline{S}_{ij} \tag{8}$$

Here $C = C_S^2$, $\left|\overline{S}\right| = \sqrt{2\overline{S}_{ij}\overline{S}_{ij}}$ and $\overline{S}_{ij}$ is the rate-of-strain tensor for the resolved scale defined by

$$\overline{S}_{ij} \equiv \frac{1}{2}\left(\frac{\partial \overline{u}_i}{\partial x_j} + \frac{\partial \overline{u}_j}{\partial x_i}\right) \tag{9}$$

In the dynamic SGS model (Germano et al. (1991), two different filters are applied. In addition to the grid filter G (Δ), a test filter $\hat{G}$ ($\hat{\Delta}$) is also applied. In general the test filter is larger than the grid filter and usually $\hat{\Delta}$ = 2Δ. Applying both the filters to the NS equation results in;

$$\frac{\partial \hat{\overline{u}}_i}{\partial t} + \frac{\partial \hat{\overline{u}}_i \hat{\overline{u}}_j}{\partial x_j} = -\frac{1}{\rho}\frac{\partial \hat{\overline{p}}}{\partial x_i} - \frac{\partial T_{ij}}{\partial x_j} + \nu \frac{\partial^2 \hat{\overline{u}}_i}{\partial x_j \partial x_j} \tag{10}$$

The above filtering result in subtest-scale stresses (as in equation 7)

$$T_{ij} = \widehat{\overline{u_i u_j}} - \hat{\overline{u}}_i \hat{\overline{u}}_j \tag{11}$$

Applying the test filter to the grid filtered equation (Eq.6) results in

$$\frac{\partial \hat{\overline{u}}_i}{\partial t} + \frac{\partial \hat{\overline{u}}_i \hat{\overline{u}}_j}{\partial x_j} = -\frac{1}{\rho}\frac{\partial \hat{\overline{p}}}{\partial x_i} - \frac{\partial \hat{\tau}_{ij}}{\partial x_j} + \nu \frac{\partial^2 \hat{\overline{u}}_i}{\partial x_j \partial x_j} - \frac{\partial L_{ij}}{\partial x_j} \tag{12}$$

Here the dynamic Leonard stresses L_{ij} is defined as

$$L_{ij} = \widehat{\overline{u}_i \overline{u}_j} - \hat{\overline{u}}_i \hat{\overline{u}}_j = T_{ij} - \hat{\tau}_{ij} \tag{13}$$

Assuming the same functional form for T_{ij} as in equation 8, we get

$$T_{ij} - \frac{1}{3}T_{kk}\delta_{ij} = -2C\hat{\Delta}^2 \left|\hat{\overline{S}}\right| \hat{\overline{S}}_{ij} \tag{14}$$

Substituting equation 8 and 14 into the expression for L_{ij} in equation 13, we get

$$L_{ij} - \frac{1}{3}\delta_{ij}L_{kk} = -2C(\hat{\Delta}^2 \left|\hat{\bar{S}}\right| \hat{\bar{S}}_{ij} - \Delta^2 \widehat{\left|\bar{S}\right| \bar{S}_{ij}}) \tag{15}$$

Using $M_{ij} = (\hat{\Delta}^2 \left|\hat{\bar{S}}\right| \hat{\bar{S}}_{ij} - \Delta^2 \widehat{\left|\bar{S}\right| \bar{S}_{ij}})$, the error $Q = (L_{ij} - \frac{1}{3}\delta_{ij}L_{kk} - 2CM_{ij})^2$ is minimized using a least squares minimization suggested by Lilly (1992) using the relationship $\frac{\partial Q}{\partial C} = 0$ giving

$$C = -\frac{1}{2}\frac{L_{ij}M_{ij}}{M_{ij}M_{ij}} \tag{16}$$

Here $C = C(x_i, t)$ i.e. a function of both space and time. To avoid numerical instability, the value of C is clipped at zero. More details about LES model can be found in Fluent (2005).

3.3. Numerical Simulation of Moving Jet

To model the moving microburst and compute the unsteady flow field and its effects on the building model, both a sliding mesh model as well as the dynamic mesh model were used [Fluent 2005]. In the sliding mesh technique, the whole numerical domain is divided into two separate zones. Zone one consisted of the building model with the surrounding box shaped domain. Zone two included the nozzle through which the air jet exits. The cells of both of these two zones are bounded by an interface zone. The two interface zones form a grid interface. The cells of the nozzle zone move at designated speeds relative to the static zone one along this grid interface. Node alignment along the grid interface is not required, but for a stable solution a fine mesh is required. In this method there is no cell distortion due to the motion. The sliding mesh technique is routinely used to simulate the relative motion of two trains or vehicles passing each other.

In the dynamic mesh method, the whole computational domain is again decomposed into two distinct zones as before. But in this case the nozzle is embedded in the dynamic or

moving zone and the cells are distorted due to the motion of the nozzle. Too much cell distortion can lead to instability of the solution procedure. The layering method was used where the cells are created or destroyed based on predefined split and collapse factors. For both the sliding and dynamic procedure, a non-conformal mesh interface was needed. More details about these two techniques can be found in Fluent [2005]. The nozzle was translated for a total distance of 6D, i.e., for $-3.0 \leq x/D \leq 3.0$, though in some cases to decrease the computational time, it was translated between the range $-2.5 \leq x/D \leq 2.5$ for a total distance of 5D. The dynamic mesh motion is used mainly to simulate the flow in reciprocating IC engines as well as automobile overtaking phenomenon, Clark and Filippone (2007).

3.4 Numerical Simulation Parameters

For the numerical simulations, the air density was taken as 1.225 kg/m^3 and air viscosity as 1.7894 E-05 Ns/m^2. The inlet values of turbulence intensities were substituted from the experimental data. For all the RANS models, the QUICK scheme was used for the convective fluxes as this reduces the numerical diffusion, and 2nd Order schemes for k and ε terms were chosen. The SIMPLE algorithm was used for the pressure correction for static jet simulations. For the moving jet simulations, both the SIMPLEC and PISO schemes were used. The simulations using these two schemes were closer to experimental values and also it provided a more stable solution. No appreciable difference in results was found using either of these two schemes.

Enhanced wall treatment was adopted for RANS simulation and a fine mesh was used near the walls to ensure a mean $y^+ \approx 1$ for the region near the ground and the building faces. For all RANS simulations, fully converged solutions were obtained after setting the residual

errors for all the variables to be less than $1x10^{-6}$, except for continuity it was set less than $1x10^{-8}$.

In case of static jet simulation using LES, the Fractional Step Method (FSM) was used for pressure-velocity coupling. This non-iterative (NITA) scheme uses much less computation time compared to the iterative (ITA) schemes. For the moving jet simulations, the ITA scheme as well PISO pressure-velocity coupling algorithm were used for reasons of stability as the FSM method was highly unstable, particularly for the higher jet translation speeds.

Initially, LES simulations for the static jet case were performed using the both the constant Smagorinsky [Fluent 2005] and dynamic Smagorinsky-Lily [Fluent 2005] model. It was seen that the results of the dynamic model matched the experimental data better, and henceforth all the simulations (both static jet and translating jet) were conducted using the dynamic model only.

For LES, a bounded central difference scheme was used for the convective terms and an implicit scheme was chosen for temporal discretization. The jet nozzle was moved at four different speeds, 0.225 m/s (S1; V_{TR} = 0.0225), 0.5 m/s (S2; V_{TR} = 0.05), 1 m/s (S3; V_{TR} = 0.1) and 2 m/s (S4; V_{TR} = 0.2) using both the sliding mesh and dynamic mesh simulation methods.

The simulations were carried out using Fluent [2005] in our computational laboratory consisting of PCs with 2GB of RAM and using dual CPU Intel Xeon processors running Red Hat Linux OS. The validity of the numerical simulation was checked using different domain and grid sizes as well as time steps (unsteady case only). For the simulation results presented

here, the RANS model for the static jet case consisted of approximately 1.1 million cells (half model). For the static jet LES simulations, 1.4 to 2.0 million cells were used depending on the location of the jet and about 2 million cells were used for the moving jet LES simulations. The same mesh for the moving jet LES simulations were used for the moving jet RANS simulations. Grid stretching and clustering near the walls helped to achieve a mean y+ value of 1 for the ground plane wall and the building walls. Another AMD dual CPU Opteron 64 bit machine was available which helped to validate the LES simulations for the translating jet case using about 2.8 million cells. Figure 4 shows boundary conditions adopted for the moving jet simulation. Figure 4 shows the grid used for the moving jet simulation using the dynamic mesh method.

4. Results and Discussion

The result of the static jet without the building model is plotted first. In Figure 5a, the ground pressure distribution is shown when the jet is directly on top of the center tap, P0 (refer Fig. 2a). A typical bell shaped curve is seen. It can also be seen that there is good agreement between numerical and experimental results.

The pressure coefficient C_p was normalized with the jet exit velocity V_J. Here C_P is defined as:

$$C_p = \frac{(P - P_S)}{0.5\rho V_j^2} \tag{17}$$

The translating jet results are discussed now. First, the results for the case of a moving impinging jet are discussed without any building model on the ground surface. Then the

results of the moving impinging jet with a building model are discussed, where experimental and numerical results are compared and analyzed.

The effects of the moving jet on the ground surface pressures without any obstacle was tested in the laboratory for three different jet heights, H1, H2 and H3, respectively. The experimental data for jet height H2 are only presented along with the corresponding numerical results. For the experimental setup, the maximum speed achieved by the translating impinging jet was 0.225 m/s (S1). Though other translation speeds that were lower than this speed were also tested, the results for these speeds are not presented here since these do not differ much.

The pressure coefficients for a point P0 on the centerline of the traveling jet axis are plotted in Figure 5b. The experimental and numerical results at the lowest speed setting (S1:0.225 m/s) are in close agreement. The experimental data shows that the maximum value of Cp occurs when the jet is directly over point P0. As the jet is moving very slowly, it is seen that not much difference occurs between the results for the static and moving jets. The comparison with both LES and realizable k-ε model is very good, though it can be seen that the RANS model is unable to capture the fluctuation of C_P. LES is able to reproduce these with greater accuracy when compared to the experimental data. Figure 6 plots the results for speeds S3 (1 m/s) and S4 (2 m/s). It can be seen from the computed pressure distribution at P0 for higher speeds that though RANS is able to capture the mean pressure distribution profile, it is again not able to predict the pressure fluctuations which occurs in reality. The entire distribution of the ground pressure on either sides of the traveling impinging jet is plotted. Comparison of numerical (LES) results with experimental data in Figure 7a shows excellent agreement. Figure 8b shows the ground pressures for higher speed

S4. The results do not exactly match Fujita's (1985) hypothesis as shown in Figure 8a. The fluctuating velocities are plotted using the LES results. The velocity fluctuations were measured at two locations above point P0, at $0.5H_B$ and H_B, respectively. In Figure 9, it can be seen that the velocity in the x direction (U) is higher at lower heights; due to the shallow depth of the wall jet formed after impingement and also that these velocities increase with increased jet translation velocity. The effects of these higher velocities are explained when the peak loads on the cube are discussed later.

In Figure 10a, the wind speeds measured at the Andrews Air Force Base (AFB) [Fujita, 1985] are shown. To make a comparison of this field data with the LES simulation, the horizontal velocity (magnitude only) at a height of $0.5H_B$ from the ground plane and corresponding to a translating speed of S4 is also plotted as in Figure 10b. The time axis in Figure 10b is plotted in the reverse direction to match Figure 10a. The ratio between the front-side peak velocity to the back-side peak velocity from AFB was calculated as 1.55 and was found to be comparable to 1.46 as determined from the LES simulation. The velocity scale (field versus model) was calculated as 3.52 from the front-side peak velocities of the AFB field and the numerical data.. The time scale (field versus model) was determined as 736 by comparing the time intervals between the two peak velocities (front-side and back-side peaks) as in the field and numerical data. A length scale can be calculated as 2591 or roughly 2600 from these estimated velocity and time scales. This means that the diameter of the microburst that was simulated in this work was 528 m and the equivalent dimension of the cubic building (B2) that was tested was 66 m (medium-rise building). Based on the equations derived for the horizontal velocity profile (chapter 2), U_m and b as a function of r/D, it means that the maximum horizontal wind (U_m) that occurs at r/D of 0.9 from the

center of the microburst possibly occurred at 0.02D or about 11 m elevation from the ground (b = 0.13D at this location) in the AFB case. This has implication with regards to the design of one- two- or three-story residential and commercial buildings.

The basis of putting more emphasis on using LES compared to the RANS models was justified after studying the effects of the static jet on the building model at various distances from the jet center. The pressure distribution along the centerline of the cube at two different distances from the center of the jet is shown in Figure 11. It can be seen that out of all the turbulence models used (k-ε, k-ω, reaz k-ε, rng k-ε), only LES was able to predict the pressure distribution on the roof at these two building locations where there was significant flow separation on the roof.

In this paper, C_D and C_L are defined as

$$C_D = \frac{Fx}{0.5\rho V_J^2 A_R} \tag{18}$$

$$C_L = \frac{Fy}{0.5\rho V_J^2 A_F} \tag{19}$$

Here Fx and Fy are the forces in the x and y directions, respectively. A_R is the roof area of the cube and A_F (=A_R) is the frontal area of the cubic model.

Initially, the time and mesh resolutions were studied. It was noticed that higher speeds needed smaller time steps, otherwise the solution blew up. The time steps used (non-dimensionalized by $\frac{\Delta t * V_J}{D_J}$) are given in Table 2. The mesh sizes used are also given in Table 2. Figure 12 shows the effects of time step reduction on the results of S4 using LES and dynamic mesh simulation. Smaller time steps leads to better results, especially for higher translating speeds and also increases the stability of the solution. As both the sliding and

dynamic mesh methods were used, a comparison of the drag and lift for S4 obtained with both of these methods is plotted in Figure 13. It can be seen that these two methods produce slightly different results under identical conditions of mesh and time step size, though the trend is similar. The effect of mesh size is seen next by comparing the results for S4 in Figure 14. Here the results for the dynamic mesh are compared.

Figure 15 presents results of the translating microburst at the lowest speed setting (S1). It can be seen that CFD (LES) is able to predict both the drag and lift coefficients on the cubic building with remarkable accuracy. It can also be seen that in a microburst, a significant downward force occurs on the roof when the microburst is at a position close to the top of the building which is not considered in current design practice. Though the RANS model is able to capture the mean pressure distribution for both drag and lift, the fluctuating components are missing as before. For higher speeds S3 and S4 also, RANS model tends to predict the mean distribution as forecasted by LES. It can be seen that the building undergoes severe fluctuating loads due to the translating motion of the jet as shown in Figure 16 for speed S4.

Figure 17 shows the pressure data on individual points along the centerline surface of the building. Two extreme points are selected on the front and back of the cube. Also two points were chosen on the front and the middle of the building roof. It can be seen that LES replicates the experimental results accurately. This plot gives us a clear view as to how the C_P values change with the passage of the translating jet from one side of the building to the other side. It is also important to note the symmetry of the results for points at the same height on both the front and the back of the building. The distribution on the roof front is somewhat skewed, whereas that on the middle of the roof is very symmetric. The drag and lift coefficients are plotted in Figure 18 for all four speeds of jet translation for the dynamic

mesh case using LES. The drag coefficient C_D was observed to significantly increase as depicted in Figure 18a. The lift coefficient C_L does not show the same pattern with increasing translation speed, though close to equal magnitudes of positive and negative lifts are produced at different locations of the jet relative to the building. The maximum drag of the building is seen to occur at x/D value close to -1, i.e., before the jet passes the building. The results of RANS again show similar behavior as LES, but the distribution is much smoother. Figure 19 shows the effects of increased translating speed using realizable k-ε model. A lateral shift in both the drag and lift curves is noticed due to increase in translating speeds. This means that with increasing translation speeds, the building faces the peak loads at values of x/D greater than that for lower speeds. This situation is analyzed better by looking at the pressure and velocity contour plots in Figures 20 and 21, respectively. Due to viscous effects, for higher translating velocities, the flow near the ground is attached to the floor and cannot move as quickly as the top of the jet near the nozzle. Due to this the flow is bent away from the building model even when the jet is directly on top of the building. This causes the building to feel the effects later as the translation speed of the jet is increased.

The peak loads (C_P) experienced by each individual point on the building are shown in Figures 22 and 23. Figure 22 shows the comparison of LES and experimental data for both sliding and dynamic mesh. The numerical prediction mostly lies within the maxima and minima band determined experimentally. Figure 23 shows the variation in these peak point loads due to increased translation speeds of the jet obtained numerically. It can be seen that the front portion of the building faces increasing loads with increase in speed. This is due to the increase in the outflow velocities with increasing translating speed which was seen earlier. Also due to increased velocities at lower building heights as was seen previously, the

loads on the bottom frontal half is more. Also the negative loads on the roof points (lift) change rapidly with increases in jet translation speed compared to the positive loads. Note that X_B is distance along the centerline of the cubic building of side H_B starting from the bottom of the frontal face.

Table 2 shows the force coefficient values from both experimental and numerical simulations. It can be seen that the CFD (LES and reaz k-ε) cases (QS and S1), are smaller than the experimental cases. This might be attributed to the fact that the experimental values were calculated based on the centerline pressure data only.

The peak force coefficients on a cubic building oriented at zero degree angle with respect to the axis of translation of a microburst or a tornado are listed in Table 3 along with force coefficients that were calculated using the wind load provisions of ASCE 7-05 (2006). More details about the tornado simulation and load calculation can be found in the paper by Sarkar et al. (2006) and Sengupta et al (2007). The loads (F_D and F_L) were calculated using the maximum values of the coefficients in Table 3 for tornados of different intensities F1 to F5 using the mean-hourly equivalent wind speeds of the Fujita scale. For microburst load calculations, a downdraft mean-hourly equivalent wind speed of 140 mph (3-sec gust) was chosen that is comparable to the maximum horizontal wind speed of 150 mph measured at the Andrews Air-Force Base. It was observed that a microburst with wind speeds of 140 mph can generate loads equivalent to that of a tornado of F2 (160 mph, 3-sec gust) intensity on a cubic building. The drag force on a cubic building from a microburst corresponding to the wind speed mentioned earlier and the maximum values of peak drag coefficient in Table 3 was calculated to be 2.18 times greater than those of straight-line winds as stipulated by ASCE 7-05 (2006) with 40 m/s or 90 mph design wind speed (3-sec gust at 10 m height for

open terrain), while those from a tornado of F2 intensity was similarly calculated to be 2.07 times greater. This ASCE 7-05 design wind speed was chosen for comparison because tornadoes and microburst occur more frequently in non-hurricane zones and a region that is known as tornado alley. In this analysis, it is observed that although microburst produces lower uplift roof loads (Table 3 factor = 0.96) compared to a tornado (Table 3 factor = 1.46), it produces an additional downward force (Table 3 factor = -0.84) that is not considered in design (except buildings designed for snow loads). Thus, it can be argued that if buildings are designed to resist winds from an F2 tornado and adequate downward loads like snow loads these will be also able to withstand loads induced by a microburst of reasonably high intensity (140 mph winds).

5. Summary and Conclusion

The goal of the work presented here was to subject a cubic building model to simulated translating microburst to quantify the resulting aerodynamic loading on the building. Loads resulting from both static and moving impinging jets were studied. Based on the fact that LES produced superior results compared to RANS models in the case for static jet, it was used extensively for the moving jet simulations in this paper. The peak force coefficients for the microburst were determined for different translating speeds. Peak drag coefficient was observed to monotonically increase with higher microburst translation speed, whereas the peak lift coefficient remained the same for a range of speeds until a critical speed of S4 (2 m/s) was reached when positive (or upward force) peaks resulted along with higher negative peaks of lift force. Microburst can produce loads on buildings equivalent to that produced by an F2 tornado.

References

Alahyari, A., and Longmire, E.K. (1995) Dynamics of Experimentally Simulated Microbursts. AIAAJ. 33(11) 2128- 2136.

ASCE (2006) Minimum Design Loads for Buildings and Other Structures, ASCE Standard, SEI/ASCE 7-05. American Society of Civil Engineers.

Chattopadhyay, H. and Saha, S.K. (2003) Turbulent flow and heat transfer from a slot jet impinging on a moving plate. Int. J. Heat Fluid Flow. 24, 685-697.

Clark, J. and Filippone, A. (2007) Unsteady computational analysis of vehicle passing. J. Fluids Eng. 129, 3590-367.

Fluent. (2005) FLUENT *User's Guide.* Release 6.2. Fluent, Inc., Lebanon, New Hampshire.

Fujita, T.T. (1985) The Downburst: Microburst and Macroburst. University of Chicago Press.

Germano, M., Piomelli, U. Moin, P. and Cabot, W.H. (1991) A Dynamic Subgrid-Scale Eddy Viscosity Model. Physics of Fluids, 3, 1760-1765.

Letchford C.W. and Chay M.T. (2002) Pressure distributions on a cube in a simulated thunderstorm downburst. Part B: moving downburst observations. J. Wind Eng. Ind. Aerodyn. 90, 733-753.

Lilly, D.K. (1992) A Proposed Modification of the Germano Subgrid-Scale Closure Method. Physics of Fluids, 4, 633-635.

Lundgren, T.S., Yao, J. and N.N. Mansour, N.N. (1992) Microburst Modeling and Scaling. J. Fluid Mechanics. Vol. 239, pp. 461-488.

Orf, L.G. and Anderson, J.R. (1998) A numerical study of traveling microbursts. Monthly Weather Review. 127, 1244-1258.

Sarkar, P.P., Haan, F.L., Balaramudu, V. and Sengupta, A., (2006) Laboratory simulation of tornado and microburst to assess wind loads on buildings. Proc. ASCE Structures Congress, St. Louis, USA.

Sengupta. A., Haan, F.L., Sarkar. P.P. and Balaramudu, V. (2006) Transient loads on buildings in microburst and tornado winds. Proc. 4th Intl. Symp. on Computational Wind Engineering (CWE2006), Japan, July 16–19.

Sengupta. A. and Sarkar. P.P. (2007) Computational and experimental simulation of static and transient loads on buildings in microburst winds. Proc. 12th International Conference on Wind Engineering, Cairns, Australia, July 1-6.

Sengupta, A., Haan, F.L., Sarkar, P.P., and Balaramudu, V. (2007) Transient Loads on Buildings in Microburst and Tornado Winds. Submitted to Journal of Wind Engineering and Industrial Aerodynamics for review and publication.

Senter, J. and Solliec, C (2007) Flow field analysis of a turbulent slot air jet impinging on a moving surface. Int. J. Heat Fluid Flow, In press.

Ye, G. (2005) Using dynamic mesh models to simulate electrostatic spray-painting. High performance computing in science and engineering 05. eds. Nagel, W.E., Jager, W and Resch, M, 173-183.

Yao, J. and Lundgren, T.S. (1996) Experimental Investigation of Microbursts. Experiments in Fluids. 21, 17-25.

Table 1: Summary of mesh size, time step and velocity ratio used in numerical simulation

Mesh Size		Time Step [$= \frac{\Delta t * V_J}{D_J}$]		Velocity Ratio ($V_{TR} = V_T/V_J$)	
Name	# of cells*	Name	Step Size	Name	Ratio
M	1	T1	0.25	QS	0
M1	1.6	T2	0.10	S1	0.0225
M2	2	T3	0.05	S2	0.05
M3	2.8	T4	0.025	S3	0.1
	* in millions	T5	0.0125	S4	0.2
		T6	0.00625		

Table 2 Peak loads from Exp, LES and Realizable k-ε

Speed	Experiments		Simulation					
			LES				Realizable k-ε	
			Sliding Mesh		Dynamic Mesh			
	C_D	C_L	C_D	C_L	C_D	C_L	C_D	C_L
QS	1.7	-1.10	1.4*	-1.0*	1.4*	-1.0*	-	-
S1	1.7	-1.07	1.41	-1.01	1.42	-1.04	1.09	-1.0
S2	-	-	1.40	-1.03	1.48	-1.03		
S3	-	-	1.91	-1.06	1.90	-1.06	1.13	-1.0
S4	-	-	2.01	1.43/-1.08	2.71	1.24/-1.08	1.34	-1.08

* Values from static jet simulation only

Table 3 Cube with 0^0 orientation w.r.t. Tornado and Microburst Translation Axis

Type of Wind	**Type of Simulation**	**Translation Speed***	**Force Coefficients**		**Factor w.r.t. ASCE 7-05**
			C_D	C_L	
Tornado	EXP	QS	1.80	1.26	F2, 160 mph
		LS	**1.97**	**1.44**	1.46 Uplift
		HS	1.79	1.18	2.07 Drag
Microburst	EXP	QS	1.70	-1.10	140 mph
		S1	1.70	-1.07	
	CFD	QS	1.40	-1.00	0.96 Uplift
		S1	1.40	-1.04	- 0.84 Down
		S2	1.50	-1.03	2.18 Drag
		S3	1.90	-1.06	
		S4	**2.70**	**+1.24/ -1.08**	
ASCE 7-05	STANDARD		1.02	1.08	90 mph

*QS: Quasi-steady, LS: Low Speed, HS: High Speed

The wind speeds are 3-sec gusts and the force coefficients that were used for calculating the factors in the last column are highlighted in bold font.

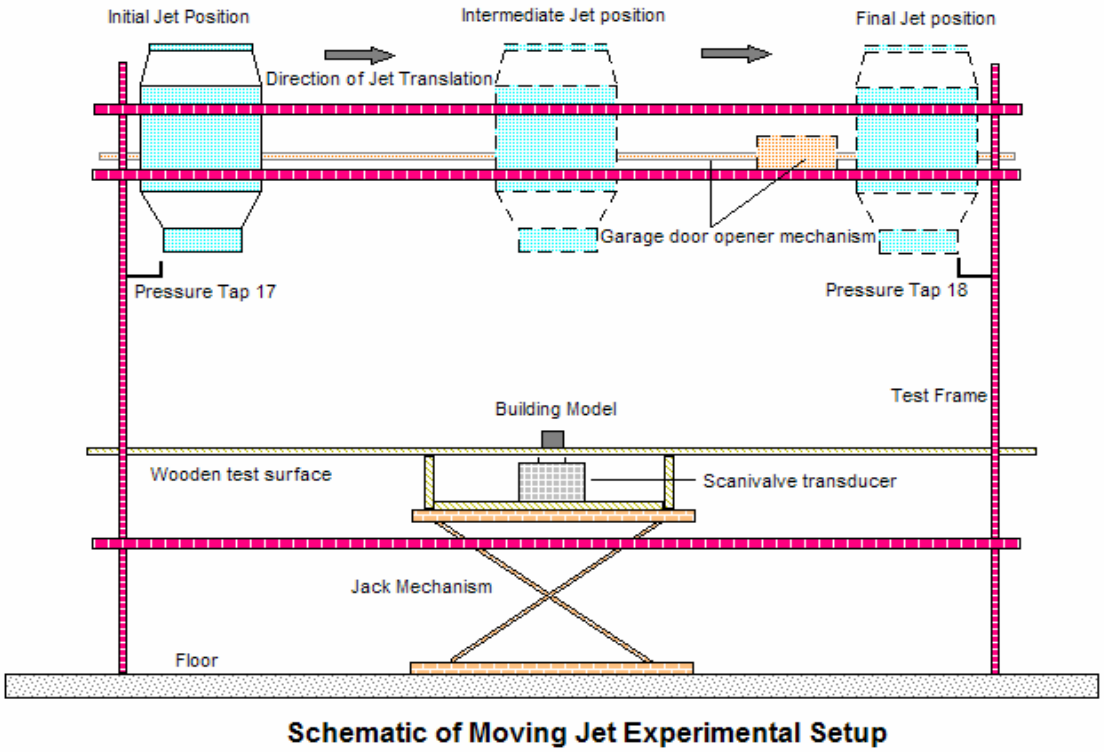

Figure 1: Sketch of Experimental Setup

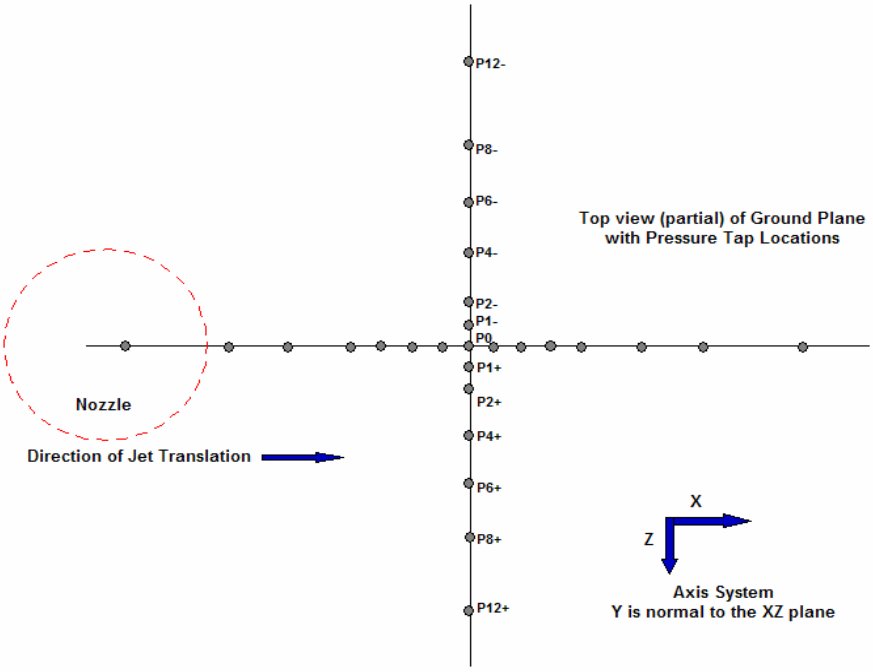

(a)

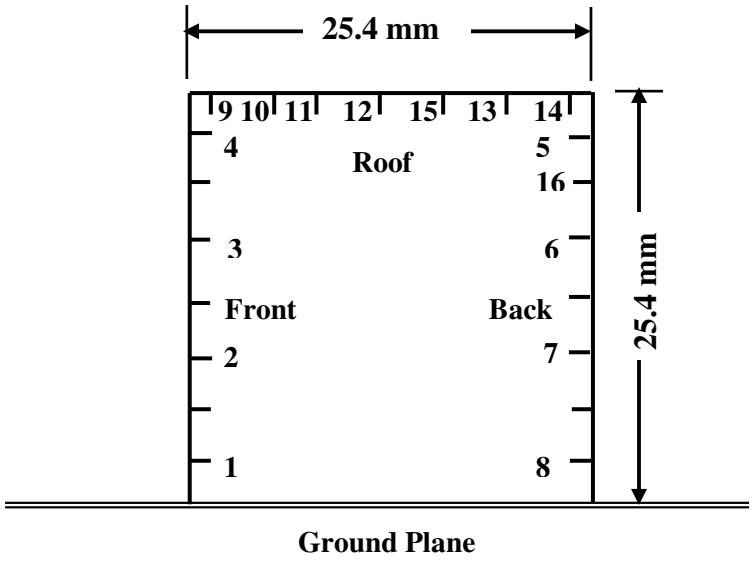

(b)

Figure 2: (a) Ground surface pressure tap location schematic
(b) Building model with pressure tap location and number of building model with pressure tap location and numbers

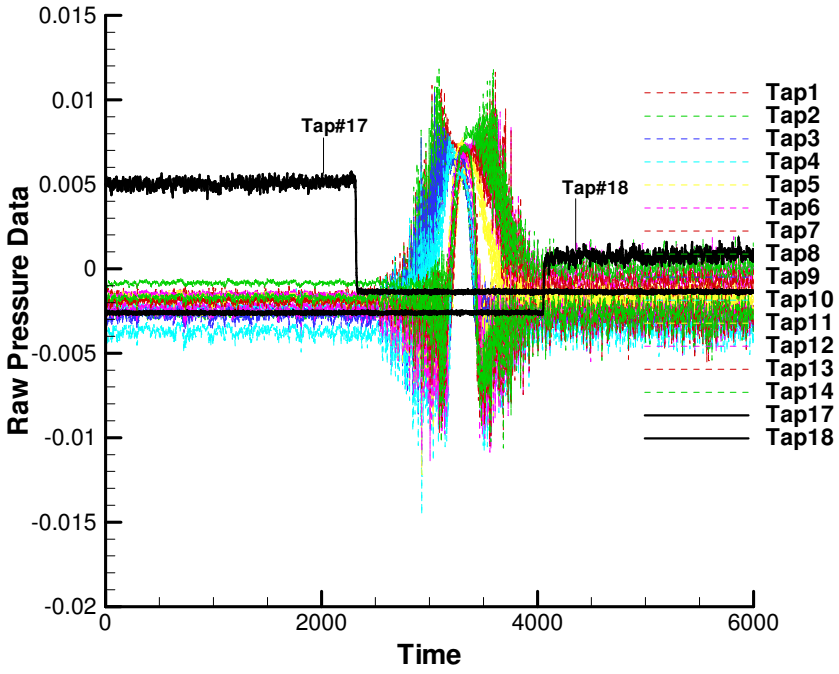

Figure 3: Raw pressure data showing effectiveness of starting and stopping time

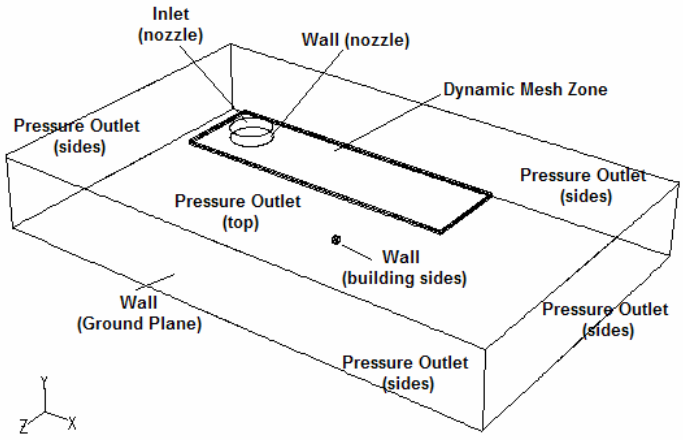

(a)

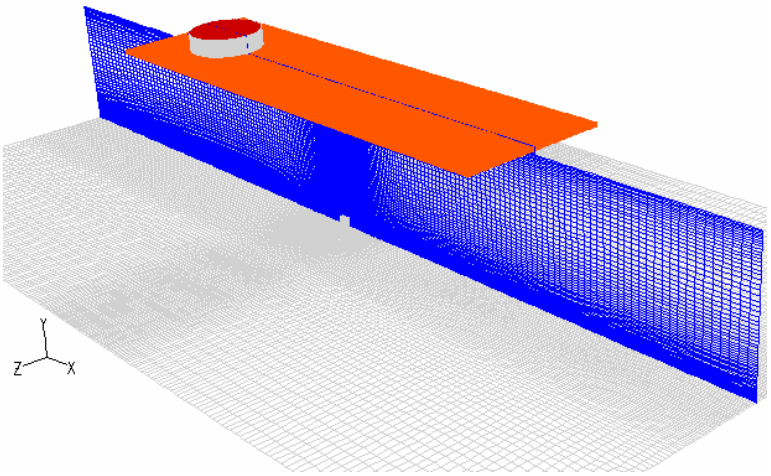

(b)

Figure 4: Numerical boundary and Mesh
(a) Numerical boundaries (b) Grid for Dynamic Mesh

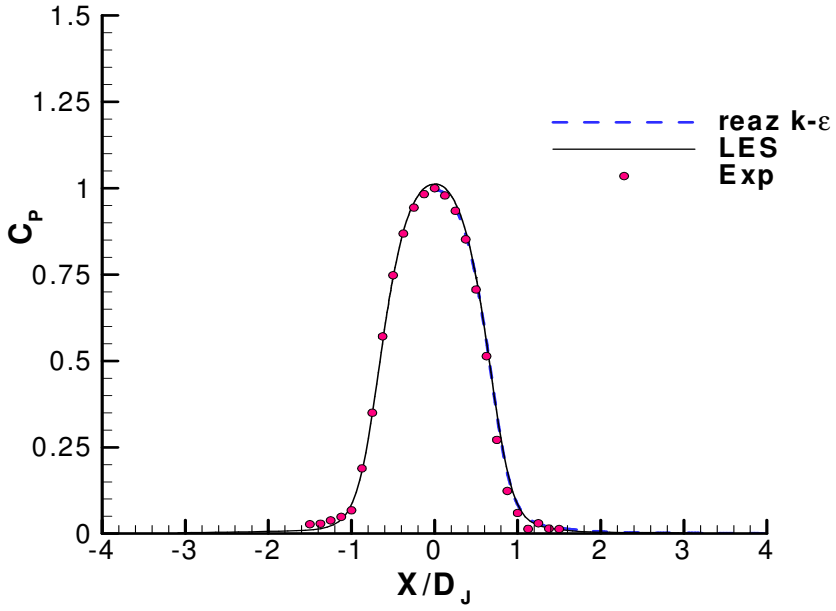

(a)

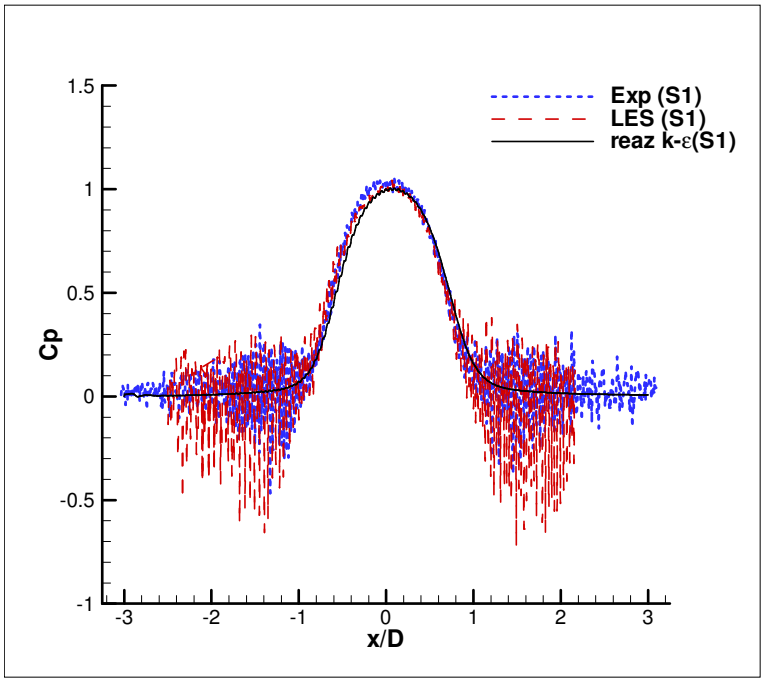

(b)

Figure 5: (a) Ground Pressure for Static Jet
(b) Moving Jet Ground Pressure Comparison (LES, reaz k-ε & Exp)

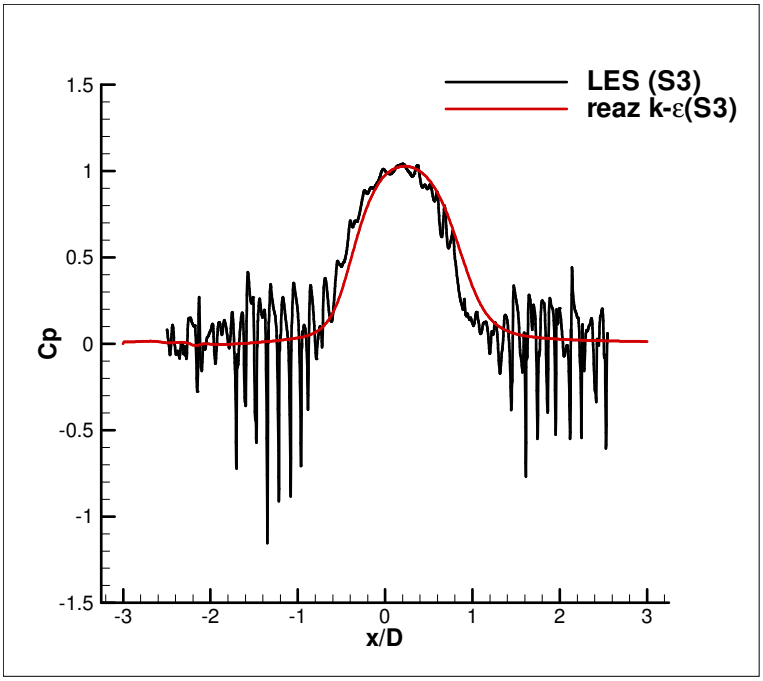

(a)

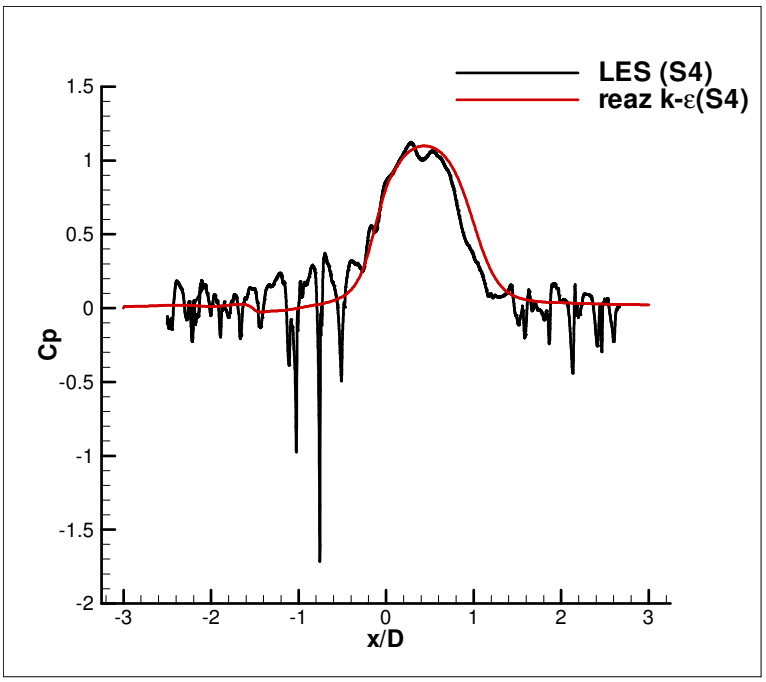

(b)

Figure 6: (a) Ground pressure at P0 for S3 (LES & reaz k-ε)
(b) Ground pressure at P0 for S4 (LES & reaz k-ε)

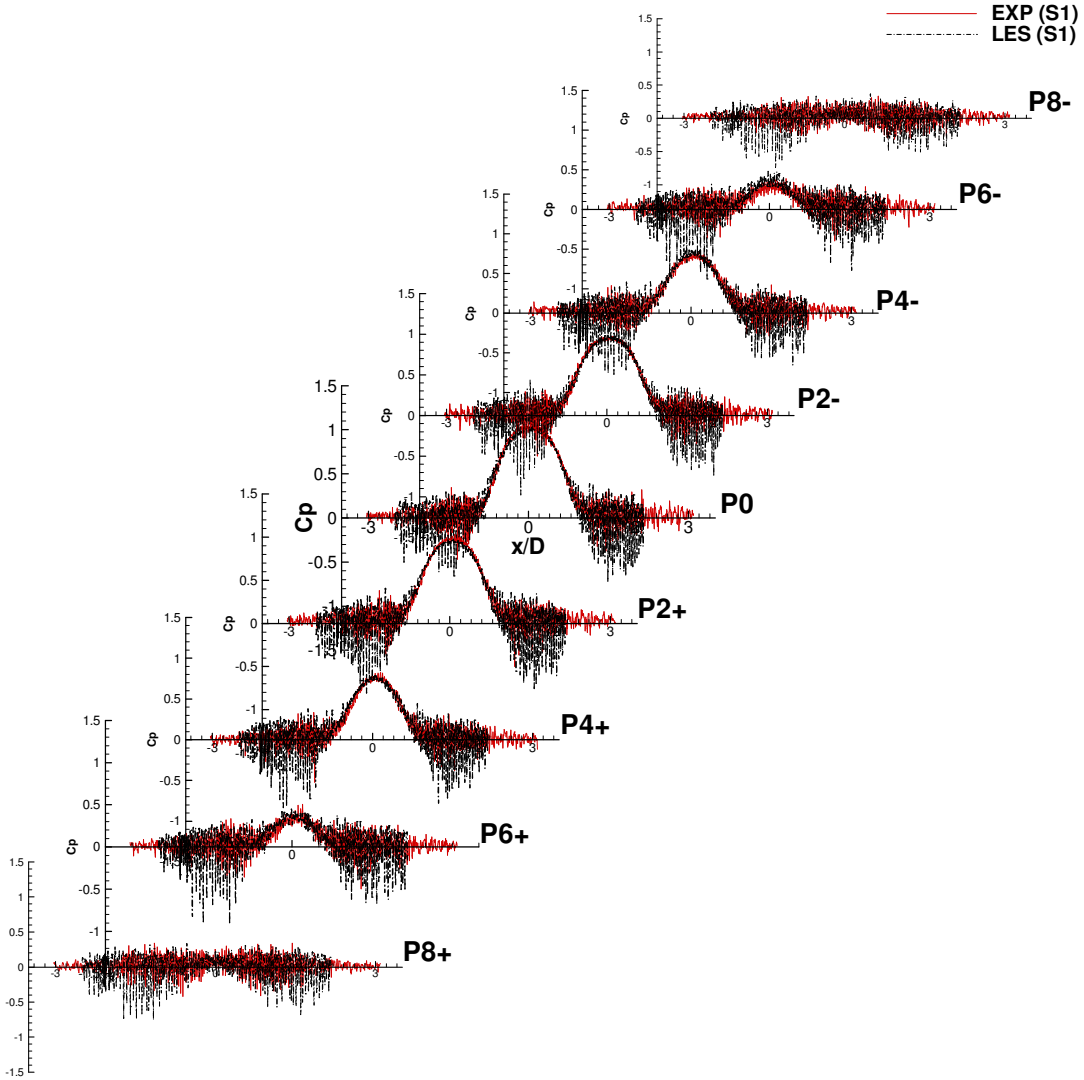

Figure 7: Ground Pressure Comparison along X = 0 line (Points P8- to P8+)
[LES & Exp at S1]

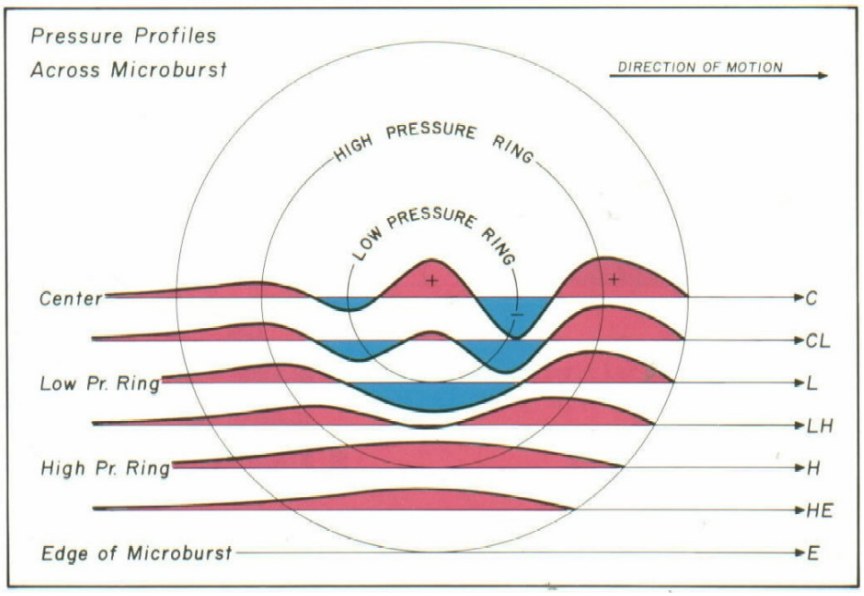

(b)

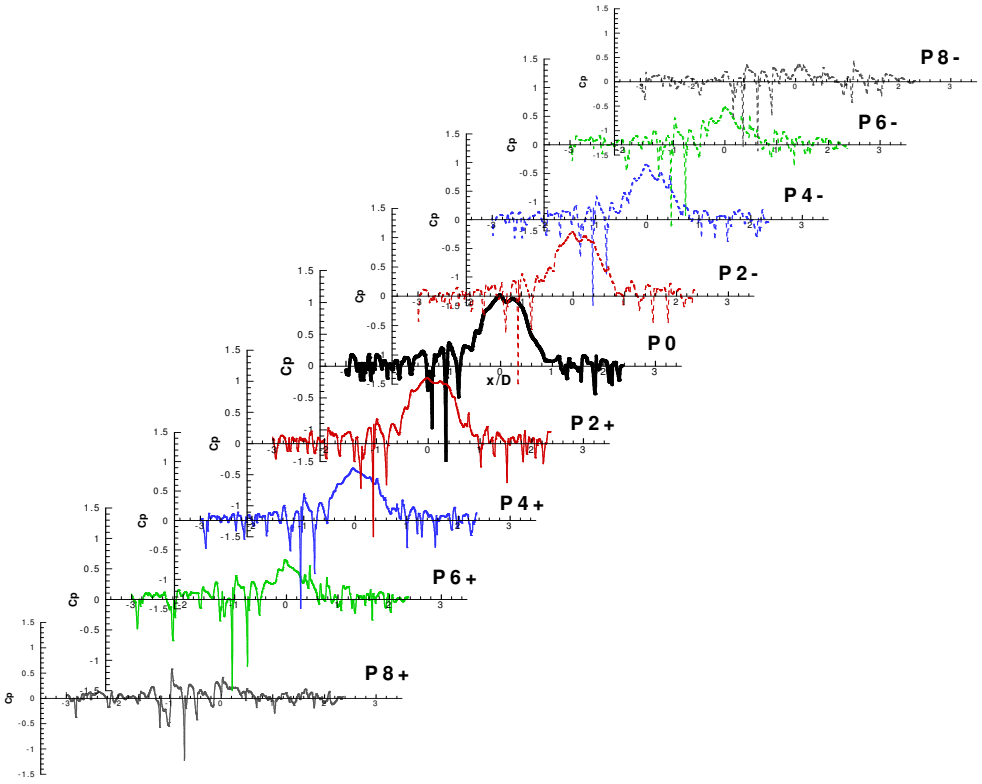

(c)

Figure 8: (a) Ground pressure distribution due to translating microburst hypothesized by Fujita (1985) (b) Ground Pressure LES at speed S4

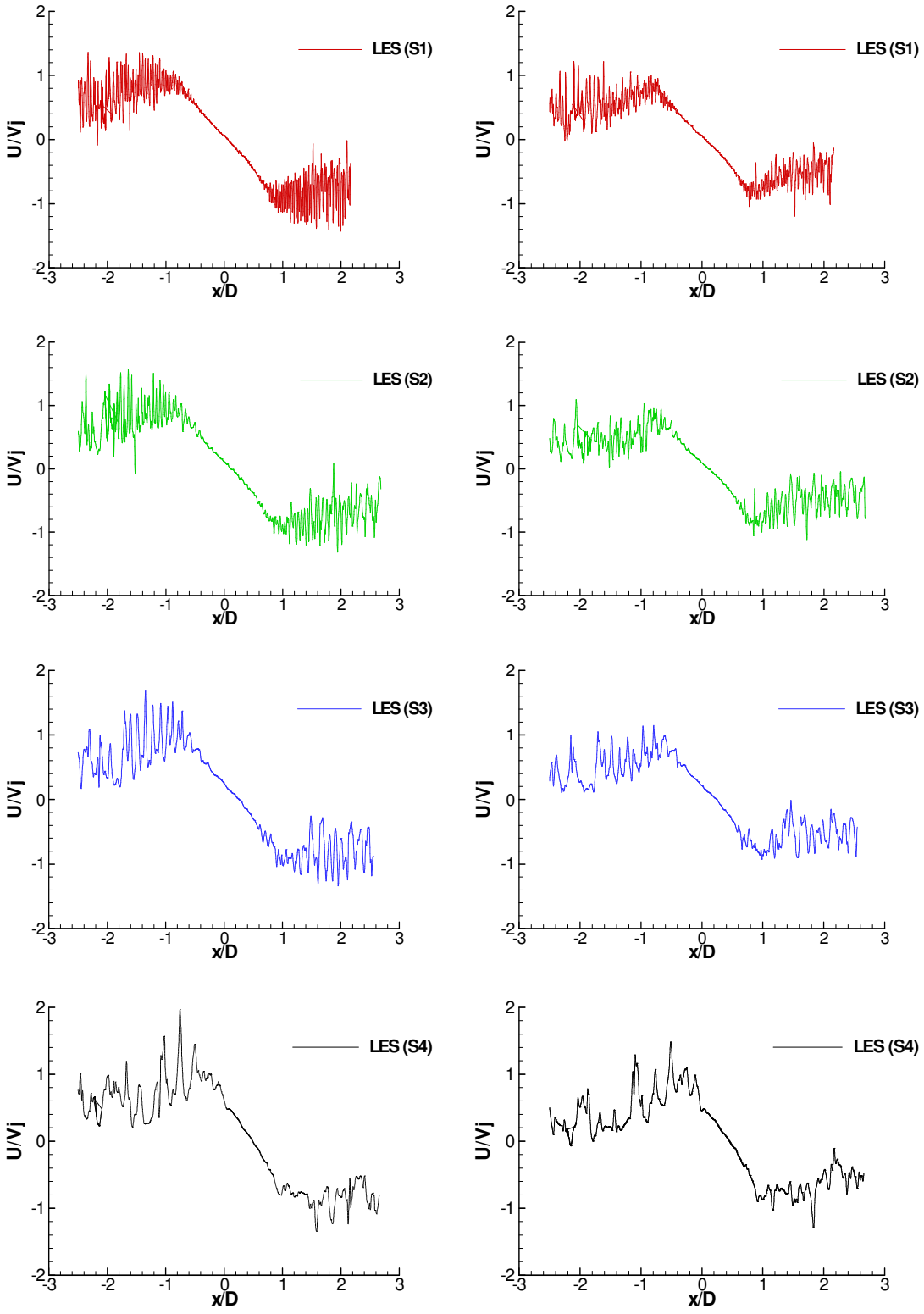

(a) (b)

Figure 9: Ground Velocity at Different Jet Translation Speeds (a) At $0.5H_B$ (b) At H_B

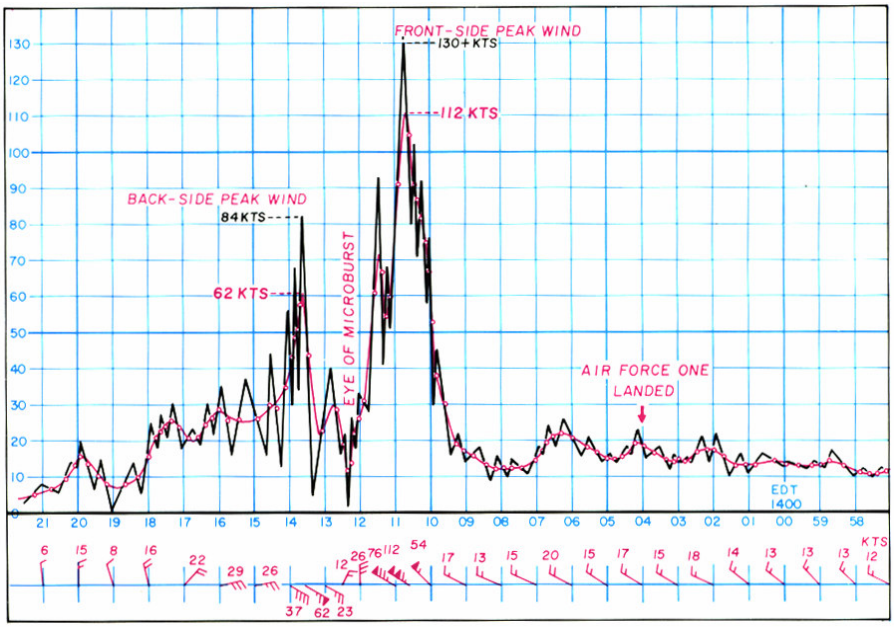

(a)

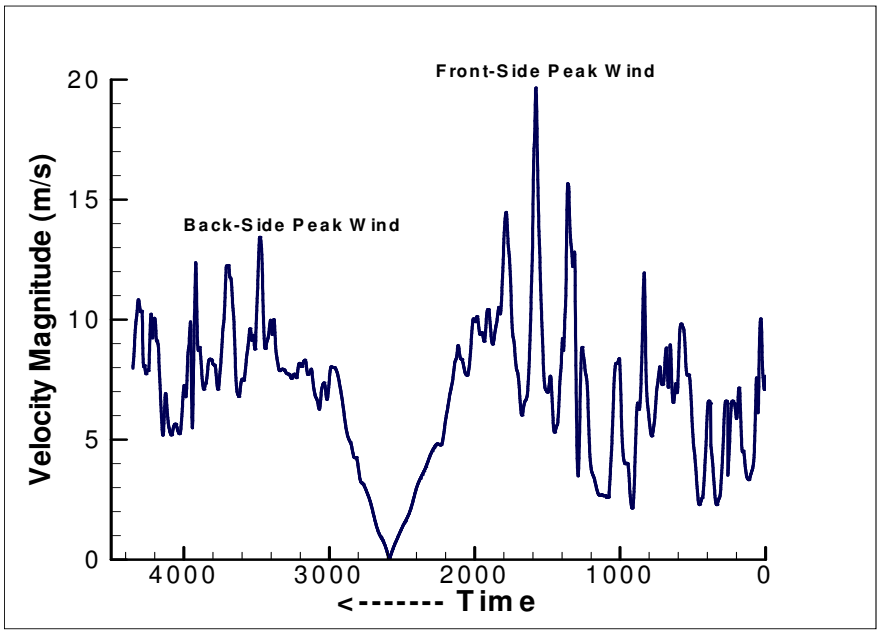

(b)

Figure 10: Comparison of Field (AFB) and numerical (LES) wind speeds due to a traveling microburst
(a) At Andrews Air-Force Base (AFB) (b) LES (S4)

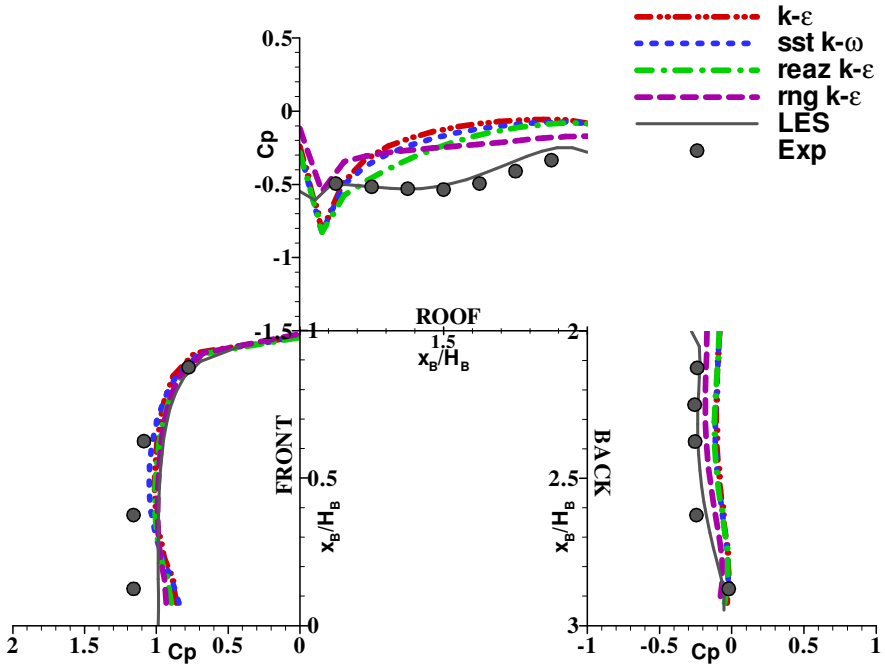

(a)

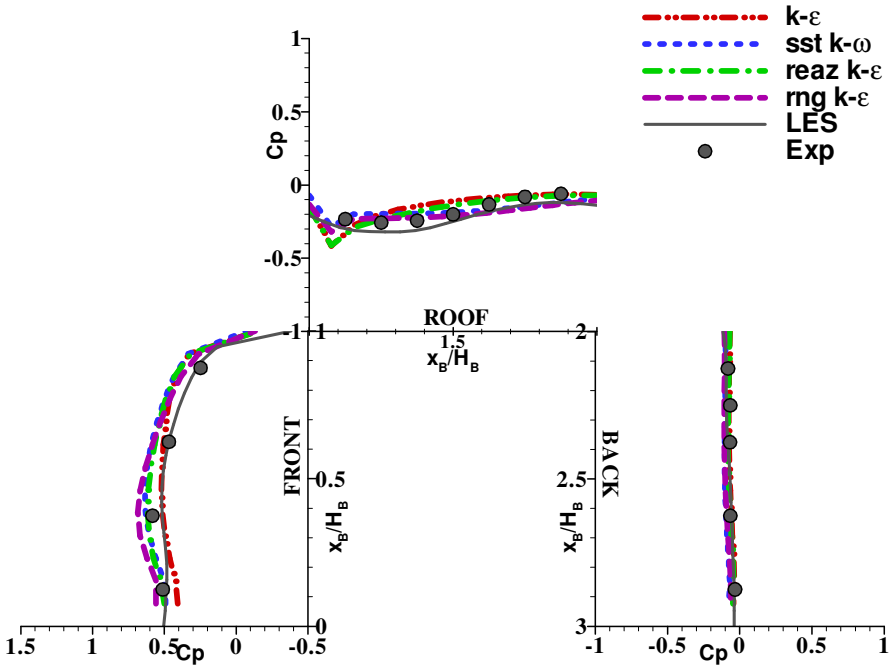

(b)

Figure 11: Plots of Static building with all turbulence models
(a) Building at 1D (b) Building at 2D

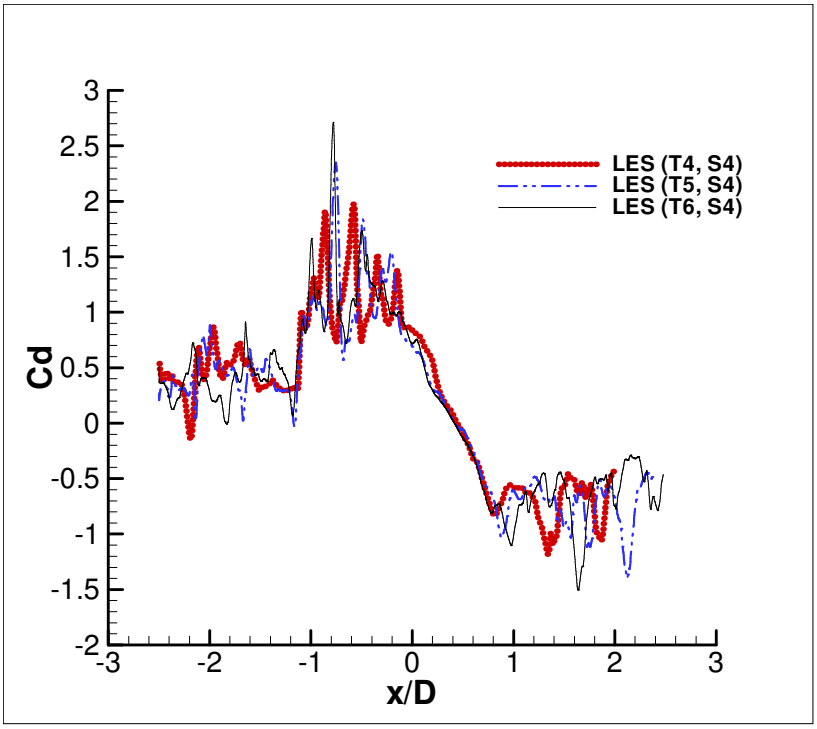

(a)

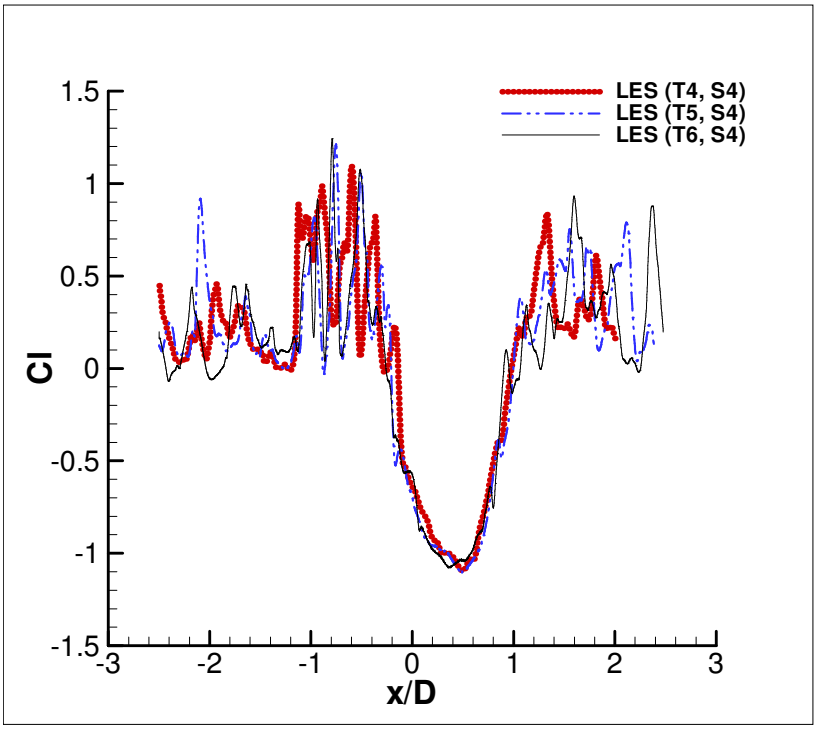

(b)

Figure 12: Comparison of Time Step (LES, Dynamic Mesh, M2, S4) (a) Drag (b) Lift

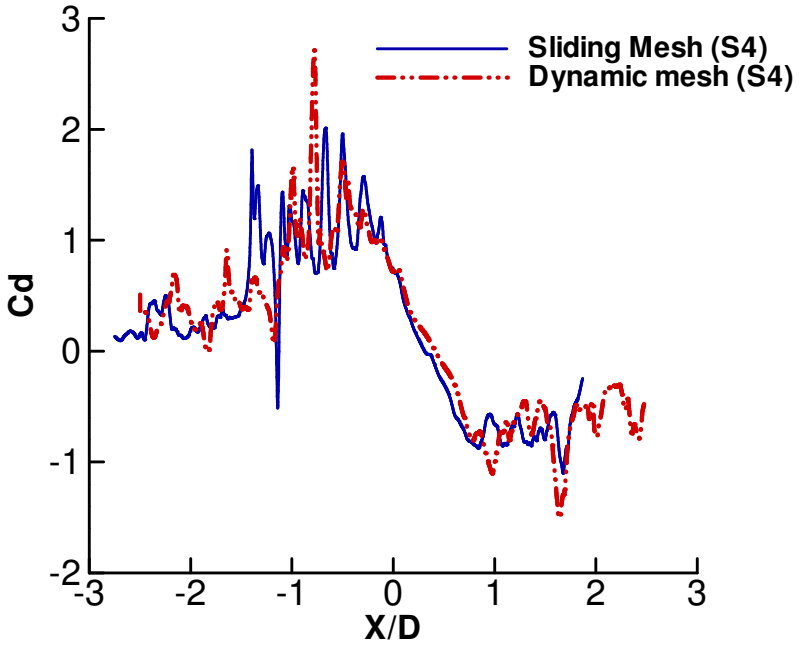

(a)

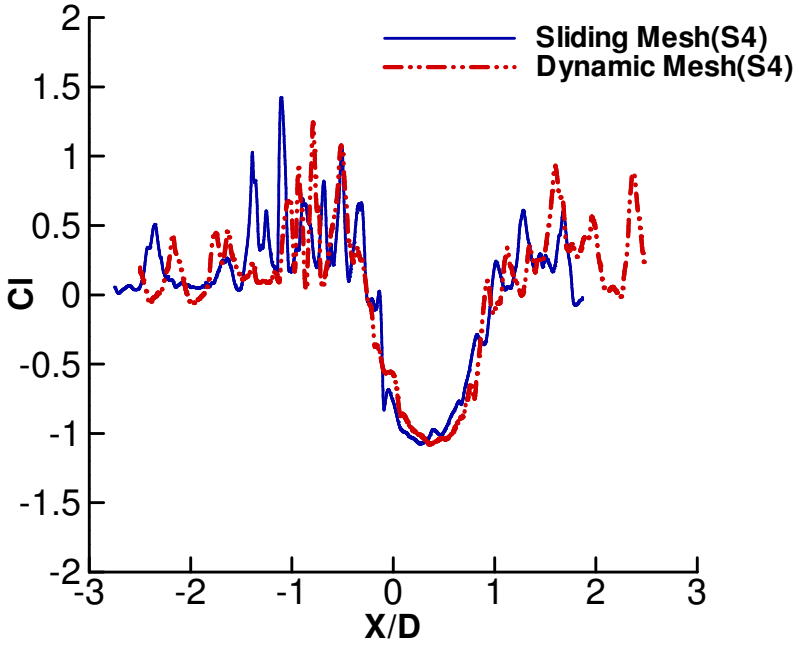

(b)

Figure 13: Comparison of Drag and Lift for Dynamic Mesh & Sliding Mesh (LES, M2)
(a) Drag (b) Lift

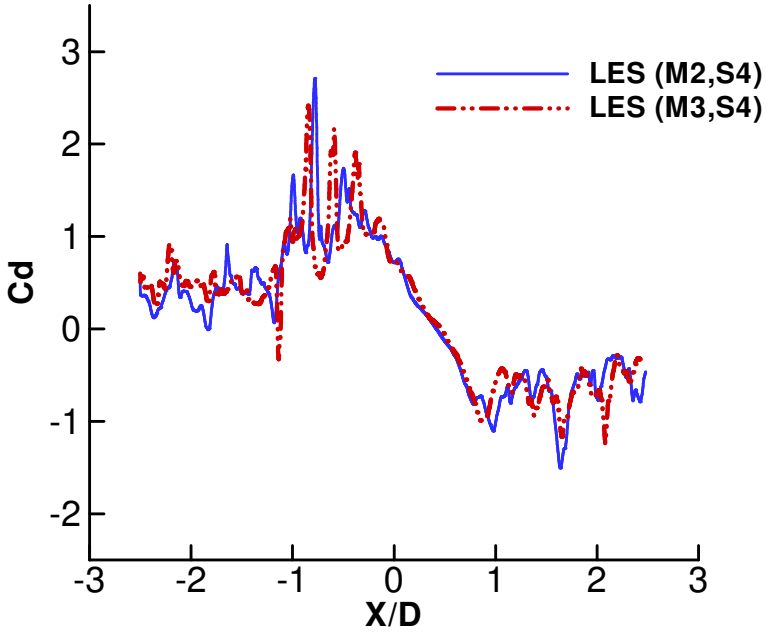

(a)

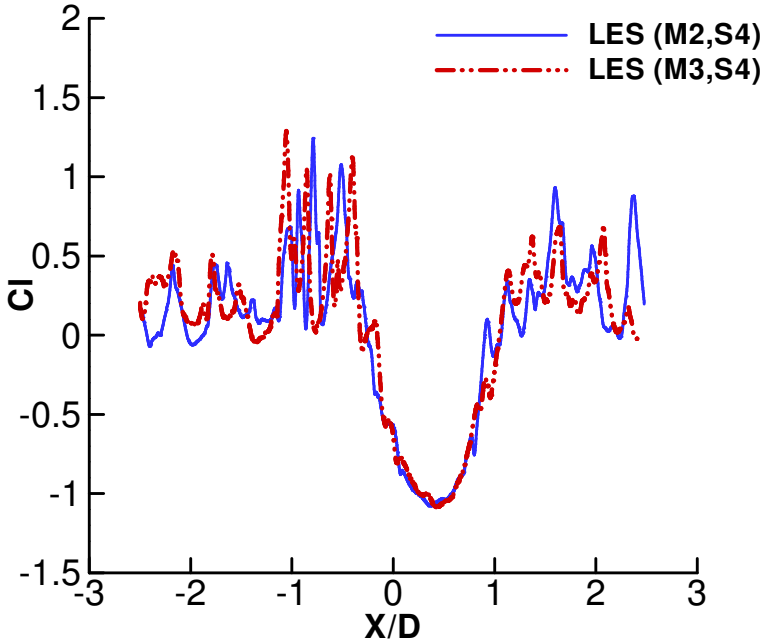

(b)

Figure 14: Comparison of Grid Size (LES, Dynamic Mesh, S4)
(a) Drag (b) Lift

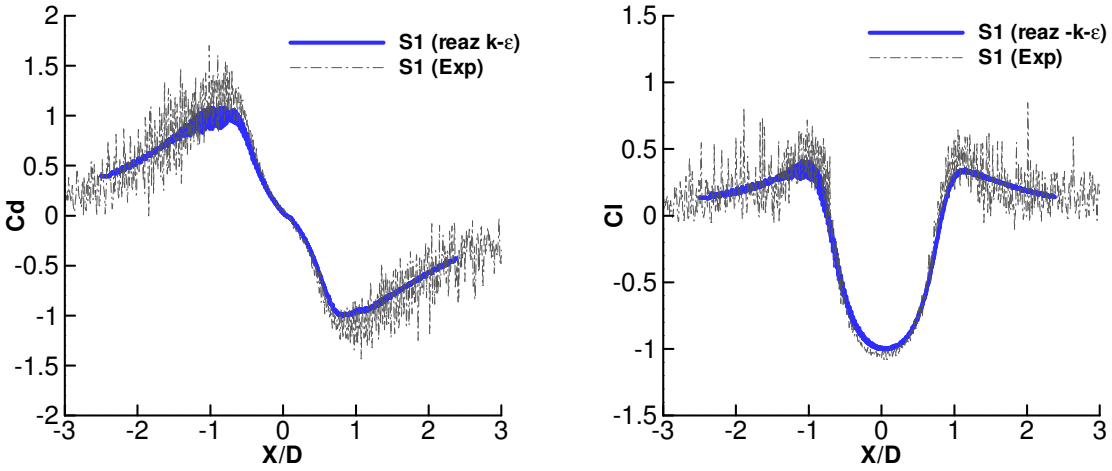

(a)

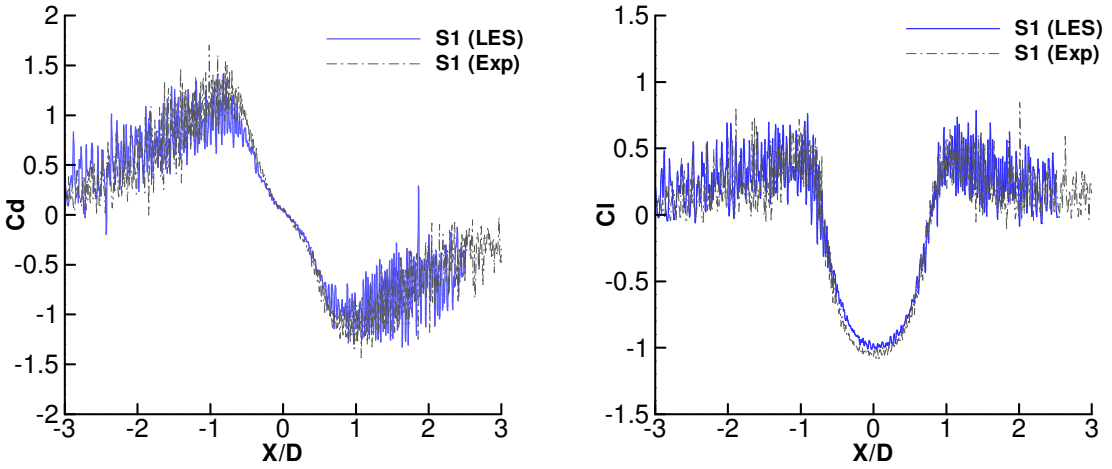

(b)

Figure 15: Comparison of Drag and Lift (Numerical and Experiments at S1)
(a) reaz k-ε (b) LES

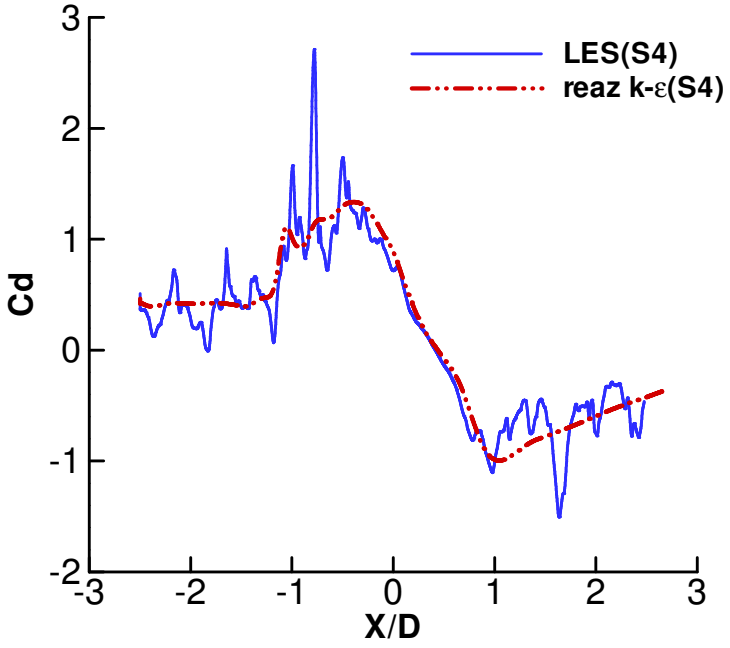

(a)

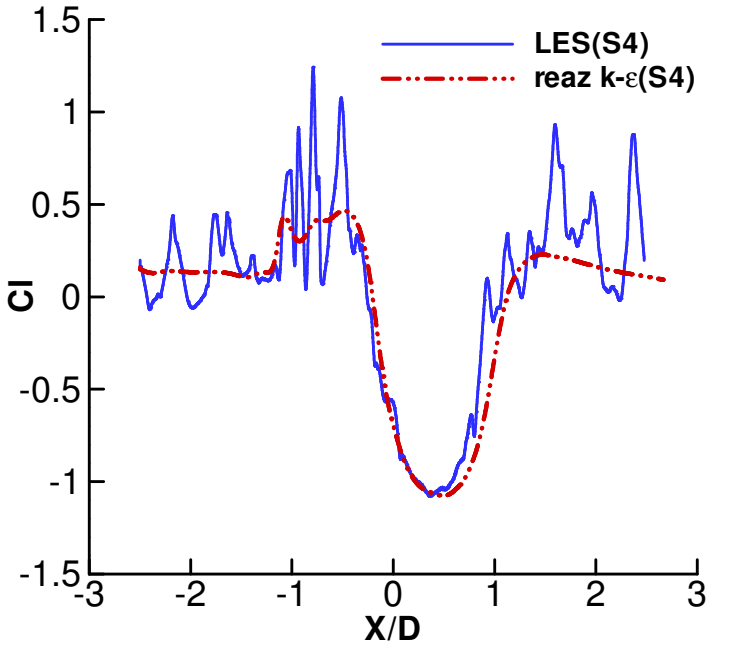

(b)

Figure 16: Comparison of Drag and Lift (LES and reaz k-ε) (a) Drag at S4 (b) Lift at S4

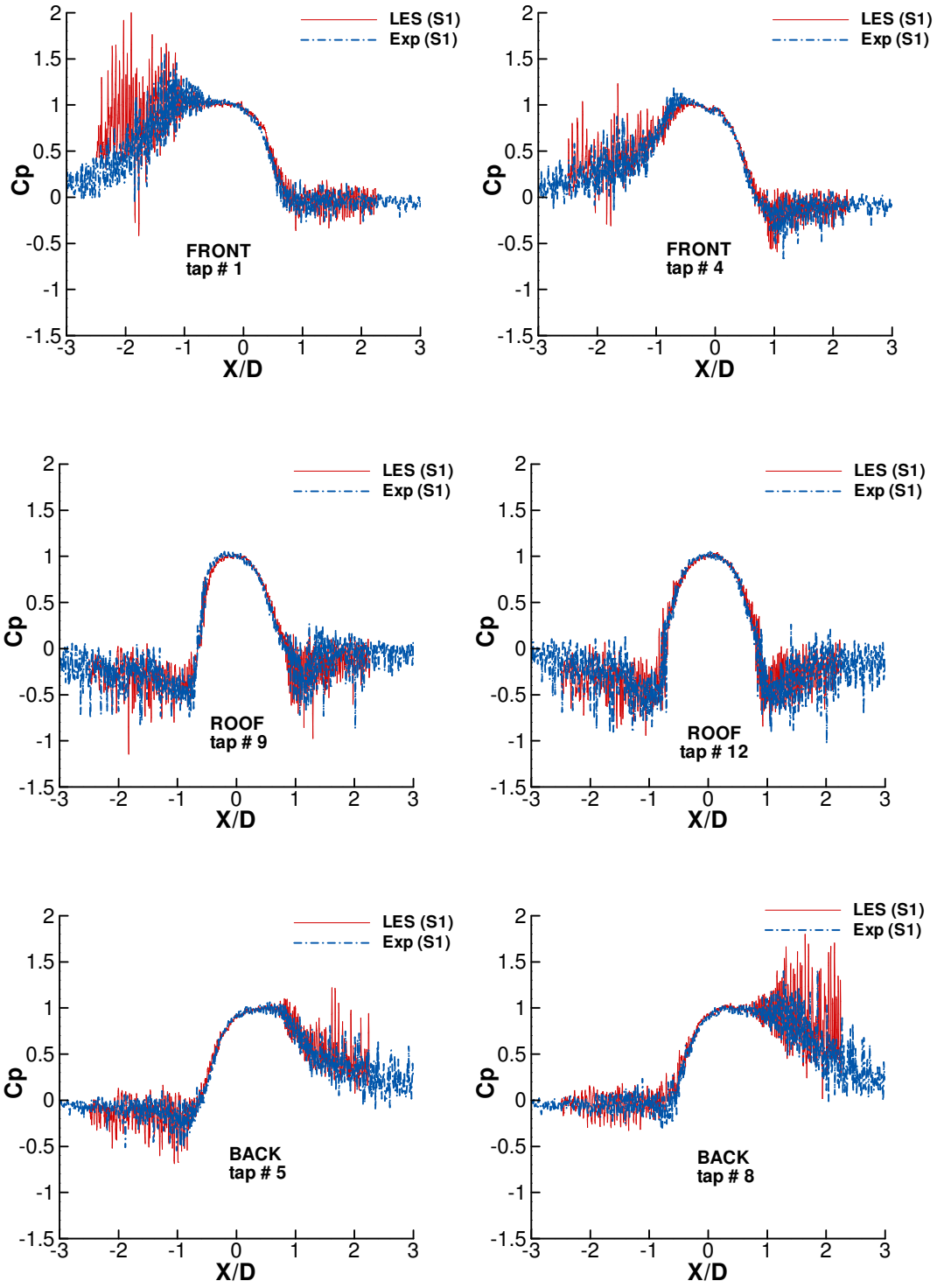

Figure 17: Comparison of point pressure on bldg (LES + Exp)

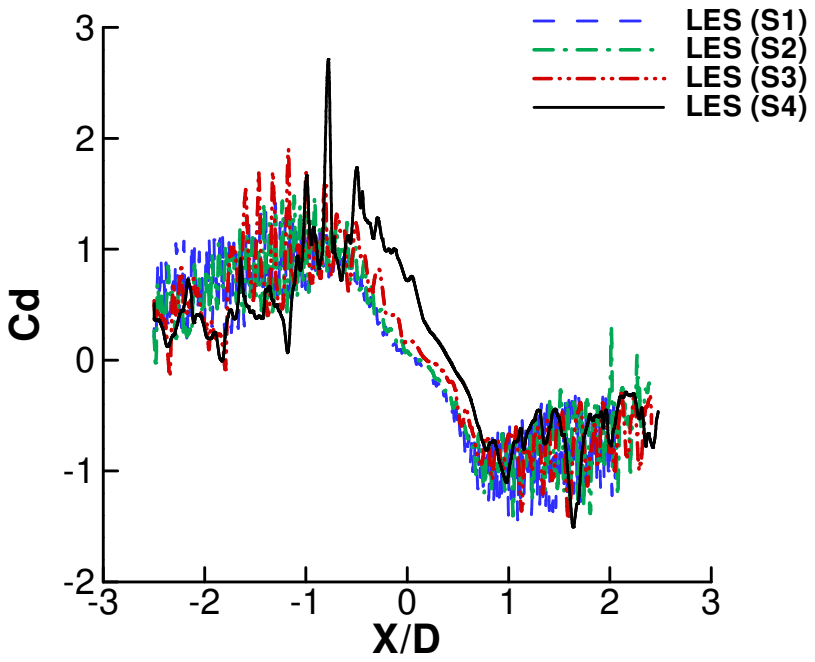

(a)

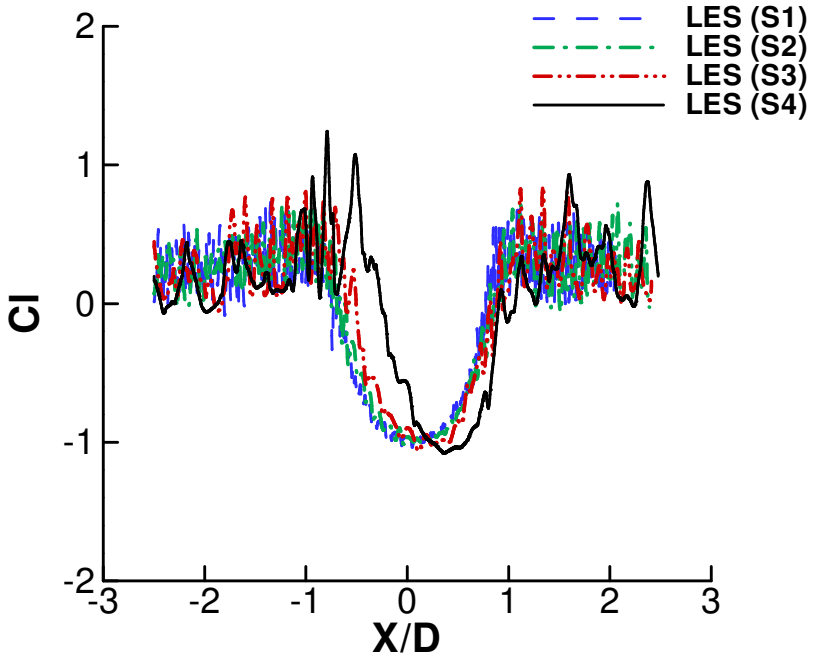

(b)

Figure 18: Comparison of Drag and Lift on bldg (LES all speeds – Dynamic Mesh, M2)
(a) Drag (b) Lift

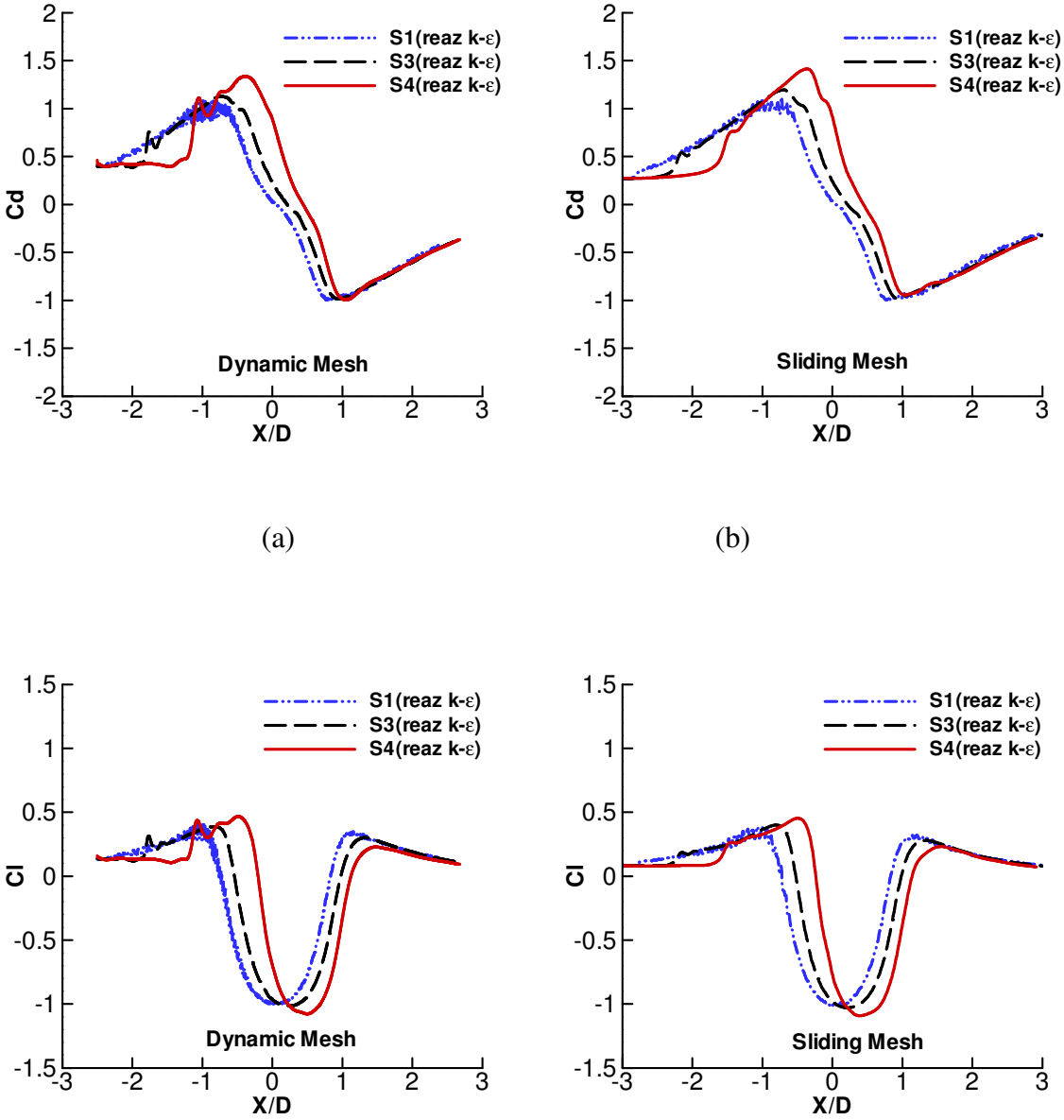

Figure 19: Comparison of Drag and Lift for Dynamic Mesh + Sliding Mesh (reaz k-ε)
(a) Drag - Dynamic Mesh (b) Drag – Sliding Mesh
(c) Lift - Dynamic Mesh (d) Lift – Sliding Mesh

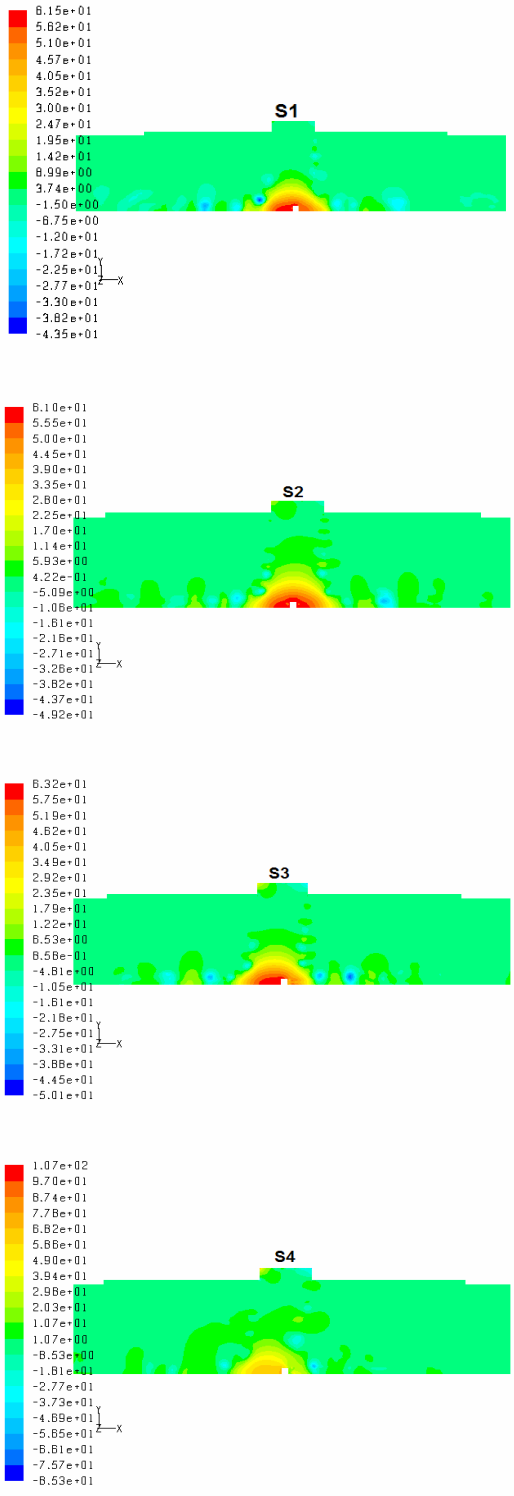

Figure 20: Contour Plots of Pressure (LES, All Speeds)

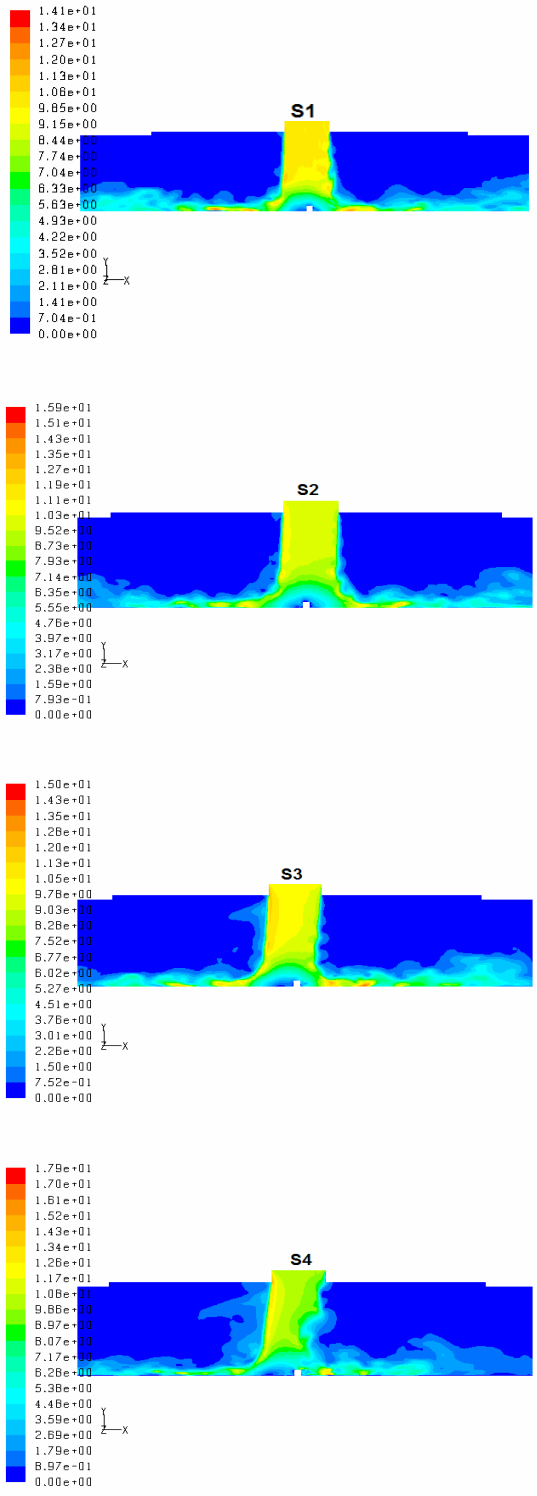

Figure 21: Contour Plots of Velocity (LES, All Speeds)

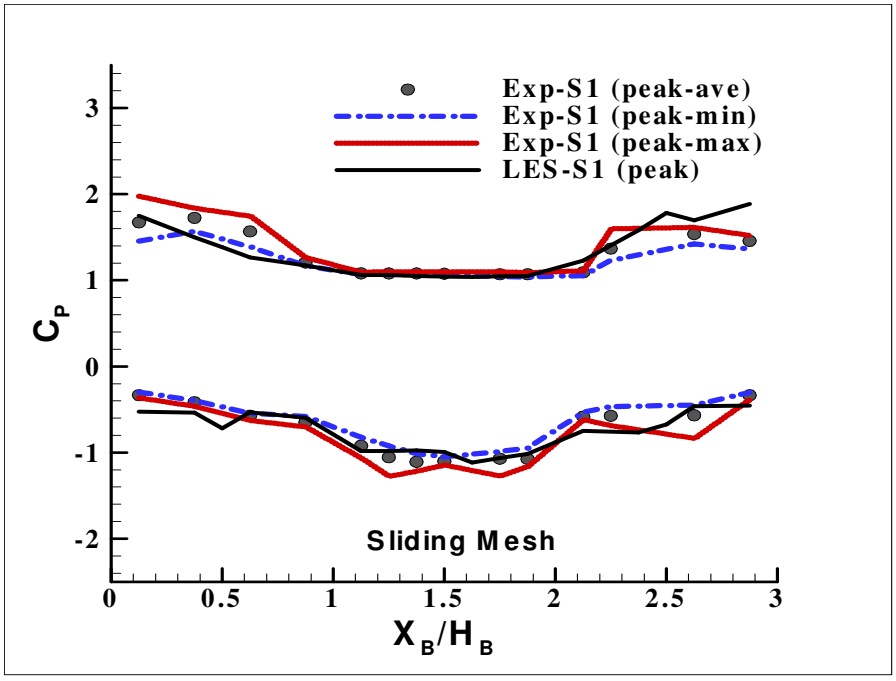

(a)

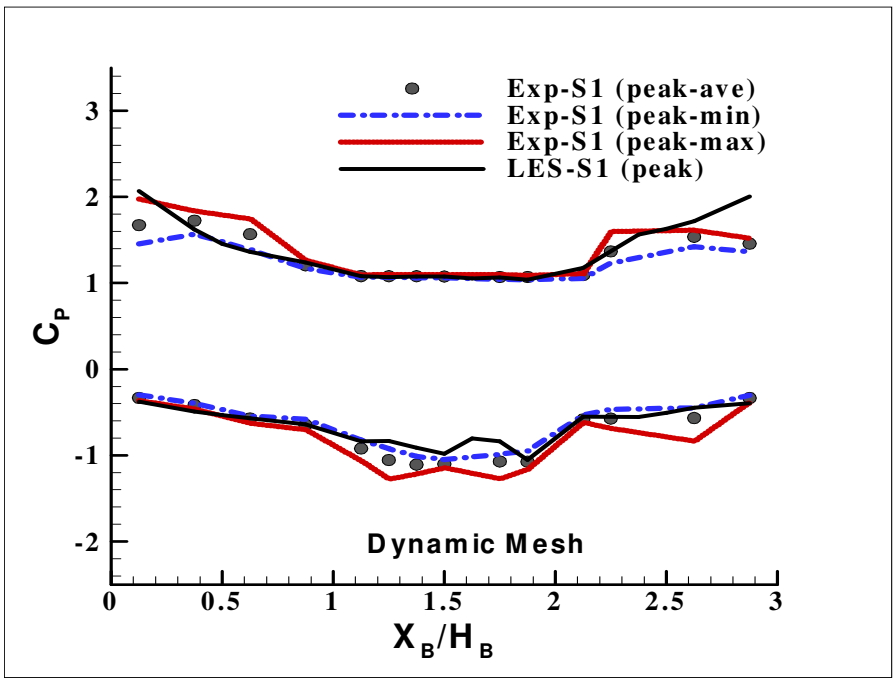

(b)

Figure 22: Comparison of Peak Loads (LES with Exp)
(a) Sliding Mesh (b) Dynamic Mesh

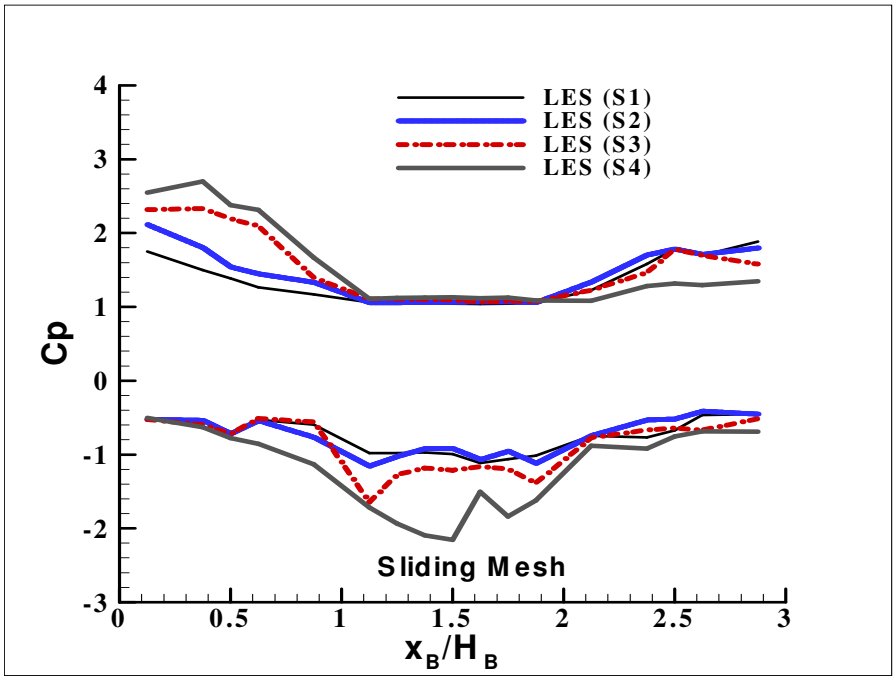

(a)

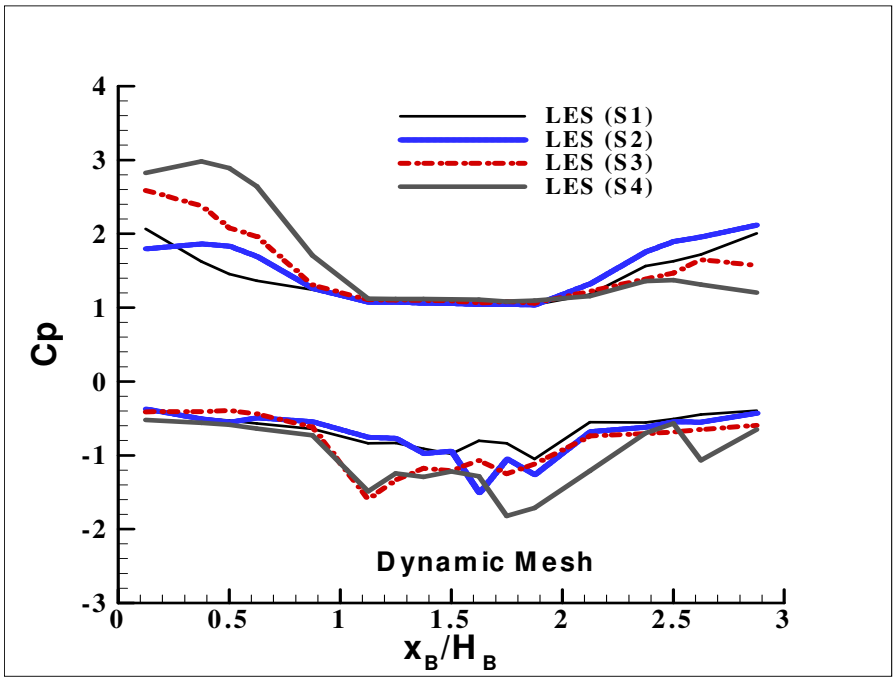

(b)

Figure 23: Comparison of Peak Loads (LES at different speeds, S1-S4)
(a) Sliding Mesh (b) Dynamic Mesh

CHAPTER 5

SUMMARY, CONCLUSIONS AND RECOMMENDATIONS

5.1 Summary and conclusions of current work

The current research reports results from both experimental and numerical analysis of microburst type wind profiles and its effects on cube-shaped buildings. This research is the first 3D numerical work in the field of microburst-generated wind loads and its effects on buildings. Microburst is a rare phenomenon that occurs during thunderstorms. Wind-induced damage to properties from thunderstorms, most likely during a microburst when extreme winds are generated, averages $1.4 billion per year in the US, and hence it is important to understand the wind effects of a microburst on buildings and other commonly occurring structures. Both a static as well as a moving microburst was simulated in the Wind Simulation and Testing (WiST) Laboratory at Iowa State University (ISU) using a round impinging jet. The major accomplishments of this research work are summarized below.

- Designed and constructed a microburst simulator capable of generating a static and translating microburst using an impinging jet. The requirements of portability, storage and low cost dictated its final design. This small-scaled microburst simulator was built to conduct preliminary research that eventually helped in the design of the much larger microburst simulator (scaled up by 9:1) as part of the ISU Tornado/Microburst Simulator (Haan et al., 2007) located in the WiST Lab.

A garage door opener was used to move the jet nozzle horizontally resulting in a uniform jet translation velocity. In the absence of a triggering mechanism to record the motion of the jet, a new method of stamping the starting and stopping time of the translating jet was devised using two pressure ports.

- Studied the effects of an impinging jet and proposed three new equations for boundary layer growth due to the impinging jet and subsequent wall jet formation. The experimental data used for the equations used hotwire, pressure rake and PIV data, as such reducing the bias of these equations towards a particular experimental technique.
- Compared the experimental data above with numerical results from 2D RANS and 3D LES simulations and validated the fact that the maximum velocity in the wall jet occurred in the regions of $0.75 \leq x/D_J \leq 1.25$.
- The loads on two cube-shaped prisms representing buildings with different dimensions were determined experimentally for different locations of these bluff bodies from the center of the static impinging jet. The above experiments were repeated for three different jet impingement heights as well as two different jet exit velocities. It was determined that jet height H2 produced the highest loads on the building at most locations. It was also found that the bigger building (B2) experienced more loads (as normalized by area) compared to the smaller building (B1).
- Conducted an extensive numerical validation of the above experiments using RANS and LES. The numerical simulations were performed for jet height H2 and building B2 based on the findings reported previously. Both the mean and peak

loads for the static jet case from the numerical simulations were determined and it was found that LES produced the best results in comparison with the experimental data.

- It was found that the load distribution on the cubed-shaped buildings tested under microburst type of wind flow is completely different from what they would experience in a normal boundary-layer type of flow. The distribution of roof pressure varies the most, depending on the location of the cube from the center of the jet. Major variation in overall load distribution occurs within the zone $0.0 \leq x/D_J \leq 1.25$. For $x/D_J \geq 1.25$, the overall load distribution begins to resemble that of boundary-layer type of flow.
- It was found that the buildings experienced severe downward force on the roof, which never occurs in a boundary-layer type of flow, and therefore not accounted for in building design codes.
- Used Particle Image Velocimetry (PIV) to study and visualize the flow field around the cube-shaped bodies at various distances from the center of the impinging jet and compared the results with that obtained numerically as discussed above.
- Conducted experiments on the effects of transient loading on the bluff bodies due to the linear translation of the jet at jet translation to jet exit velocity ratio (V_{TR}) of 0.0225. Found the peak loads on the body due to the moving jet and compared them with the static case.
- Used both a sliding as well as dynamic mesh to replicate the moving jet effects ($V_{TR} = 0.0225$) numerically. Major emphasis was placed on LES, though RANS

models were used in a few cases. Used LES to simulate higher jet translation speeds corresponding to the ratio (V_{TR}) of jet translation speed to jet exit speed of 0.05, 0.1 and 0.2, which could not be achieved in the laboratory due to physical limitations of the experimental equipment used.

- It was found from the above study that peak load on the cube-shaped bluff bodies, specially drag, increases significantly with increase in jet translation velocities. The study also emphasized the applicability of LES to model the fluctuating wind loads on the building models due to both static and moving jets. It could be seen that even with limited computer resources and a modest mesh size, LES was able to capture the flow physics and replicate the experimental results with greater accuracy compared to other turbulence models.
- Microburst can produce loads on buildings equivalent to that generated by an F2 tornado.

5.2 Recommendations for future research

Based on the research accomplishments as described above, the following recommendations are suggested.

- Study wind effects on buildings and other structures of different sizes and shapes using the larger microburst simulator that was mentioned earlier. This will give better scaling effects and an extensive database of loads.
- Simulate higher jet translation to jet exit velocity ratios ($V_{TR} > 0.0225$), which could not be achieved experimentally in the current research. This would help to validate the LES results that were presented in this dissertation.

- Formulate methods to improve the jet exit conditions that would create a more realistic rolling vortex near the ground. Try to add effects of temperature and humidity in both numerical and physical simulation models to mimic nature more realistically.
- Use high speed PIV to capture the evolution of the rolling vortex created due the jet impingement and also study the distribution of the velocity field (both on the ground and around the building model) due to the translating impinging jet. The results can be compared with the current LES data.
- Use LES with more accurate 3D inlet velocity profile as input (from PIV data), larger lateral boundaries and bigger mesh size (5-10 million cells) to see if better results are achieved in terms of the rms values of pressure and velocity.